

Quantification and comparison of the neuroarchitecture of deep cerebellar nuclei in the rat and macaque

Dissertation

zur Erlangung des Grades eines Doktors der Naturwissenschaften

der Mathematisch-Naturwissenschaftlichen Fakultät

und

der Medizinischen Fakultät

der Eberhard-Karls-Universität Tübingen

vorgelegt

von

Haian Mao

(毛海岸)

aus Loudi, China

Mai - 2019

Tag der mündlichen Prüfung: 26.11.2019

Dekan der Math.-Nat. Fakultät: Prof. Dr. W. Rosenstiel

Dekan der Medizinischen Fakultät: Prof. Dr. I. B. Autenrieth

1. Berichterstatter: Prof. Dr. Fahad Sultan

2. Berichterstatter: Prof. Dr. Stefan Liebau

Prüfungskommission:

Prof. Dr. Fahad Sultan

Dr. Marc Himmelbach

Prof. Dr. Hans-Peter Thier

Prof. Dr. Almut Schüz

Erklärung / Declaration:

Ich erkläre, dass ich die zur Promotion eingereichte Arbeit mit dem Titel:

“Quantification and comparison of the neuroarchitecture of deep cerebellar nuclei in the rat and macaque”

selbständig verfasst, nur die angegebenen Quellen und Hilfsmittel benutzt und wörtlich oder inhaltlich übernommene Stellen als solche gekennzeichnet habe. Ich versichere an Eides statt, dass diese Angaben wahr sind und dass ich nichts verschwiegen habe. Mir ist bekannt, dass die falsche Abgabe einer Versicherung an Eides statt mit Freiheitsstrafe bis zu drei Jahren oder mit Geldstrafe bestraft wird.

I hereby declare that I have produced the work entitled:

“Quantification and comparison of the neuroarchitecture of deep cerebellar nuclei in the rat and macaque”

submitted for the award of a doctorate, on my own (without external help), have used only the sources and aids indicated and have marked passages included from other works, whether verbatim or in content, as such. I swear upon oath that these statements are true and that I have not concealed anything. I am aware that making a false declaration under oath is punishable by a term of imprisonment of up to three years or by a fine.

Tübingen,

Datum/Date

Unterschrift /Signature

Table of Contents

Introduction.....	9
Aims of this dissertation.....	16
Summary of scientific findings.....	17
Study 1:.....	17
Study 2:.....	17
Study 3:.....	17
Conclusions and outlook.....	19
References.....	21
Appended papers/manuscripts.....	29
Personal contribution statement.....	30
Acknowledgments.....	31
Appendix 1	
Appendix 2	
Appendix 3	

Introduction

The enigma of cerebellar function: beyond motor coordination

The cerebellum has been traditionally viewed as a sensorimotor structure, which is important for movement control and motor learning (Ito 2006, Kawato 1999, Loewenstein et al 2005, Manto et al 2012, Wolpert et al 1998). Disorders of the cerebellum result in movement disturbance that have been described in great detail in clinical and animal models studies (Barash et al 1999, Diener & Dichgans 1992, Glickstein et al 2005, Haines & Manto 2007, Holmes 1917, Holmes 1939, Ignashchenkova et al 2009, Markanday et al 2018). The cerebellum as a comparator is a view that has been shared by many neuroscientists during the last decades. In this model, the difference between the intended movement and the actual movement is compared and used as a motor error to correct subsequent movements. The intended movement is sent as an efferent copy from the motor cortex via pontine nuclei, whereas the sensory inputs provide the afferent feedback and both are then compared within the cerebellum (Apps & Garwicz 2005, Ito 2013, Oscasson 1980). A more recent adaptation implies that the cerebellum is built of modules of internal models that provide a sensory prediction of the movement outcome which is used for comparison with the actual movement for subsequent motor learning (Herzfeld et al 2018).

In the last decades, the cerebellum was also reported to be involved in non-motor functions based on clinical symptoms of cerebellar patients, functional imaging as well as neuroanatomical studies (Dum et al 2002, Dum & Strick 2003, Schmahmann & Sherman 1998, Strick et al 2009). However, it remains unclear how the cerebellum contributes to non-motor function, and whether it uses a similar computational principle as the one that it uses in motor coordination (comparator/sensory predictor).

Modular organization of the cerebellum

The motor function of the cerebellum is integrating motor commands with somatosensory, vestibular, visual and auditory information for coordination and motor learning. Specific motor functions can be ascribed to particular modules within the cerebellum, although the neuronal circuitry of the cerebellum seems to be homogeneous (Apps et al 2018, Diener & Dichgans 1992, Voogd 2014). The Purkinje cells are uniformly aligned in the cerebellar cortex and project to the deep cerebellar nuclei (DCN) in a modular fashion. The DCN is embedded within the white matter and generally, four cerebellar nuclei are distinguished on either side: the fastigial/medial nucleus (MN), globose/posterior interposed nucleus (PIN), emboliform/anterior interposed nucleus (AIN) and dentate/lateral nucleus (LN). An additional

nucleus, the interstitial cell group, is distinguished between the fastigial and globose (Buisseret-Delmas 1988). Seven to nine modules were initially identified on both sides of the carnivores', rodents' and primates' cerebellum (Apps & Hawkes 2009). Each module is composed of one longitudinally organized Purkinje cell zone, its cerebellar or vestibular target nuclei and inferior olive (IO) subdivision. The Purkinje cells within a zone receive their climbing fiber (CF) projections from a particular subdivision of the contralateral IO. In addition the cerebellar or vestibular target nuclei are interconnected with the IO subdivision in a reciprocal fashion.

For example, the C1 and the adjacent C2 zones in the hemispheres, receive CFs from the rostral dorsal accessory olive (DAO) and rostral medial accessory olive (MAO), respectively. Their target nuclei are the emboliform/AIN and the globose/PIN, respectively. They thereby compose two separate modules only allowing for interactions via the parallel fibers (PFs) in the cerebellar cortex. Another two examples are the Purkinje cell zones D1 and D2 in the hemispheres, which target the caudoventral and rostradorsal dentate/LN, respectively and make up another two separate modules. They receive CFs from ventral principal olive (PO) for the D1 zone and the dorsal PO for the D2 zone (Glickstein et al 2011, Oscarsson 1979, Voogd 2014).

The special dentate

Compared to its neighbouring nuclei, the dentate/LN is special in several aspects. It is the most voluminous cerebellar nucleus in primates, located on both sides most laterally and the newest nucleus from the evolutionary perspective. During evolution the overall brain size increases at a characteristic allometric rate with body size (Jerison 1955; Finlay, Darlington et al. 2001). This size increase often follows a regular scaling of its components and reflects a general trend of the brain parts to enlarge conjointly (Roth and Dicke 2005). However, deviations from the regular scaling were crucial to the evolution of the primate brain and the emergence of a different cerebrotyp, as different brain parts evolved at different pace. The emergence of the neocerebellum, which is made up of the cerebellar hemispheres and the dentate/LN accompanies the emergence of the increased surfaces of cerebral neocortex. As demonstrated by Sultan, there is a parallel growth in surface area of both cerebral and cerebellar cortices during evolution (Sultan 2002). Leiner et al have argued that the increase in the size of the dentate/LN is also paralleled by an increase in the cortical areas influenced by cerebellar output (Leiner et al 1986, Leiner et al 1991). Unlike in primates, the more medial part of PIN shows the greatest increase in cetaceans (Voogd & Glickstein 1998). Furthermore, the shape of the enlarged primate dentate/LN changed in a remarkable fashion to a highly folded structure, while the cetaceans' PIN

remained a globous-shaped nucleus (Ogawa 1935). The dentate/LN is the only other highly folded subcortical region (D'Angelo et al 2015, Fujita & Sugihara 2013) besides its tightly connected partner, the PO. The joint expansion of cerebral cortex and the cerebellar modular components: the cerebellar hemispheres, the dentate/LN and the PO, indicates a functional dependence of one upon the other.

The dentate/LN is the main recipient of the Purkinje cell projections from the ipsilateral D1 and D2 zones of the cerebellar hemisphere and is the main source of efferents from the cerebellum (Benagiano et al 2018). According to the connections with the cerebellar cortex, the macaque dentate/LN can be divided into a the rostradorsal region receiving somatotopically organized corticonuclear projections from the skeletomuscular regions of the cerebellar cortex (i.e., anterior and simplex lobule) and a caudoventral region, receiving corticonuclear projections from the visuomotor regions (i.e., crus I and crus II and paraflocculus) of the cerebellar cortex (Glickstein et al 2011). Strick and colleagues (Strick et al 2009) suggested that the dorsal portions of the dentate/LN project to the primary motor and premotor areas of the cerebral cortex while projections to prefrontal and posterior parietal areas of cortex originate from ventral portions of the dentate/LN (Dum & Strick 2003, Middleton & Strick 2001). This subdivision within the dentate/LN agrees with the results of functional MRI studies providing evidence of the activation in distinct regions of the dentate/LN during the execution of either motor or non-motor tasks (Dimitrova et al 2006, Kim et al 1994, Kuper et al 2011).

The special dentate/LN has led to renewed interest in the specific cerebellar computational abilities. Braitenberg and Sultan proposed that the cerebellum temporally coordinates sequences in its inputs. A larger neocerebellum could allow for a larger sequence with more multimodal and diverse input (Braitenberg et al 1997, Sultan 2014, Sultan & Braitenberg 1993, Sultan & Heck 2003). The quest to comprehend the evolutionary driving forces that required a larger human neocerebellum has led to a new hypothesis (Sultan et al 2010): that an enlarged dentate/LN with its folding's and an enlarged surface might be required to reduce the overlap between the sequences and thereby rendering them independent.

Comparative neuroanatomy of the DCN

The dentate/LN connects with the cerebellar hemisphere and IO subdivisions in a modular fashion. Studying the interface —the neurons' soma and dendrites, axons, and synapses—between modular components comparatively within DCN may provide essential clues which adaptations occurred parallel to the expanded and flattened dentate/LN due to the evolutionary selection forces. The DCN are built of a heterogeneous population of neurons, consisting of both large and small projecting neurons and local

interneurons. The projecting neurons can be of variable size while interneurons are usually small (Czubayko et al 2001, Sultan et al 2003a). Comparing the neuroarchitecture within DCN, however, has been limited to Golgi-staining procedure in a qualitative manner in rodents and nonhuman primates (Chan-Palay 1977). Filling the neurons Intracellularly allowed for analyzing soma and dendrites in a quantitative manner in rodent dentate/LN (Sultan et al 2003b). Applying this method to non-human primates is, however, challenging. Therefore, an alternative approach was developed by Sultan and colleagues using 3D quantitative immunohistochemistry (3D-QIHC) which is applicable to both rodents and non-human primates. This method uses confocal laser scanning microscopy (CLSM) to 3D reconstruct fibers on the population level (thereby losing the individual neuronal identity) and extracts information about fiber diameter and length. This approach showed that the phylogenetically newer DCN, i.e., the dentate/LN and the PIN, had a higher dendritic length density than the phylogenetically older parts (MN and AIN) in the rat (Hamodeh et al 2014).

Scaling of dendrites in dentate/LN: from rat to macaque

In general, networks in larger brains have to cover a larger distance with their dendrites and axons leading to a decrease in neuron density and an increase in the dendritic and axonal wiring. This has been shown for example for the neocortex (Braitenberg 2001). However, it is not clear how the wiring in the DCN scales and whether larger DCN have more dendritic and axonal wiring.

In the first study of this thesis (Hamodeh et al 2017) we show that the neuron density is comparable between dentate/LN and its neighbors within one species and follows a regular scaling rule within different species (Hamodeh et al 2017). The comparison of the dendritic wiring, however, demonstrates a specific deviation of the scaling rule within the primates' dentate/LN. The dendritic length per neuron in primate/LN is shorter than predicted. This reduction is also associated with a smaller dendritic region-of-influence (ROI) of these neurons. The smaller dendritic fields would provide an explanation of the unique folded structure of the primate dentate/LN, and also enable more independent network modules to be accommodated inside. However, it is not clear whether this dendritic reduction is also associated with a reduction in the number of synapses.

Excitatory synaptic density in rat DCN

The activity of DCN neurons is jointly regulated by the inhibitory inputs from the Purkinje cells from the cerebellar cortex and the excitatory inputs from CFs and mossy fibers (MFs) from outside of the cerebellum. The frequency and accuracy of DCN neurons spiking is controlled by synchronized inhibitory inputs from the Purkinje cells (Gauck & Jaeger 2000, Gauck & Jaeger 2003). These physiologic property

of the DCN neurons are reflected in their anatomy with the majority of inhibitory synapses (73% in the rat (De Zeeuw & Berrebi 1995) and 63% in cats (Palkovits et al 1977)) located close to the axon initial segment (on the somata and primary dendrites).

The excitatory inputs to the DCN are the collaterals of CFs and MFs and have different sources of origin. In contrast to the CFs, all of which are derived from IO, the MFs stem from multiple brain stem and spinal cord regions. These include such nuclei as the basilar pontine nuclei, the nucleus reticularis tegmentis pontis (Gerrits & Voogd 1987) and the lateral reticular nucleus. Despite the different origins of the fibers and in contrast to the inhibitory synapses (Hioki et al 2003, Hisano et al 2002), almost all the excitatory synapses were found to be on the dendrites of DCN neurons (Gerrits & Voogd 1987, van der Want et al 1987, van der Want & Voogd 1987, Van der Want et al 1989).

Nevertheless, strong excitation through the MFs and/or CFs can directly drive DCN responses and therefore short-circuit the cerebellar cortical processing (Gauck & Jaeger 2000, Gauck & Jaeger 2003). The MFs and CFs projecting to the DCN are therefore important components of the modular circuitry, but have not been quantitatively studied. A previous study has shown that the dendritic length density is higher in phylogenetically newer DCN than the phylogenetically older counterparts in rat (Hamodeh et al 2014) and the excitatory synapses falls on the dendrites. This could imply a larger excitatory connectivity within the phylogenetically newer DCN.

MFs and CFs both utilize glutamate as neurotransmitter to signal the DCN neurons. However they express different vesicular glutamate transporters (vGluTs) to load the glutamate into vesicles for later release. There are two major types of vGluTs in the brain, vGluT1 and vGluT2. Although vGluT1 and vGluT2 have comparable pharmacological properties, they show a complementary expression pattern with vGluT1 in cortical and vGluT2 in subcortical regions. They also correlate with distinct physiological properties in synapses expressing these isoforms. The vGluT1 is usually associated with modulatory synapses with a low probability of vesicular release, while the vGluT2 is usually associated with driving synapses with a high release probability, probably due to their distinct trafficking and recycling mechanisms (Fremeau et al 2001, Li et al 2017, Petrof & Sherman 2013, Sherman 2016, Varoqui et al 2002, Voglmaier et al 2006, Weston et al 2011). The PFs in cerebellar cortex, which express only vGluT1, show paired-pulse enhancement (Perkel et al 1990). In contrast, the CFs, which express exclusively vGluT2 (Hioki et al 2003, Hisano et al 2002), show paired-pulse depression (Konnerth et al 1990, Perkel et al 1990). Each Purkinje cell forms about 175.000 synapses with PFs which, by far, outnumber the synapses from CFs (about 300 synapses per Purkinje cell) (Napper & Harvey 1988, Rossi & Borsello 1993,

Shinoda et al 2000). However the CFs have a powerful effect on the Purkinje cells evoking the so-called complex spikes, while the PFs can only elicit simple spikes in a weak connection to the Purkinje cells. Similarly, the thalamocortical synapses in layer 4 of the mouse somatosensory cortex, expressing vGluT2, is far outnumbered by intracortical synapses utilizing vGluT1. However the differences of release probability between vGluT1 and 2 expressing synapses make the thalamocortical connection more effective than the intracortical connection (Gil et al 1999).

Immunostaining of the vGluT1 and vGluT2 in the DCN region labels all MF and CF terminals and serves as a good approach for quantifying the excitatory synapses in DCN. Based on the mRNA expression pattern of the precerebellar nuclei, we would assume that the vGluT1 labelled synapses would be mostly from the basilar pontine nuclei since this precerebellar nuclei is the only one that express strong vGluT1 mRNA (Geisler et al 2007). The vGluT2 labelled synapses correspond to the sum of CF terminals from IO which express only vGluT2 and the terminals from other precerebellar nuclei, such as the external cuneate nucleus, reticulotegmental nuclei, and spinal trigeminal nucleus, which express strong vGluT2 and weak vGluT1 (Graziano et al 2008, Hisano et al 2002).

In the second part of this dissertation (see study 2, Mao et al 2018), I have quantified the excitatory synapses by using vGluT1 and 2 double staining across the rat DCN. I have shown that there is a higher excitatory synaptic density (mainly the vGluT1 type) in phylogenetically newer DCN, where a higher dendritic wiring was also observed in a previous study.

Scaling of excitatory synaptic density from rat to macaque

Our data shows that 3D-QIHC analysis is robustly able to detect differences in the neuropil of different brain structures and provide considerable sampling scope to survey a whole brain region in detail. When transforming the 3D-QIHC to the primate brain, lipofuscin introduces problems. Lipofuscin is a major source of autofluorescence in the primate brain, even in very young animals and has, for instance, already been detected in cortical neurons of a 5-year-old human subject (Benavides et al 2002). Lipofuscin was also detected in the IO of 3-month-old macaca mulatta. It later appeared in other brain regions and by the time the macaque reached the age of four, it was found in all brain regions examined (Brizzee et al 1974). Lipofuscin is generally assumed to be a major polymerization product of lipids and proteins that accumulates with age in liposomes (Nakano et al 1990, Nakano et al 1989, Oenzil et al 1994). It has a broad excitation and emission spectrum which overlaps with those of the common commercial fluorophores (Barden 1980, Dowson 1982, Dowson et al 1982), thus making it difficult to quantify specific immunostaining in the primate brain (Correa et al 1980). Pretreatments of the brain

sections, such as chemical quenching, photo bleaching, or the combination of the two, were used to remove the lipofuscin like fluorescence in previous studies. These methods can reduce the fluorescence, however, they also affect the efficiency of the immunohistochemistry (IHC) staining (Neumann & Gabel 2002, Schnell et al 1999, Viegas et al 2007). Multispectral imaging was also used to distinguish lipofuscin fluorescence from the stained fluorescence, but this method is very time consuming (Marmorstein et al 2002).

Generally it is difficult to distinguish lipofuscin from the presynapses, given the puncta/granula shape of both structures. By taking advantage of the specific physical property of lipofuscin, broad excitation and emission under laser microscope, we used a specific channel to record the lipofuscin signal only and then masked the lipofuscin signal from our immuno-stained signals. Based on this approach we obtained pure vGluT1 and 2 signals in macaque DCN. This method can also be applied to human brain tissue where lipofuscin is abundant. In the third part of the thesis, I have shown that the excitatory synaptic density (mainly the vGluT1 type) is higher in phylogenetically newer DCN of the macaque, similar to the rat. However, the individual neurons in the macaque dentate/LN have fewer excitatory synapses (mainly the vGluT1 type) than the rat dentate/LN neurons. Taken together, the hyposcaling of both excitatory synapses and dendritic length per neuron could be confirmed in the macaque dentate/LN and reflects its special neuronal architecture.

Aims of this dissertation

The first aim of this dissertation is to search for deviations from normal scaling that could support the notion that primate brains have a special architecture and represent a distinct cerebrotypic (Clark et al 2001, Haug 1970, Watson et al 2012). The dentate nucleus is unusually large, folded and flattened. The evolutionary adaptation that led to this special morphology together with the cellular changes that accompanied it, still remains unknown. To unravel these cellular changes we compared the dentate to the other DCN. This was done by quantifying several neuronal parameters in a systematic and an unbiased approach in the DCN of the rat and macaque, the most commonly used animal models in neuroscience (1st study, Appendix 1).

The second aim of this dissertation is to verify that the structural differences that we observed in the 1st study reflect the synaptic organization of the DCN. The DCN is a critical component of the modular organization and the main output of the cerebellum. Special modifications or adaptations in the DCN could influence the computations of the cerebellum as a whole. In the first study, we showed that the dendritic length density is higher in phylogenetically newer DCN. The aim of this part of the dissertation is to check whether the higher dendritic length density is accompanied with higher excitatory synaptic density in the rat and how these excitatory synapses are quantitatively organized; whether they are of the vGluT1 or 2 type (2nd study, Appendix 2).

Finally, we also wanted to look at the excitatory synaptic organization of the macaque DCN, especially the dentate/LN to see whether the phylogenetically newer DCN has also a higher excitatory synaptic density and compare that between rat and macaque. To achieve this goal we had to design a new approach to remove lipofuscin like fluorescence on our fluorescence stained tissue (3rd study, Appendix 3).

Summary of scientific findings

Study 1

Uncovering specific changes in network wiring underlying the primate cerebrototype

Salah Hamodeh, Ayse Bozkurt, Haian Mao, Fahad Sultan

Brain Struct Funct, DOI 10.1007/s00429-017-1402-6

In this study we analyzed the major hub (DCN) connecting the cerebellar with the cerebral cortex and demonstrate that these hubs could show changes from a predictable scaling (neuron density decrease and dendritic/axonal length increase) to a different scaling mode, with smaller dendritic regions of interest allowing for a larger number of modules in the most enlarged DCN of primates, in dentate/LN. This surprising result, however, is well in keeping with the long known observation of the unique anatomy of the primate dentate/LN from which its name is derived: the flattening and folding of its grey matter into a tooth-shaped structure.

Study 2

Quantitative comparison of vesicular glutamate transporters in rat deep cerebellar nuclei

Haian Mao, Salah Hamodeh, Fahad Sultan

Neuroscience 376 (2018) 152–161

In this paper we quantified the excitatory synapses by vGluT1 and vGluT2 immunolabeling in cerebellar output region (DCN) systematically in an unbiased fashion and showed that the density of vGluT1+ boutons differs significantly within these nuclei (in contrast to the vGluT2+ bouton density). Our results confirmed and extended our previous findings showing that the higher dendritic and axonal wiring in phylogenetically newer DCN is associated with a higher vGluT1+ synaptic density.

Study 3

Quantitative organization of the excitatory synapses of the primate cerebellar nuclei: further evidence for a specialized architecture underlying the primate cerebellum

Haian Mao, Salah Hamodeh, Angelos Skodras, Fahad Sultan

Brain Structure and Function, accepted

In this study we optimized our quantitative approach to the primate brain by using immunohistochemical staining of defined neuron parts (excitatory presynaptic makers) and by taking the lipofuscin autofluorescence into account. The lipofuscin like fluorescence was obtained in a specific channel and subsequently masked from the vGluT1 and 2 stained fluorescence signals. We were therefor able to quantify the excitatory synapses in DCN systematically in an unbiased fashion and compared one of the two main animal models in neuroscience research (rats and macaca mulata). Our results provided important clues of the long known observation of the unique anatomy of the primate dentate/LN and of the difference to its close neighbour, the PIN, a nucleus which is enlarged in cetaceans and reflects another mammalian cerebrotyp in the highly encephalized cetaceans.

Conclusions and outlook

In primates the dentate/LN is the largest and phylogenetically newest part of the DCN and is of particular interest because of its morphological changes in shape during evolution. By combining 3D-QIHC and systematic, random sampling on different neuronal substrates, we compared DCN subregions (phylogenetically newer vs. older parts) in different species (rat vs. macaque). We found that the phylogenetically newer DCN increased in dendritic length density and excitatory synaptic density within the same species. However, when comparing different species, we found a hyposcaling of dendrites and excitatory synapses in individual neuronal level particular in macaque dentate/LN. The neurons in dentate/LN tend to occupy smaller dendritic fields and bear less excitatory synapses. Therefore this hyposcaling in the dentate/LN provides special clues for its morphological changes and for its functional adaptation by allowing for a larger number of independent modules.

We observed the hyposcaling of dentate/LN neurons from two representative animal models (rat and macaque). Applying our method to the cerebella of other mammalian orders, such as tree shrews (scandentia) will allow us to test whether the hyposcaled dendrites are specific for primates. Furthermore, the relationship between the expansion/folding and the pruning of the dendrites in the dentate/LN can also be studied. A simplified assumption would be that dendritic pruning are a secondary effect of increased mechanic tension due to the expansion of the dentate/LN in primates. Several genes, such as *Trnp1* and *ARHGAP11B* were identified in regulating the cerebral cortex expansion (Florio et al 2015, Stahl et al 2013). Transgenic animal model systems can be built by searching genes responsible for the dentate/LN expansion and quantifying the dendritic fields when the expression level of the candidate gene(s) is disrupted to test this assumption.

Our results showed a higher vGluT1+ synaptic density in phylogenetic newer DCN which fits with the general distribution pattern of vGluT1 in the phylogenetically newer and more modifiable parts of the brain (Herzog et al 2004, Hisano 2003). However, the comparable vGluT1 and 2+ synaptic density in the DCN is likely due to the presence of two separate pathways: the CFs and MFs which process information differently, with the CFs having a much lower firing frequency than the MFs (Delvendahl & Hallermann 2016, Sultan et al 2012). However, the presence of vGluT2 in a subpopulation of MFs complicates this view and further studies are required to quantify the proportion of MFs expressing vGluT2 and clarify which brain regions they origin from. A study by Boele and colleagues showed an increase of vGluT2 MF presynapses to the DCN from basilar pontine nuclei following Pavlovian eyeblink conditioning (Boele et al 2013). So far, it remains unclear whether this kind of learning in the DCN requires the sprouting and

formation of new vGluT1 synapses, or whether it is achieved by an increase in vGluT2 levels in vGluT1 MF collaterals. The former has been shown to underlie synaptic plasticity in other parts of the brain (Black et al 1990), while the latter would point to a novel mechanism of synaptic plasticity that has not been described so far.

References

- Apps R, Garwicz M. 2005. Anatomical and physiological foundations of cerebellar information processing. *Nature Reviews Neuroscience* 6: 297
- Apps R, Hawkes R. 2009. Cerebellar cortical organization: a one-map hypothesis. *Nature reviews. Neuroscience* 10: 670-81
- Apps R, Hawkes R, Aoki S, Bengtsson F, Brown AM, et al. 2018. Cerebellar Modules and Their Role as Operational Cerebellar Processing Units. *Cerebellum*
- Barash S, Melikyan A, Sivakov A, Zhang M, Glickstein M, Thier P. 1999. Saccadic dysmetria and adaptation after lesions of the cerebellar cortex. *J Neurosci* 19: 10931-9
- Barden H. 1980. Interference filter microfluorometry of neuromelanin and lipofuscin in human brain. *Journal of neuropathology and experimental neurology* 39: 598-605
- Benagiano V, Rizzi A, Lorusso L, Flace P, Saccia M, et al. 2018. The functional anatomy of the cerebrocerebellar circuit: A review and new concepts. *The Journal of comparative neurology* 526: 769-89
- Benavides SH, Monserrat AJ, Farina S, Porta EA. 2002. Sequential histochemical studies of neuronal lipofuscin in human cerebral cortex from the first to the ninth decade of life. *Archives of gerontology and geriatrics* 34: 219-31
- Black JE, Isaacs KR, Anderson BJ, Alcantara AA, Greenough WT. 1990. Learning causes synaptogenesis, whereas motor activity causes angiogenesis, in cerebellar cortex of adult rats. *Proceedings of the National Academy of Sciences of the United States of America* 87: 5568-72
- Boele HJ, Koekkoek SK, De Zeeuw CI, Ruigrok TJ. 2013. Axonal sprouting and formation of terminals in the adult cerebellum during associative motor learning. *The Journal of neuroscience : the official journal of the Society for Neuroscience* 33: 17897-907
- Braitenberg V. 2001. Brain size and number of neurons: an exercise in synthetic neuroanatomy. *Journal of computational neuroscience* 10: 71-7
- Braitenberg V, Heck D, Sultan F. 1997. The detection and generation of sequences as a key to cerebellar function: experiments and theory. *The Behavioral and brain sciences* 20: 229-45; discussion 45-77
- Brizze KR, Ordly JM, Kaack B. 1974. Early appearance and regional differences in intraneuronal and extraneuronal lipofuscin accumulation with age in the brain of a nonhuman primate (*Macaca mulatta*). *Journal of gerontology* 29: 366-81

- Buisseret-Delmas C. 1988. Sagittal organization of the olivocerebellonuclear pathway in the rat. I. Connections with the nucleus fastigii and the nucleus vestibularis lateralis. *Neuroscience research* 5: 475-93
- Chan-Palay V. 1977. *Cerebellar Dentate Nucleus: Organization, Cytology and Transmitters*. Berlin/Heidelberg/New York: Springer-Verlag.
- Clark DA, Mitra PP, Wang SS. 2001. Scalable architecture in mammalian brains. *Nature* 411: 189-93
- Correa FM, Innis RB, Rouot B, Pasternak GW, Snyder SH. 1980. Fluorescent probes of alpha- and beta-adrenergic and opiate receptors: biochemical and histochemical evaluation. *Neuroscience letters* 16: 47-53
- Czubayko U, Sultan F, Thier P, Schwarz C. 2001. Two types of neurons in the rat cerebellar nuclei as distinguished by membrane potentials and intracellular fillings. *Journal of neurophysiology* 85: 2017-29
- D'Angelo E, Galliano E, De Zeeuw CI. 2015. Editorial: The Olivo-Cerebellar System. *Frontiers in neural circuits* 9: 66
- De Zeeuw CI, Berrebi AS. 1995. Postsynaptic targets of Purkinje cell terminals in the cerebellar and vestibular nuclei of the rat. *The European journal of neuroscience* 7: 2322-33
- Delvendahl I, Hallermann S. 2016. The Cerebellar Mossy Fiber Synapse as a Model for High-Frequency Transmission in the Mammalian CNS. *Trends in neurosciences* 39: 722-37
- Diener HC, Dichgans J. 1992. Pathophysiology of cerebellar ataxia. *Movement disorders : official journal of the Movement Disorder Society* 7: 95-109
- Dimitrova A, de Greiff A, Schoch B, Gerwig M, Frings M, et al. 2006. Activation of cerebellar nuclei comparing finger, foot and tongue movements as revealed by fMRI. *Brain research bulletin* 71: 233-41
- Dowson JH. 1982. Neuronal lipofuscin accumulation in ageing and alzheimer dementia: a pathogenic mechanism? *The British journal of psychiatry : the journal of mental science* 140: 142-8
- Dowson JH, Armstrong D, Koppang N, Lake BD, Jolly RD. 1982. Autofluorescence emission spectra of neuronal lipopigment in animal and human ceroidoses (ceroid-lipofuscinoses). *Acta neuropathologica* 58: 152-6
- Dum RP, Li C, Strick PL. 2002. Motor and nonmotor domains in the monkey dentate. *Annals of the New York Academy of Sciences* 978: 289-301
- Dum RP, Strick PL. 2003. An unfolded map of the cerebellar dentate nucleus and its projections to the cerebral cortex. *Journal of neurophysiology* 89: 634-9

- Florio M, Albert M, Taverna E, Namba T, Brandl H, et al. 2015. Human-specific gene ARHGAP11B promotes basal progenitor amplification and neocortex expansion. *Science* 347: 1465-70
- Fremeau RT, Jr., Troyer MD, Pahner I, Nygaard GO, Tran CH, et al. 2001. The expression of vesicular glutamate transporters defines two classes of excitatory synapse. *Neuron* 31: 247-60
- Fujita H, Sugihara I. 2013. Branching patterns of olivocerebellar axons in relation to the compartmental organization of the cerebellum. *Frontiers in neural circuits* 7
- Gauck V, Jaeger D. 2000. The control of rate and timing of spikes in the deep cerebellar nuclei by inhibition. *The Journal of neuroscience : the official journal of the Society for Neuroscience* 20: 3006-16
- Gauck V, Jaeger D. 2003. The contribution of NMDA and AMPA conductances to the control of spiking in neurons of the deep cerebellar nuclei. *The Journal of neuroscience : the official journal of the Society for Neuroscience* 23: 8109-18
- Geisler S, Derst C, Veh RW, Zahm DS. 2007. Glutamatergic afferents of the ventral tegmental area in the rat. *The Journal of neuroscience : the official journal of the Society for Neuroscience* 27: 5730-43
- Gerrits NM, Voogd J. 1987. The projection of the nucleus reticularis tegmenti pontis and adjacent regions of the pontine nuclei to the central cerebellar nuclei in the cat. *The Journal of comparative neurology* 258: 52-69
- Gil Z, Connors BW, Amitai Y. 1999. Efficacy of thalamocortical and intracortical synaptic connections: quanta, innervation, and reliability. *Neuron* 23: 385-97
- Glickstein M, Sultan F, Voogd J. 2011. Functional localization in the cerebellum. *Cortex* 47: 59-80
- Glickstein M, Waller J, Baizer JS, Brown B, Timmann D. 2005. Cerebellum lesions and finger use. *Cerebellum* 4: 189-97
- Graziano A, Liu XB, Murray KD, Jones EG. 2008. Vesicular glutamate transporters define two sets of glutamatergic afferents to the somatosensory thalamus and two thalamocortical projections in the mouse. *The Journal of comparative neurology* 507: 1258-76
- Haines DE, Manto MU. 2007. Clinical symptoms of cerebellar disease and their interpretation. *Cerebellum* 6: 360-74
- Hamodeh S, Bozkurt A, Mao H, Sultan F. 2017. Uncovering specific changes in network wiring underlying the primate cerebrotypes. *Brain structure & function*
- Hamodeh S, Sugihara I, Baizer J, Sultan F. 2014. Systematic analysis of neuronal wiring of the rodent deep cerebellar nuclei reveals differences reflecting adaptations at the neuronal circuit and internuclear level. *J Comp Neurol* 522: 2481-97

- Haug H. 1970. Quantitative data in neuroanatomy. *Progress in brain research* 33: 113-27
- Herzfeld DJ, Kojima Y, Soetedjo R, Shadmehr R. 2018. Encoding of error and learning to correct that error by the Purkinje cells of the cerebellum. *Nature neuroscience* 21: 736-43
- Herzog E, Landry M, Buhler E, Bouali-Benazzouz R, Legay C, et al. 2004. Expression of vesicular glutamate transporters, VGLUT1 and VGLUT2, in cholinergic spinal motoneurons. *The European journal of neuroscience* 20: 1752-60
- Hioki H, Fujiyama F, Taki K, Tomioka R, Furuta T, et al. 2003. Differential distribution of vesicular glutamate transporters in the rat cerebellar cortex. *Neuroscience* 117: 1-6
- Hisano S. 2003. Vesicular glutamate transporters in the brain. *Anatomical science international* 78: 191-204
- Hisano S, Sawada K, Kawano M, Kanemoto M, Xiong G, et al. 2002. Expression of inorganic phosphate/vesicular glutamate transporters (BNPI/VGLUT1 and DNPI/VGLUT2) in the cerebellum and precerebellar nuclei of the rat. *Brain research. Molecular brain research* 107: 23-31
- HOLMES G. 1917. THE SYMPTOMS OF ACUTE CEREBELLAR INJURIES DUE TO GUNSHOT INJURIES. *Brain : a journal of neurology* 40: 461-535
- HOLMES G. 1939. THE CEREBELLUM OF MAN1. *Brain : a journal of neurology* 62: 1-30
- Ignashchenkova A, Dash S, Dicke PW, Haarmeier T, Glickstein M, Thier P. 2009. Normal spatial attention but impaired saccades and visual motion perception after lesions of the monkey cerebellum. *J Neurophysiol* 102: 3156-68
- Ito M. 2006. Cerebellar circuitry as a neuronal machine. *Progress in neurobiology* 78: 272-303
- Ito M. 2013. Error detection and representation in the olivo-cerebellar system. *Front Neural Circuits* 7: 1
- Kawato M. 1999. Internal models for motor control and trajectory planning. *Current opinion in neurobiology* 9: 718-27
- Kim SG, Ugurbil K, Strick PL. 1994. Activation of a cerebellar output nucleus during cognitive processing. *Science* 265: 949-51
- Konnerth A, Llano I, Armstrong CM. 1990. Synaptic currents in cerebellar Purkinje cells. *Proceedings of the National Academy of Sciences of the United States of America* 87: 2662-5
- Kuper M, Dimitrova A, Thurling M, Maderwald S, Roths J, et al. 2011. Evidence for a motor and a non-motor domain in the human dentate nucleus--an fMRI study. *NeuroImage* 54: 2612-22
- Leiner HC, Leiner AL, Dow RS. 1986. Does the cerebellum contribute to mental skills? *Behav Neurosci* 100: 443-54

- Leiner HC, Leiner AL, Dow RS. 1991. The human cerebro-cerebellar system: its computing, cognitive, and language skills. *Behav Brain Res* 44: 113-28
- Li H, Santos MS, Park CK, Dobry Y, Voglmaier SM. 2017. VGLUT2 Trafficking Is Differentially Regulated by Adaptor Proteins AP-1 and AP-3. *Frontiers in cellular neuroscience* 11: 324
- Loewenstein Y, Mahon S, Chadderton P, Kitamura K, Sompolinsky H, et al. 2005. Bistability of cerebellar Purkinje cells modulated by sensory stimulation. *Nature neuroscience* 8: 202-11
- Manto M, Bower JM, Conforto AB, Delgado-García JM, Da Guarda SNF, et al. 2012. Consensus paper: roles of the cerebellum in motor control—the diversity of ideas on cerebellar involvement in movement. *The Cerebellum* 11: 457-87
- Markanday A, Messner J, Thier P. 2018. A loss of a velocity-duration trade-off impairs movement precision in patients with cerebellar degeneration. *The European journal of neuroscience* 48: 1976-89
- Marmorstein AD, Marmorstein LY, Sakaguchi H, Hollyfield JG. 2002. Spectral profiling of autofluorescence associated with lipofuscin, Bruch's Membrane, and sub-RPE deposits in normal and AMD eyes. *Investigative ophthalmology & visual science* 43: 2435-41
- Middleton FA, Strick PL. 2001. Cerebellar projections to the prefrontal cortex of the primate. *The Journal of neuroscience : the official journal of the Society for Neuroscience* 21: 700-12
- Nakano M, Mizuno T, Gotoh S. 1990. Accumulation of cardiac lipofuscin in mammals: correlation between sexual maturation and the first appearance of lipofuscin. *Mechanisms of ageing and development* 52: 93-106
- Nakano M, Mizuno T, Katoh H, Gotoh S. 1989. Age-related accumulation of lipofuscin in myocardium of Japanese monkey (*Macaca fuscata*). *Mechanisms of ageing and development* 49: 41-8
- Napper RM, Harvey RJ. 1988. Number of parallel fiber synapses on an individual Purkinje cell in the cerebellum of the rat. *The Journal of comparative neurology* 274: 168-77
- Neumann M, Gabel D. 2002. Simple method for reduction of autofluorescence in fluorescence microscopy. *The journal of histochemistry and cytochemistry : official journal of the Histochemistry Society* 50: 437-9
- Oenzil F, Kishikawa M, Mizuno T, Nakano M. 1994. Age-related accumulation of lipofuscin in three different regions of rat brain. *Mechanisms of ageing and development* 76: 157-63
- Ogawa T. 1935. Beitr~ ige zur vergleichenden Anatomie des Zentralnervensystems der Wassers~ iugetiere: Ober die Kleinhirnkerne der Pinnipeden und Zetazeen. *Arb. anat. Inst. Semtai* 17: 63-136

- Oscarsson O. 1979. Functional units of the cerebellum - sagittal zones and microzones. *Trends in neurosciences* 2: 143-45
- Oscasson O. 1980. Functional organization of olivary projection to the cerebellar anterior lobe. *The Inferior Olivary Nucleus, Anatomy and Physiology*
- Palkovits M, Mezey E, Hamori J, Szentagothai J. 1977. Quantitative histological analysis of the cerebellar nuclei in the cat. I. Numerical data on cells and on synapses. *Experimental brain research* 28: 189-209
- Perkel DJ, Hestrin S, Sah P, Nicoll RA. 1990. Excitatory synaptic currents in Purkinje cells. *Proceedings. Biological sciences / The Royal Society* 241: 116-21
- Petrof I, Sherman SM. 2013. Functional significance of synaptic terminal size in glutamatergic sensory pathways in thalamus and cortex. *The Journal of physiology* 591: 3125-31
- Rossi F, Borsello T. 1993. Ectopic Purkinje cells in the adult rat: olivary innervation and different capabilities of migration and development after grafting. *The Journal of comparative neurology* 337: 70-82
- Schmahmann JD, Sherman JC. 1998. The cerebellar cognitive affective syndrome. *Brain : a journal of neurology* 121 (Pt 4): 561-79
- Schnell SA, Staines WA, Wessendorf MW. 1999. Reduction of lipofuscin-like autofluorescence in fluorescently labeled tissue. *The journal of histochemistry and cytochemistry : official journal of the Histochemistry Society* 47: 719-30
- Sherman SM. 2016. Thalamus plays a central role in ongoing cortical functioning. *Nature neuroscience* 19: 533-41
- Shinoda Y, Sugihara I, Wu HS, Sugiuchi Y. 2000. The entire trajectory of single climbing and mossy fibers in the cerebellar nuclei and cortex. *Progress in brain research* 124: 173-86
- Stahl R, Walcher T, De Juan Romero C, Pilz GA, Cappello S, et al. 2013. Trnp1 regulates expansion and folding of the mammalian cerebral cortex by control of radial glial fate. *Cell* 153: 535-49
- Strick PL, Dum RP, Fiez JA. 2009. Cerebellum and nonmotor function. *Annu Rev Neurosci* 32: 413-34
- Sultan F. 2002. Analysis of mammalian brain architecture. *Nature* 415: 133-4
- Sultan F. 2014. From cerebellar texture to movement optimization. *Biological Cybernetics* 108: 677-88
- Sultan F, Augath M, Hamodeh S, Murayama Y, Oeltermann A, et al. 2012. Unravelling cerebellar pathways with high temporal precision targeting motor and extensive sensory and parietal networks. *Nature communications* 3: 924

- Sultan F, Braitenberg V. 1993. Shapes and sizes of different mammalian cerebella. A study in quantitative comparative neuroanatomy. *J Hirnforsch* 34: 79-92
- Sultan F, Czubayko U, Thier P. 2003a. Morphological classification of the rat lateral cerebellar nuclear neurons by principal component analysis. *The Journal of comparative neurology* 455: 139-55
- Sultan F, Czubayko U, Thier P. 2003b. Morphological classification of the rat lateral cerebellar nuclear neurons by principal component analysis. *The Journal of Comparative Neurology* 455: 139-55
- Sultan F, Hamodeh S, Baizer JS. 2010. The human dentate nucleus: a complex shape untangled. *Neuroscience* 167: 965-8
- Sultan F, Heck D. 2003. Detection of sequences in the cerebellar cortex: numerical estimate of the possible number of tidal-wave inducing sequences represented. *J Physiology-Paris* 97: 591-600
- van der Want JJ, Gerrits NM, Voogd J. 1987. Autoradiography of mossy fiber terminals in the fastigial nucleus of the cat. *The Journal of comparative neurology* 258: 70-80
- van der Want JJ, Voogd J. 1987. Ultrastructural identification and localization of climbing fiber terminals in the fastigial nucleus of the cat. *The Journal of comparative neurology* 258: 81-90
- Van der Want JJ, Wiklund L, Guegan M, Ruigrok T, Voogd J. 1989. Anterograde tracing of the rat olivocerebellar system with Phaseolus vulgaris leucoagglutinin (PHA-L). Demonstration of climbing fiber collateral innervation of the cerebellar nuclei. *The Journal of comparative neurology* 288: 1-18
- Varoqui H, Schafer MK, Zhu H, Weihe E, Erickson JD. 2002. Identification of the differentiation-associated Na⁺/PI transporter as a novel vesicular glutamate transporter expressed in a distinct set of glutamatergic synapses. *The Journal of neuroscience : the official journal of the Society for Neuroscience* 22: 142-55
- Viegas MS, Martins TC, Seco F, do Carmo A. 2007. An improved and cost-effective methodology for the reduction of autofluorescence in direct immunofluorescence studies on formalin-fixed paraffin-embedded tissues. *European journal of histochemistry : EJH* 51: 59-66
- Voglmaier SM, Kam K, Yang H, Fortin DL, Hua Z, et al. 2006. Distinct endocytic pathways control the rate and extent of synaptic vesicle protein recycling. *Neuron* 51: 71-84
- Voogd J. 2014. What we do not know about cerebellar systems neuroscience. *Frontiers in systems neuroscience* 8: 227
- Voogd J, Glickstein M. 1998. The anatomy of the cerebellum. *Trends in neurosciences* 21: 370-5

Watson C, Provis J, Herculano-Houzel S. 2012. What determines motor neuron number? Slow scaling of facial motor neuron numbers with body mass in marsupials and primates. *Anat Rec (Hoboken)* 295: 1683-91

Weston MC, Nehring RB, Wojcik SM, Rosenmund C. 2011. Interplay between VGLUT isoforms and endophilin A1 regulates neurotransmitter release and short-term plasticity. *Neuron* 69: 1147-59

Wolpert DM, Miall RC, Kawato M. 1998. Internal models in the cerebellum. *Trends in cognitive sciences* 2: 338-47

Appended papers/manuscripts

Appendix 1: Salah Hamodeh, Ayse Bozkurt, Haian Mao, Fahad Sultan. (2017) Uncovering specific changes in network wiring underlying the primate cerebrotype. *Brain Struct Funct*, DOI 10.1007/s00429-017-1402-6

Appendix 2: Haian Mao, Salah Hamodeh, Fahad Sultan. (2018) Quantitative Comparison Of Vesicular Glutamate Transporters in rat Deep Cerebellar Nuclei. *Neuroscience* 376 152–161

Appendix 3: Haian Mao, Salah Hamodeh, Angelos Skodras, Fahad Sultan. Quantitative organization of the excitatory synapses of the primate cerebellar nuclei: further evidence for a specialized architecture underlying the primate cerebellum. *Brain Structure and Function*, accepted

Personal contribution statement

Study 1:

Salah Hamodeh, Ayse Bozkurt, Haian Mao, Fahad Sultan. (2017) Uncovering specific changes in network wiring underlying the primate cerebrotype. Brain Struct Funct, DOI 10.1007/s00429-017-1402-6

SH and **HM** conducted the histology and, together with FS, analyzed the data. AB counted the cells. FS wrote the manuscript, designed the project, and was responsible for securing funding. All authors reviewed the manuscript.

Study 2:

Haian Mao, Salah Hamodeh, Fahad Sultan. (2018) Quantitative Comparison Of Vesicular Glutamate Transporters in rat Deep Cerebellar Nuclei. Neuroscience 376 152–161

HM and SH conducted the experiments and together with FS analyzed the data and wrote the manuscript. FS designed the project and provided for funding. All authors reviewed the manuscript.

Study 3:

Haian Mao, Salah Hamodeh, Angelos Skodras, Fahad Sultan. Quantitative organization of the excitatory synapses of the primate cerebellar nuclei: further evidence for a specialized architecture underlying the primate cerebellum. Brain Structure and Function, accepted

SH sectioned the macaque cerebellum and AS helped with the LSM multi-channel setup and lambda mode scanning. **HM** conducted the staining and acquired the data. **HM** and FS analyzed the data and wrote the manuscript. FS designed the project and provided for funding. All authors reviewed the manuscript.

Acknowledgments

First of all, I would like to thank my supervisor Prof. Fahad Sultan, for providing me the opportunity to work at the Department of Cognitive Neurology of the Hertie Institute for Clinical Brain Research. I had a lot of freedom to perform my experiments and whenever problems turn up, he was always the right person to turn for help. This work could not have been done without his support, supervision and guidance throughout the project and thesis. I am really very grateful to him not only for his academic guidance but also for his support outside the academics.

I would also like to thank my advisory board members. Prof. Hans-Peter Thier and Prof. Almut Schüz for their valuable advices and suggestions. I would like to thank Dr. Peter W. Dicke, Dr. Friedemann Bunjes and Ute Großhennig for their technical support.


I would like to thank all the lab members in the Department of Cognitive Neurology for their help and useful feedback during my talks. I am especially grateful to Salah Hamodeh for a fruitful collaboration and Akshay Markanday for his valuable comments on the thesis. I really enjoyed working with all the lab members and I had wonderful time during my thesis work.

I am beyond grateful to my family, especially to my husband Shengjun Wen and my son Youde Wen. Without their endless love and constant support over the years, I could not have accomplished this feat.

Appendix 1:

Salah Hamodeh, Ayse Bozkurt, Haian Mao, Fahad Sultan. (2017) Uncovering specific changes in network wiring underlying the primate cerebrotype. Brain Struct Funct, DOI 10.1007/s00429-017-1402-6

Uncovering specific changes in network wiring underlying the primate cerebrotype

Salah Hamodeh¹ · Ayse Bozkurt¹ · Haian Mao¹ · Fahad Sultan^{1,2} 

Received: 19 January 2017 / Accepted: 2 March 2017
© The Author(s) 2017. This article is an open access publication

Abstract Regular scaling of brain networks during evolution has been proposed to be the major process leading to enlarged brains. Alternative views, however, suggest that deviations from regular scaling were crucial to the evolution of the primate brain and the emergence of different cerebrotypes. Here, we examined the scaling within the major link between the cerebellum and the cerebral cortex by studying the deep cerebellar nuclei (DCN). We compared the major axonal and dendritic wiring in the DCN of rodents and monkeys in search of regular scaling. We were able to confirm regular scaling within the density of neurons, the general dendritic length per neuron and the Purkinje cell axon length. However, we also observed specific modification of the scaling rules within the primates' largest and phylogenetically newest DCN, the dentate nucleus (LN/dentate). Our analysis shows a deviation from regular scaling in the predicted dendritic length per neuron in the LN/dentate. This reduction in the dendritic length is also associated with a smaller dendritic region-of-influence of these neurons. We also detected specific changes in the dendritic diameter distribution, supporting the theory that there is a shift in the neuronal population of the LN/dentate towards neurons that exhibit spatially restricted, clustered branching trees. The smaller dendritic fields would enable a larger number of network modules

to be accommodated in the primate LN/dentate and would provide an explanation for the unique folded structure of the primate LN/dentate. Our results show that, in some brain regions, connectivity maximization (i.e., an increase of dendritic fields) is not the sole optimum and that increases in the number of network modules may be important for the emergence of a divergent primate cerebrotype.

Keywords Cerebellar nuclei · Dentate nucleus · Motor systems · Purkinje cells · Quantitative immunohistochemistry · 3D reconstructions · Comparative neuroanatomy

Abbreviations

AIN	Anterior interposed nucleus
asf	Area sampling fraction
CI	Confidence interval
D_{dia}	Dendritic diameter
Dl_{dens}	Dendritic length density
Dl_{neu}	Dendritic length per neuron
dROI	Dendritic regions of influence
hsf	Height sampling fraction
LN/dentate	Lateral nucleus/dentate nucleus
LVN	Lateral vestibular nucleus
MAP2	Microtubule-associated protein 2a, b
MN	Medial nucleus
PIN	Posterior part of interposed nucleus
PCax	PCP2-stained Purkinje cell axons
PCP2	Purkinje cell-specific protein 2
ΣQ	Total counted neuron/glia number
ssf	Slice sampling fraction
Th_{ref}	Section depth used to calculate fiber densities within 3D-QIHC probes
V_{DCN}	Volume of DCN per side
Vf_{dend}	Volume fraction of dendrites

Electronic supplementary material The online version of this article (doi:10.1007/s00429-017-1402-6) contains supplementary material, which is available to authorized users.

✉ Fahad Sultan
fahad.sultan@umu.se

¹ Department of Cognitive Neurology, HIH for Clinical Brain Research, Otfried-Müller-Str. 27, 72076 Tübingen, Germany

² Department of Integrative Medical Biology, Umeå University, Linnéus väg 9, 901 87 Umeå, Sweden

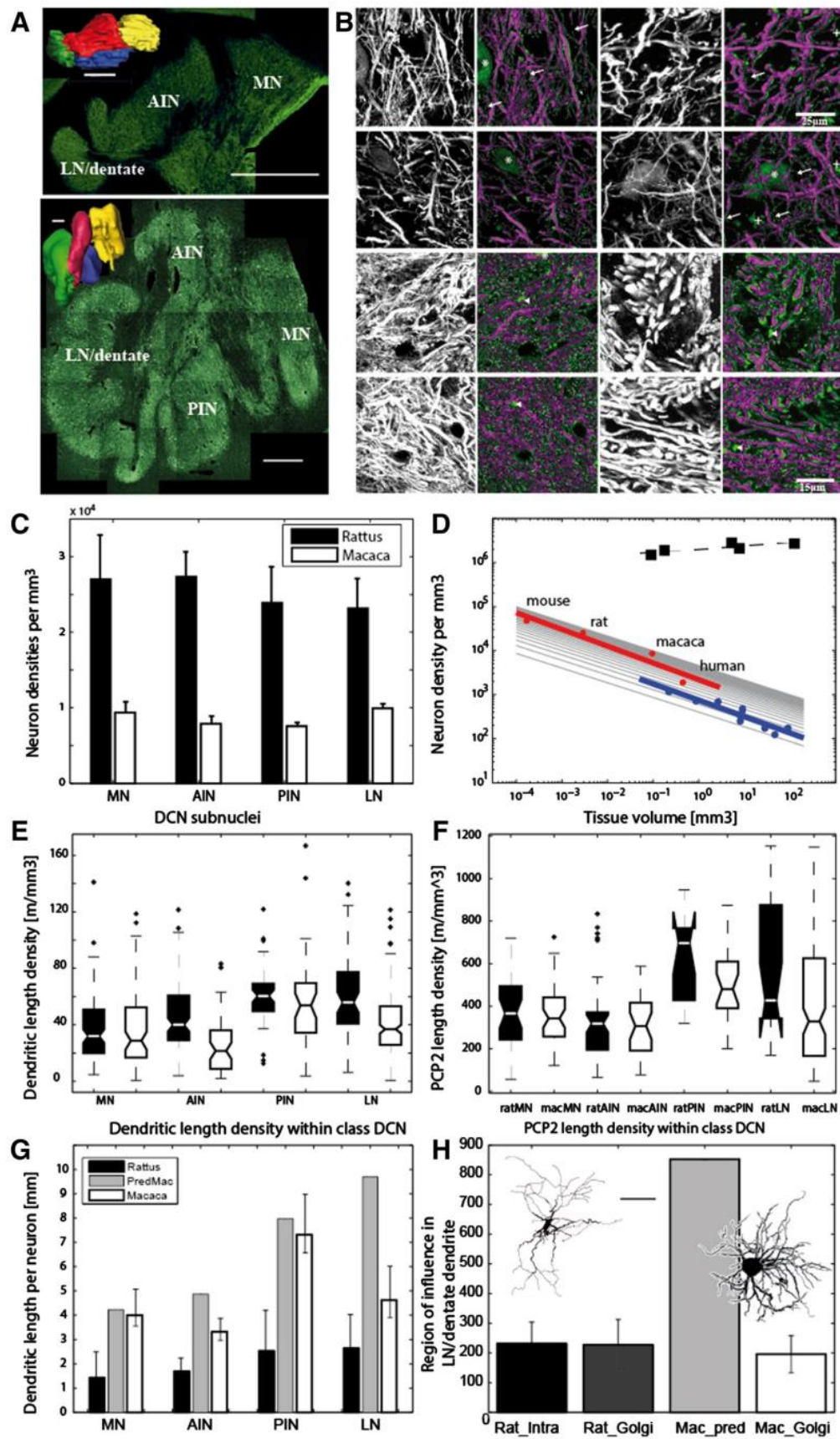


Fig. 1 Comparison of the rat and macaque DCN. **a** Composite overviews of fluorescent MAP2 immunohistochemistry of the rat (*upper; coronal section*) and rhesus monkey (*lower; horizontal section*) DCN. Surface reconstructions of the rat (*upper*) and macaque (*lower*) DCN are also shown. The surfaces are color coded for the different DCN: MN, *yellow*; AIN, *red*; PIN, *blue* and LN/dentate, *green*. Scale bars correspond to 1 mm. **b** Examples of MAP2 and PCP2 stains acquired with the laser confocal microscope. *Black and white images* are maximal intensity projections through a stack of slices. *Magenta and green images* show the outcome of the automatic fiber and diameter reconstruction (*Magenta*) overlaid on the maximal intensity projection (*green*). The view axis was tilted slightly sideways to enable observation of the underlying maximal intensity projection. *Upper two rows* are MAP2 stains, while the *lower two rows* are PCP2. *Left two columns* are images from the rat and 1st and 3rd rows are from the AIN, while 2nd and 4th are from the LN/dentate. MAP2-stained somata were manually removed (marked with *asterisks*) from the reconstruction outcome. (*Plus*) marks lipofuscin that was also removed manually. *Arrow mark* subthreshold fibers and arrow heads mark other structures that the reconstruction algorithm failed to recognize. Scale bar for the *upper two rows* is 25 and 15 μm for the *lower two rows*. **c** Counts of neurons in rats ($n=4$) and macaques ($n=2$) with the optical fractionator method yielded highly significant different densities between the two species. A two-way ANOVA showed significant differences on the species level, but not on the subnuclei level (F value 28.3, $df=1$, $p<0.0001$ vs. F value 0.25, $df=3$, $p>0.86$). **d** Double logarithmic plot of the dependence of cerebellar neuron density on tissue volume. DCN (*red*) neurons show a density drop in larger brains comparable to that observed in Purkinje cells (*blue*). Regression fits showed similar results in DCN neurons and Purkinje cells (DCN: $y = -0.38046 (\pm 0.084)x + 3.3401$; $r^2 = 0.91$, $p < 0.05$; Purkinje cells: $y = -0.3718 (\pm 0.053)x + 2.8728$; $r^2 = -0.86$, $p < 0.001$). *Arrays of black lines* are also plotted for a comparison with a slope of $-1/3$. The data for cerebellar granule cells (*square, black*) which do not show a drop in density in larger brains: ($y = 0.073435 (\pm 0.027)x + 6.303$; $r^2 = 0.71$, $p = 0.072666$) are also plotted. Sources of additional neuron densities are listed in “[Material and methods](#)”. **e, f** Quantification of fibers labeled with MAP2 (dendrites, *E*) and PCP2 (Purkinje cell axons: PCax, *F*) showed higher values for the axons. In contrast to the neuron densities, DCN classification now had an additional significant effect, thus explaining the variability of the dendrites (two-factorial ANOVA with F values 14.5 vs. 19.9, $df=1$ vs. $df=4$ and $p < 10^{-5}$ vs. $p < 10^{-11}$ for the factors DCN class vs. species origin) and the PCax (two-factorial ANOVA yielded F values 57.6 vs. 5.1 and $p = 10^{-37}$ vs. $p \leq .024$ for the factors DCN class vs. species origin) in our probes. The average dendritic and PCax length densities were generally lower in the phylogenetically older DCN (i.e., the MN and the AIN), thereby contributing to the variability in the probes. **g** Comparison of the dendritic length per neuron for different subnuclei and for the two species. Dendritic length densities were normalized by neuron densities for each DCN to obtain the dendritic length per neuron. Predictions for the monkey were derived by multiplying the values obtained from the rat with the factor of volume increase to the power of $1/3$ obtained from the different subnuclei. *Error bars* for the rat and monkey show the 95% confidence region obtained from the ratios of the two measured parameters (e.g., dendritic length density and neuron density). The prediction for the MN and PIN were well within the CI. The AIN prediction was somewhat higher than the CI of the monkey values. By contrast, the prediction for the LN/dentate was well above that of the CI established by our probes (only 4.8 vs. a prediction of 9.7 mm). **h** Comparison of the diameter of region-of-influence (dROI) obtained for rat and monkey dendritic trees. Rat_intra denotes dROI diameters obtained from 3D-reconstructed intracellularly filled neurons ($n=35$) and refers to the diameters we obtain when 2D images of

those neurons are analyzed by taking the area from the boundary spanned by the outer tips of the dendrites. Rat_golgi denotes diameters obtained with the same approach, but from Golgi-stained neurons ($n=27$ for the rats; $n=54$ for the monkey). The difference between rat and monkey (Mac_Golgi) was not significant (mean of 227 μm compared to 196 μm , respectively and t test $p=0.059$). *Inlet to the left* intracellularly stained neuron from the rat. *Inlet to the right* neurons showing a small dROI with clustered dendrites from the monkey’s LN/dentate. Scale bar corresponds to 100 μm for the *left* and 50 μm for the *right* neuron

Introduction

Brains of different sizes can show a remarkable degree of regular scaling (Finlay et al. 2001; Yopak et al. 2010). Brain scaling simply refers to the observation that brains increased in size during evolution. Larger brains can, in principle, be due to an increase in their constituent elements or in the size of the elements: two processes that compete for the limited space available. In addition, most mammalian networks have a large intrinsic excitatory connectivity that is critical for their function (Abeles 1991; Braitenberg and Schüz 1991; Schüz and Sultan 2009) and which is, therefore, exploited to the utmost (Chklovskii et al. 2002). The upscaling of such networks also leads to an increase in the dendritic and axonal wiring required to connect larger brains, thereby causing a decrease in neuron density (Braitenberg 2001).

The mammalian brain, however, is composed of several different network architectures. One radically different type of network is found in the cerebellum. Here, the granule cell axons (the parallel fibers) show a constant length irrespective of brain size, and the granule cell density remains constant (Schüz and Sultan 2009). This difference in scaling leads to an increase in the proportion of granule cells of all neurons to 80% in humans (Andersen et al. 2003; Azevedo et al. 2009), despite the cerebellum occupying only 15% of the whole volume of the brain.

Precisely how this interlinkage between different scaling networks functions has not yet been established. We speculated that we could gain important insight on this question by studying the scaling between the cerebral and cerebellar cortex at their connecting hub. The DCN are a major hub which connect the cerebellar cortex with the cerebral cortex (via the thalamic nuclei). The DCN are classically subdivided into four different nuclei (Fig. 1a): the medial (MN), anterior interposed (AIN), posterior interposed (PIN), and lateral nucleus. In primates, the latter is also termed the dentate (LN/dentate). The DCN nuclei are distinguished on the basis of both their connections (Glickstein et al. 2011) and their phylogenetic development. During evolution, the DCN exhibited a remarkable change of size and form in different highly encephalized mammals. The LN/dentate increased considerably in size

in primates, whereas in cetaceans the more medial PIN showed the greatest increase (Voogd and Glickstein 1998). Furthermore, the shape of the enlarged primate LN/dentate changed in a remarkable fashion to a highly folded structure, while the cetaceans' PIN remained a globus-shaped nucleus. To comprehend the important and remarkable evolution of this major hub, we decided to quantify its major wiring components in rodents and primates.

Materials and methods

The study supplements our previous analysis (Hamodeh et al. 2014) and now includes the data of five adult (8–14 years) male monkeys (*Macaca mulatta*) weighing 8–12 kg. Handling and care of the animals was approved by the regional authorities (Regierungspraesidium) and complied fully with the guidelines of the European Community (EUV 86/609/EEC). All experiments were carried out in accordance with the institutional, national, and NIH guidelines on the use of animals in research. Following the induction of deep anesthesia (with ketamine/xylazine in rats and with barbiturates in monkeys), animals were perfused through the ascending aorta with 4% paraformaldehyde prepared in 0.1 M phosphate buffer (PB), pH = 7.4.

Histological processing was carried out as described previously (Hamodeh et al. 2014). In brief, tissue was mounted and sectioned to serial transversal slices of either 60 μm for the rats and, in the case of the monkey brains, 40 or 50 μm for immunohistochemistry and 60 μm for cell counting. For section orientation in the monkey see next chapter. The slices were then incubated in either the mouse monoclonal anti-microtubule-associated protein 2a, b (MAP2; Sigma-Aldrich, Steinheim, Germany, clone AP-20, Catalog No. 1406) or in the mouse monoclonal PCP-2 (F-3) (Cat. No. sc-137,064, Santa Cruz Biotechnology, Santa Cruz, CA). Primary antibodies were diluted at either 1:1000 (MAP2) or 1:100 (PCP2). The antibodies were visualized with the secondary antibody Alexafluor 488 goat anti-mouse (Invitrogen, Karlsruhe, Germany) at a concentration of 1:400.

Probe acquisition and 3D reconstruction of MAP2-labeled dendrites PCP2-labeled axons

Images were acquired with a laser scanning confocal microscope (LSM 510, Carl Zeiss, Jena, Germany) using the Argon laser (wavelength 488 nm) as described elsewhere (Hamodeh et al. 2010, 2014). Image stacks were taken for each probe using a pinhole diameter equal to 1 Airy unit. Stack matrix size and other details are listed in “Supplementary material Table 1”. Probe scans were deconvoluted using AutoQuant X3 iterative “blind deconvolution” with

maximum likelihood estimation and constrained iteration (Media Cybernetics, Bethesda, MD).

Probes were taken from each of the DCN in a systematic random fashion. In rats, slices were taken from every 4th section of the series. This resulted in a final spacing of 240 μm . Probes were sampled at xy intervals of 350 μm within a section. In monkey D98, we took every 8th horizontal cerebellar section (final slice spacing of 320 μm) and probes were sampled at an xy interval of 800 μm . We took sagittal sections covering the mediolateral middle parts of the LN/dentate from the other two monkeys. We obtained a total of 1041 probes: 323 (MAP2, 3 rats), 361 (MAP2, 3 monkeys), 113 (PCP2, 1 rat) and 244 (PCP2, 1 monkey).

We then used the Cavalieri estimator to calculate the volume of the DCN (VDCN) with $VDCN = \sum P_i \times aF \times T \times 1/ssf$, with P_i being points per section, aF area per point, T block advance and ssf the slice sampling fraction.

Fibers were quantified by custom-written scripts (Tcl) and the Amira software package (Amira 4.1.1, Mercury Computer Systems, Chelmsford, USA). Prior to the application of our segmentation and reconstruction algorithm, preprocessing included 3D Edge-preserving-smoothing using a time-stop of 50 (in PCP2 case of 100) and step size of 5 followed by Gaussian filtering using a $5 \times 5 \times 5$ kernel and $\sigma = 1$. Segmentation of the 8-bit gray-level images into a binary image was performed by testing different threshold values and then choosing a threshold of 25 for the MAP2 rat data, 40 for the MAP2 monkey data and 80 for the PCP2 case (0 black and 255 white). Threshold values were chosen such that nearby dendrites were prevented from merging. This meant that some very thin fibers became subthreshold and were, therefore, not taken into account by our algorithm. We quantified the occurrence of these subthreshold fibers in a random subselection of the probes. We examined 58 of the rat (18%) and 60 of the monkey dendritic probes (17%). Our selection algorithm ensured that equal numbers of probes were chosen from the different DCN. The results are summarized in Supplementary Table 2. In some instances, our reconstruction algorithm failed to recover small chunks of dendrites (Fig. 1b, arrow heads). However, this occurred rarely (at a magnitude less frequent than the subthreshold fibers) and, therefore, was not taken into account further.

The final 3D reconstruction steps included chamfer distance map calculation, thinning process and, finally, conversion to a skeleton structure as described previously (Hamodeh et al. 2010). Furthermore, we manually removed all MAP2-stained somata from the images. In the monkey probes, we also removed the lipofuscin particles. The final skeleton structure consisted of dendritic and PC axonal segments with cylinder nodes spaced at

intervals of 0.5 μm along the fibers. The fiber radius is calculated at each node between the center of the node and the boundary, as obtained by the chamfer map calculation (Hamodeh et al. 2010). The reconstructed fibers were further thresholded to exclude very small particles ($<0.25 \mu\text{m}$) due to spurious labeled voxels.

Quantitative data analysis

The following parameters were extracted from our fiber segmentation and reconstruction analysis (Hamodeh et al. 2010, 2014): dendritic and PCax diameter (D_{dia}) and dendritic and PCax length density (DI_{dens}). The average dendritic length per neuron (DI_{neu}) was obtained by normalizing the dendritic length density by the neuron count density. We used custom-written scripts in Matlab (8.3, The MathWorks Inc., Natick, MA, 2000) to integrate the individual probes into data structures. These included the Zeiss LSM information, probes location, DCN classification, segmented fiber parameters and probe volume. We also systematically evaluated the tissue penetration of the antibody within each probe by calculating the fluorescence intensity in relation to the depth of the section. From this evaluation, and as described in detail previously (Hamodeh et al. 2010, 2014), we limited the region of fiber analysis to the stack of optical sections whose maximal intensity was 95.4% of that ascertained within the total probe. We also accounted for slice shrinkage by checking slice thickness after staining and embedding. The densities used for our analysis were obtained by multiplying each of the probes Th_{ref} with the fraction of microtome tissue block advancement and the total tissue thickness obtained after staining and embedding. Tissue thickness was measured on the Zeiss LSM 510 microscope equipped with a z -axis motorized stage. The regions within the DCN showed considerable shrinkage in the thickness of the section to 36% (60- μm block advancement, 22 μm after mounting), thus confirming earlier results in which we had obtained a shrinkage to 27% of the original thickness (Sultan et al. 2003).

Neuron and glia counts

Serial Nissl slices from four rats and two monkeys (T00 and B99) were used for counting neurons in the DCN. Purkinje cells in the cerebellar cortex were also counted for T00. Cells were counted using the optical fractionator (MicroBrightField Inc., Williston, VT, USA) as described previously (Hamodeh et al. 2014). On account of their small and homogeneously dark nuclei lacking surrounding cytoplasm, the glia cells could be readily distinguished from neurons, the latter having lightly stained nuclei with a nucleolus and surrounding cytoplasm with Nissl bodies. In the case of the rat DCN, we used a counting frame of $50 \times 50 \mu\text{m}$

with spacing of $200 \times 200 \mu\text{m}$ and counted every 4th slice. In the monkey DCN, we used a spacing of $400 \times 400 \mu\text{m}$ and took every 8th slice into account. Dissector height was set at 14 μm for the rats and 25 μm for the monkey with a 2- μm guard zones. This counting procedure yielded a coefficient of error (CE) of below 0.05 for both species. Section thickness was measured in each probe and found to be on average 23.4 μm (std=2.7 μm) in the rats and 29.6 μm (std=0.7 μm) in the monkeys. Neuron numbers were obtained by calculating $N = \Sigma Q \times 1/\text{ssf} \times 1/\text{asf} \times 1/\text{hsf}$, where ΣQ is the total counted neuron number, ssf the slice sampling fraction, asf the ratio between frame area and the area of the sampling grid, and hsf the height sampling fraction (ratio of dissector height and section thickness). Additional DCN and Purkinje cell counts for other mammals were obtained from earlier studies (Andersen et al. 1992; Korbo et al. 1993; Mwamengele et al. 1993; Sultan et al. 2002; Schüz and Sultan 2009).

Estimating dendritic region-of-influence

The dendritic region of influence (dROI) was estimated for the rat and the monkey LN/dentate from two sources. For the rat, we compared the dROI from a previous 3D dendritic reconstruction (Sultan et al. 2003) based on neurons filled intracellularly with neurobiotin with calibrated drawings of Golgi-stained neurons (Chan-Palay 1977). The dROIs in the 3D reconstructions were calculated with Matlab's built-in function `convhull`. We compared these 3D estimates with 2D estimates of the same neurons, but now based on measuring the area of the polygon that connects the outer tips of the dendritic tree from 2D plots (from Fig. 5 in Sultan et al. 2003). This comparison of the 3D and 2D data yielded similar results (232 ± 73 vs. $224 \pm 75 \mu\text{m}$, respectively) and a t test showed no statistical difference ($t = -0.48$; $df = 24$; $p = 0.63$). We, therefore, obtained further estimates from calibrated drawings of Golgi-stained neurons (Chan-Palay 1977) for the rat and the monkey by measuring the area of the polygon that connects the outer tips of the dendritic tree. Supplementary material Fig. 1 shows examples of such polygon from the two sources. Finally, we obtained the dROI diameters from the polygon measurement by taking a circle diameter occupying the area ($\text{dROI diam} = 2 \cdot (\text{polygon area}/\text{Pi})^{0.5}$).

Statistical analysis

Statistical analysis was performed within Matlab with custom-made scripts and built-in routines. Univariate data were plotted using the `boxplot` function, with five horizontal lines indicating the 10th, 25th, 50th, 75th, and 90th percentiles. The notches display the 95% confidence intervals for the median. Statistical significance within the group

was tested with two-way ANOVAs (for difference within species and DCN classification). Estimates of the dendritic length per neuron were obtained as ratios of two measured parameters and were checked for significant differences by comparing their confidence intervals (Donner and Zou 2012). In a similar fashion, confidence intervals (CI) comparing the difference between fiber distributions were calculated as confidence level = $\mu_{i_1} - \mu_{i_2} \pm t_{1-\alpha/2, n_{i_1} + n_{i_2} - 2} * (2 * MSE_i / n_{i_1})^{0.5}$, with μ_{i_1} and μ_{i_2} , the means at the i_{th} b_{in} , n_{i_1} , n_{i_2} the sample size at the i_{th} b_{in} , n_{i_1} , n_{i_2} the joint sample size calculated as $2 / (1/n_{i_1} + 1/n_{i_2})$ and MSE_i the estimated standard error calculated as $(sd_{i_1}^2 + sd_{i_2}^2) / 2$. Other statistical differences were tested with the Student t tests. Linear fits were performed using the Matlab `robustfit` routine.

Results

Regular scaling of neuron density and wiring in the DCN

We analyzed the Purkinje cell axons (PCax) and the dendrites of the DCN neurons, comparing the rat and rhesus monkey DCN in a systematic and quantitative fashion. We used fiber reconstruction and tracking algorithms (Fouard et al. 2006; Hamodeh et al. 2010, 2014) on immunofluorescent stained material (Fig. 1a, b), which then enabled us to semi-automatically extract wiring information on fiber length density and fiber diameters. We began by comparing the fiber density estimates with neuron density estimates in the different DCN. Our results show that the classification of the DCN does little to explain the neuron density variability in our samples. By contrast, and as anticipated, the species classification has a major effect on explaining the variability (two-factorial ANOVA with F values 0.25 vs. 23.4 with $p < 0.0001$ vs. $p = 0.86$ for the factors DCN class vs. species origin). The lower neuron density in the rhesus monkey corresponds to a regular down-scaling of neuron number in larger brained animals (Fig. 1c, d) and is comparable to the scaling observed in Purkinje cell numbers. Our data for the DCN, therefore, lie within the range of the theoretically expected scaling of neuron number depending on tissue volume raised to the power of $-1/3$ (Braitenberg 2001).

We detected a larger influence of the DCN classification on the variability of the dendritic and axonal wiring than on the variability of neuron densities (Fig. 1e). A two-factorial ANOVA showed a major influence of DCN classification on the dendritic length density variability (two-factorial ANOVA with F values 14.5 vs. 19.9, $df = 1$ vs. $df = 4$ and $p < 10^{-5}$ vs. $p < 10^{-11}$ for the factors DCN class vs. species origin). A similar major influence of DCN classification was also observed in the variability of the PCax (Fig. 1f),

where a two-factorial ANOVA yielded f values 57.6 vs. 5.1 and $p = 10^{-37}$ vs. $p \leq 0.024$ for the factors DCN class vs. species origin. One major influence in accounting for the variability in the DCN wiring is the higher number of dendrites and PCax length density in the PIN and the LN, the phylogenetically newer DCN (Hamodeh et al. 2014). In general, the DCN have a lower fiber length density than for instance the cerebral cortex. This has been described previously (see Hamodeh et al. 2014).

Normalizing dendritic density by cell number: hypometric dentate dendritic trees

In a next step, we examined the dendritic length density normalized by the neuron densities, yielding the average amount of dendritic length per neuron (Fig. 1g). As already reported previously (Hamodeh et al. 2014), by comparing our population-based approach with results obtained from intracellularly stained neurons of the rat LN/dentate (Sultan et al. 2003), we obtained good agreement for the amount of dendrite per neuron (2.83 compared with 2.65 mm). As anticipated, we obtained a larger amount of dendrites per neuron (rat: 2.1 vs. monkey: 4.8 mm) in the rhesus monkey DCN. We compared the two species by scaling the rodent data by a factor derived from the individual DCN volumes to the power of $1/3$. In the case of MN and PIN, the predictions are well within the confidence intervals obtained for the primate estimate. However, in the case of the primate LN/dentate, the prediction for a nucleus of its size should be in the region of 10 mm of dendritic length per neuron. We obtained a length of only 4.8 mm; about 50% less than anticipated.

To validate our findings, we compared them to a different estimate of dendritic tree size by examining the region-of-influence (dROI) defined as the polygon drawn by connecting the distant dendritic distal tips. We compared the data obtained in a previous study by intracellularly filling LN/dentate neurons in rats (Sultan et al. 2003) with Golgi-stained neurons of rats and rhesus monkeys (Chan-Palay 1977). The comparison of the differently stained rat LN/dentate neurons yielded a similar dROI diameter. The prediction for the monkey based on the LN/dentate tissue volume scaling yielded a diameter of $\sim 850 \mu\text{m}$. Our measurement, however, was much smaller than expected ($190 \mu\text{m}$). This is in agreement with the dendritic length per neuron result of our population-based analysis, which was also smaller than expected, and indicates that the majority of neurons in the primate LN/dentate must exhibit a hypocaling with dwarf-like clustered dendrites (Fig. 1h, figure inlets).

We went on to estimate the potential bias in our reconstruction algorithm caused by the very thin fibers being subthreshold (see Supplementary Table 2). An ANOVA

showed no significant effect on the amount excluded due to DCN or species classification. Therefore, our finding of hyposcaling dendrites in the primate LN/dentate is not explained by this effect.

We also compared the PCax length density to the number of Purkinje cells in the rat and rhesus monkey. By normalizing the total PCax length of the DCN (see Supplementary data: estimating PCax length in rats and rhesus monkey), we obtained 7.1-mm PCax length per Purkinje cell for the rats as opposed to 25.1 mm for the rhesus monkey. This is comparable to the rhesus monkey prediction of 27.9 mm based on the factor derived from DCN volumes to the power of 1/3.

Scaling of dendritic and axonal diameters

Our fiber tracking and reconstruction algorithm also estimated the diameter of the stained dendrites and PCax. As predicted, we found larger diameter estimates for both fibers in the monkey (Fig. 2a, b). An ANOVA analysis shows that the dendritic diameter variability was largely due to differences in species ($F=498$; $p<0.0001$) and, to a smaller degree, to the nuclear origin ($F=17.5$; $p<0.0001$). In the PCax diameters, we also found a larger influence of species ($F=201.9$, $p<0.0001$) versus nucleus ($F=8.5$; $p<0.0001$).

A comparison of the fiber diameter histograms (Fig. 2c, d) shows that the increase in size differs between the dendrites and axons: within the dendrite, there appears to be a general shift to higher diameters in primates. By contrast, the diameter range in axons broadens to include larger diameter axons in primates. For further analyses, we first examined how the diameters were distributed in the two species by subtracting them bin by bin for each DCN (Fig. 2e, f). We confirm that the primate dendritic diameters in the LN/dentate differ from the other distributions around the diameters 0.4 μm , based on the fact that they do not overlap with the 99% confidence intervals (CI) of the other distributions. We then compared a primate and an upscaled rat diameter distribution. Fig. 2g, h shows the sum of the rectified differences between the distributions (upscaled rat vs. primate) for different scaling factors. Although the two figures show certain similarities (steep descent to factor 1 and gradual rise for values larger than 1.5), the difference becomes evident in Fig. 2i, j. Here, we plotted the optimal scaling factor (yielding the smallest difference between primate and upscaled rat). With regard to the dendrites, a scaling factor of 1.35 yielded a near-perfect match between the upscaled rat and the primate. As for the axons, a broad range of scaling (1–1.5) yielded similar results, with a non-optimal fit between primates and upscaled rat pointing to a more complex scaling in axons. Such complexity was to be expected since the PCax contains both the myelinated and

the unmyelinated axon portions within the DCN. A similar distribution pattern can be observed for cortical axons (Wang et al. 2008; Buzsaki and Mizuseki 2014).

On the basis of our observation of hypometric scaling of the dendritic length in the primate LN/dentate, we would have expected a specific change in the dendritic diameter distribution in this nucleus. In a detailed examination of the different DCN histograms, we observed that, unlike in the axons, there was a deviation in the dendritic LN/dentate distribution (Fig. 2e), with a high proportion of small diameters (around 0.4 μm), and a lower proportion of large diameters (around 2 μm) in the monkey samples. Such a difference would arise if an isodendritic branching pattern changes to an idiodendritic pattern (Sultan et al. 2001), the former having more primary dendrites and the latter more distal bifurcations (yielding more thin dendrites). An earlier quantitative analysis conducted on the rodent LN/dentate neurons revealed a heterogeneous population due to the presence of two such extreme branching patterns (Sultan et al. 2001).

In contrast to our findings in the dendrites, the different DCN histograms of the PCax did not show such differences between the different DCN for the respective species. This also supports our interpretation that differences in the monkey dendritic distributions are not due to biases introduced by our reconstruction algorithm.

We also derived a parameter to better capture the differences in the dendritic diameter histograms. We took the ratio of the small dendritic diameter counts (at 0.41 μm) of the rhesus monkey and divided these by the counts at larger diameters (at 2 μm). In the rats, these corresponded to the diameters 0.35 and 1.35 μm , respectively (Fig. 2e). In Fig. 3a, b, we plotted this ratio against the dendritic density to test whether higher dendritic densities lead to thinner dendrites and higher ratios. We found no significant correlation between the two parameters. Furthermore, we found a similar pattern for most of the DCN in the two species with the exception of the LN/dentate. We used a two-way ANOVA to test the variance explained by species and DCN classification and discovered that the two factors (F -stat 6.79, $DF=1$, $p<0.01$ and F -stat: 8.68, $DF=4$, $p<0.0001$ for species and DCN classification, respectively) had a statistically significant influence. We also performed a post hoc test and ascertained that the primate LN/dentate had a significantly higher diameter ratio than all the other subnuclei (post hoc HSD test: LN to AIN: $p<0.01$; LN to NM: $p<0.0001$; LN/dentate to PIN: $p<0.0005$). Furthermore, we plotted the diameter ratio on a 3D-surface rendering of the primate DCN (Fig. 3c) and found that the higher dendritic diameter ratios within the LN/dentate tended to be located in the dorsal region.

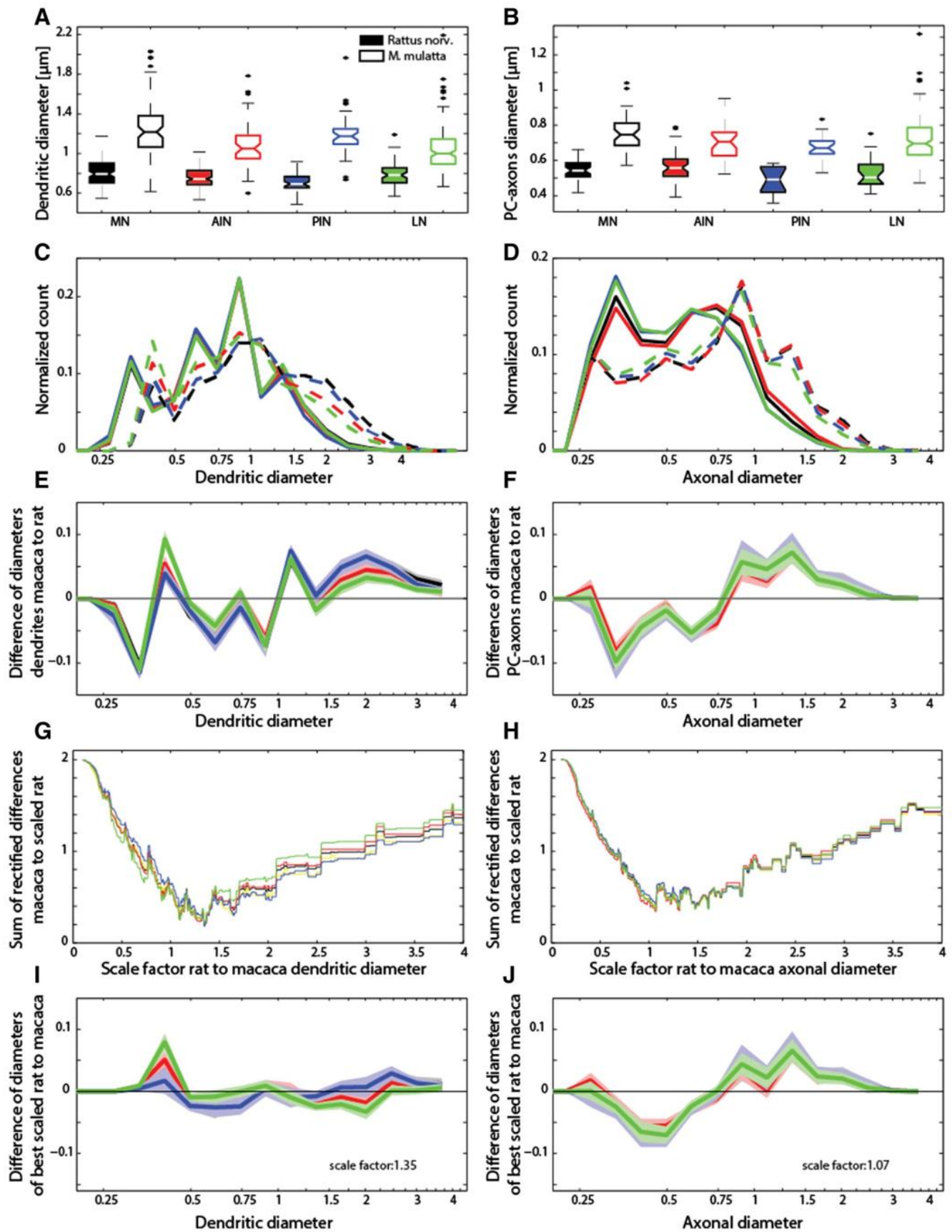


Fig. 2 Fiber diameter in different DCN subnuclei compared to predictions. **a** Monkey DCN dendrites exhibited larger diameters than rats. The thickest dendrites were measured within the monkey MN. The largest difference was observed within the PIN (factor of 1.7 between monkey and rats), with 1.19 μm ($\text{sd}=0.22$) in monkeys compared to 0.7 μm in rats ($\text{sd}=0.08$). The second largest difference was observed in the MN, ($\times 1.5$), with 1.25 μm ($\text{sd}=0.3$) in monkeys compared to 0.81 μm in rats ($\text{sd}=0.14$). The LN/dentate showed the smallest difference (1.3), with 1 μm ($\text{sd}=0.23$) in monkeys compared to 0.79 μm in rats ($\text{sd}=0.12$). Statistical analysis with a two way-factorial ANOVA showed that both the influence of the species ($F=511$; $p<0.0001$), and the origin of the probes from the different subnuclei ($F=8.76$; $p<0.0001$) were highly significant. **b** As in the dendritic diameters, differences were also observed in the PC axons between the two species. Again, the MN showed the largest increase from 0.54 to 0.75 μm . The differences were statistically significant (two-way ANOVA yielded $F=201.9$, $p<10^{-36}$ for species vs. $F=8.5$; $p<10^{-6}$ nucleus). **c, d** Histograms showing diameter distribution for the dendrites (**c**) and PCax (**d**) for different nuclei (*color coded*) and for the rats (*continuous line*) and monkey (*dashed line*). The dendritic diameters (*C*) of the monkey are shifted to larger diameters. Within the rats, the different DCN are indistinguishable from each other. By contrast, larger differences between the DCN are found in the monkey: the LN/dentate has more of the smaller diameter dendrites ($\sim 0.4 \mu\text{m}$) and fewer thick dendrites ($>1.5 \mu\text{m}$). A similar, but smaller pattern is observed in the AIN. Histograms were normalized by the sum of all diameter counts for the respective species and subnucleus. Fiber diameters are plotted as natural logarithms. **e** Difference calculation between the rhesus monkey and rat dendritic histograms (**c**) for each DCN. The difference calculation is plotted together with the 99% CI (*lighter shaded color*). The curves overlie each other and are within their CI up to a diameter of 0.4 μm , at which point the monkey dendritic histogram for the LN/dentate exceeds the others. **f** Difference calculation between the rhesus monkey and rat PCax histograms (**d**) for each DCN. As in **e**, the difference calculation is plotted together with the 99% CI. **g, h** Sum of the rectified difference curves obtained for different scaling factors. The rat fiber diameters were multiplied with varying scaling factors (scaling factors plotted on the *abscissa*) and then subtracted from the primate data. The difference was rectified and summed and plotted on the ordinate axis (**g** dendrites and **h** PCax). **i, j** Results for best scaling factors (**i** dendrites and **j** PCax). In the case of the dendrites, a scale factor of 1.35 yielded optimal scaling. A wide range of values (1–1.5) yielded similar results in the case of the PCax, i.e., with little difference between the DCN. The optimal dendritic scaling factor, however, also showed an excess of thin dendrites mainly for the monkey LN/dentate and the number of dendritic diameters around 2 μm was lower than predicted. *Color code* for DCN: MN: *black*; PIN: *blue*; AIN: *red*; NL/dentate: *green*

Discussion

In summary, we observed a specific deviation from regular scaling in the dendrites of the LN/dentate of the primate brain. We observed a deviation from scaling in the dendritic length per neuron, together with a smaller than predicted dendritic region-of-influence in the LN/dentate neurons. These deviations in scaling support the notion that the primate brain has a special architecture and represents a distinct cerebrotype (Haug 1970; Clark et al. 2001; Watson et al. 2012). The presence of neurons with restricted and clustered branching trees explains our findings of special dendritic scaling. These neurons were first described

qualitatively by Chan-Palay (1977) with Golgi staining and later quantitatively with intracellular staining techniques (Sultan et al. 2003). The increased presence of such neurons is also supported by our observation of specific changes in the dendritic diameter distribution. Such dendritic adaptations could, in principle, be either due to adaptations in the connectivity of the network or to a change in the computational role of the neurons. It has already been proposed that clustered/idi dendritic branching (Ramon-Moliner and Nauta 1966) allows for more interaction between the synaptic inputs simply because the synapses are closer together (Koch et al. 1983). This closer interaction could, then, be more effective in eliciting the well-known rebound bursts of DCN neurons following Purkinje cell inhibitory inputs (Llinas and Muhlethaler 1988; Aizenman and Linden 1999). However, such a rebound burst is also present in the other DCN neurons (Aizenman and Linden 1999) and is, therefore, in no way unique to the LN/dentate. This agrees with the general view that the computational operations within the cerebellum are the same in the different cerebellar subregions (De Zeeuw et al. 2011). The change in network connectivity, therefore, continues to be the principal explanation of the observed dendritic changes.

A further consequence of the smaller dROIs of the primate LN/dentate would be that more independent modules could be packed within the LN/dentate. Our results predict that the smaller dROIs (by a linear factor of about ~ 4.5 smaller than expected) allow for 90x more modules to be placed within the LN/dentate volume. We could expect an even larger increase for the ape and human dentate, with an even more flattened LN/dentate sheet (Sultan et al. 2010). The advantage of such an increase in the number of computational modules is, however, not yet clear. Different views on the role of the expanded primate cerebellum and LN/dentate range from sensorimotor elaboration of finger use or eye–hand coordination (Bower 1997; Glickstein et al. 2005) to non-motor cognitive contributions (Middleton and Strick 1997; Stoodley and Schmahmann 2009). On the basis of these two views, it could be predicted that more cerebellar modules are required for the finer scaled and more versatile finger movement, or for more combinations of hand and eye modules. Alternatively, more non-motor cognitive modules are required for the vast multitude of human behavior. Either way, our findings provide an additional handle to tackle the long-debated role of the human LN/dentate and could enable us to directly relate crucial evolutionary adaptations to the unique morphology of the primate LN/dentate.

Another important implication of our observations concerns the well-established parasagittal organization of the cerebellum (Glickstein et al. 2011), which is probably related to different internal models (Wolpert et al. 1998). An increase in the number of modules might imply an

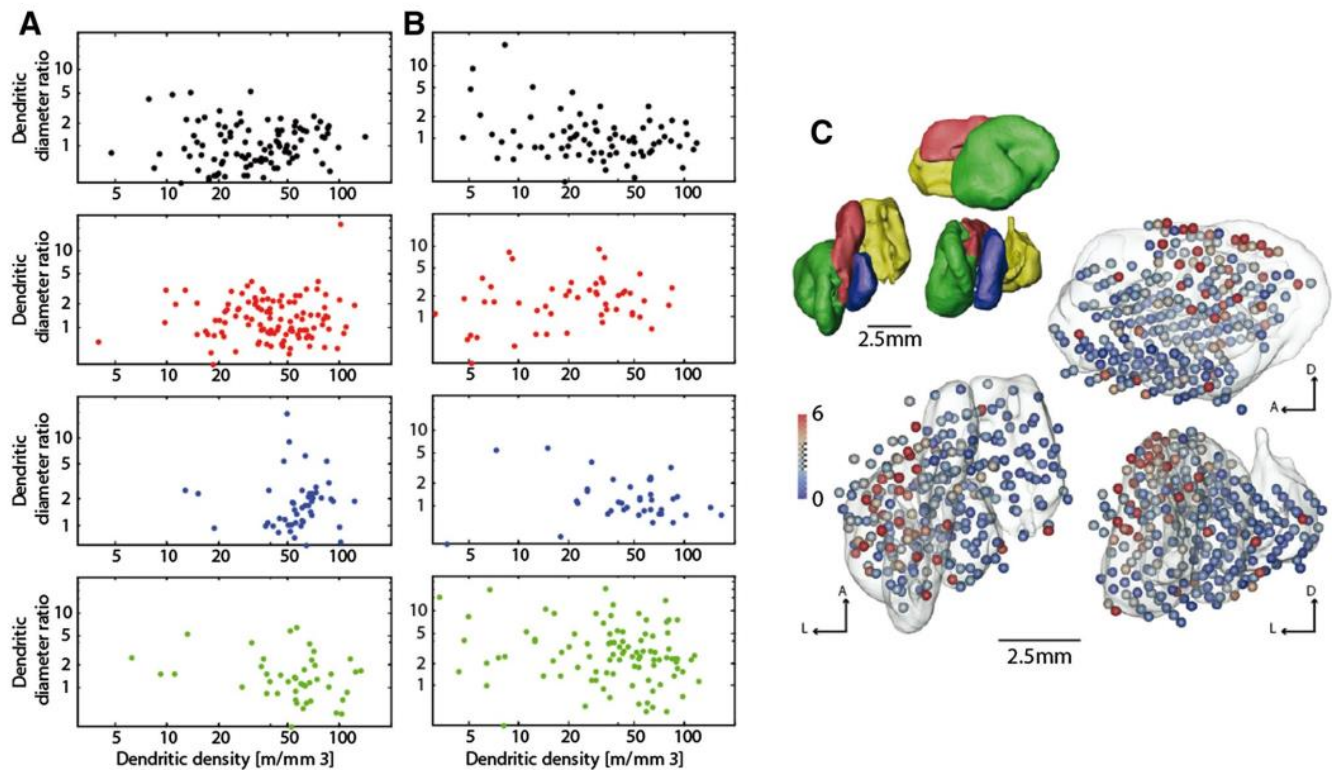


Fig. 3 Dendritic diameter ratio. **a, b** Double logarithmic plot of dendritic diameter ratio vs. dendritic length density for the rat (**a**) and the rhesus monkey (**b**). The four vertical subplots are the data for the MN (*black*), AIN (*red*), PIN (*blue*) and the LN/dentate (*green*). The diameter ratio was taken between thin diameters (rat: 0.35; monkey: 0.41 μm) and the thick diameters (rat: 1.35; monkey: 2 μm). The PIN and LN generally showed higher dendritic length densities on average. In the primate LN/dentate, a larger number of probes showed a higher dendritic diameter ratios than in the rat (**b**, lower panel). An ANOVA test showed significant effect of species and DCN classification for the dendritic diameter ratio (F -stat 6.79, $DF=1$, $p < 0.01$ and F -stat: 8.68, $DF=4$, $p < 0.0001$ for species and DCN classification, respectively). A post hoc test ascertained that the primate LN/dentate had a significantly higher diameter ratio than the other

nuclei (post hoc hsd test comparing monkey LN to AIN: $p < 0.01$; LN to NM: $p < 0.0001$; LN/dentate to PIN: $p < 0.0005$). **c** Surface models of the rhesus monkey DCN and the dendritic diameter ratio. The upper left models are surface renditions with the different subnuclei color coded: MN (*yellow*), AIN (*red*), PIN (*blue*) and the LN/dentate (*green*). The left shows the view from dorsal, the upper right from lateral, and the lower right from posterior. The same views are shown again in the larger 3D model version with transparent DCN surfaces. In addition, we plotted the distal-proximal dendritic diameter ratio as the proportion of 0.41- μm diameters divided by the proportion of 2- μm diameters color coded on small spheres, with *red* for larger ratios (more small diameters) and *blue* colors for lower ratios (larger thicker diameters)

increase in the number of parasagittal strips in the hemisphere connected to the LN/dentate, which would confirm a recent prediction (Jörntell 2017). In principle, one could expect the increase in the number of modules to occur along one of the two main cerebellar axes: the medio-lateral or the antero-posterior cerebellar axis. However, the larger surface increase of the dentate in the mediolateral axis (Sultan et al. 2010) would provide more space to accommodate independent modules, which would, in turn, support the theory of increased parasagittal strips.

Our approach is based on the analysis of the overall neuronal population of the DCN and, as such, does not allow us to draw conclusions about the different neuron class composition within the DCN. However, we were able to utilize this approach to extend our analysis beyond the

rodent species to that of primates, in which it is challenging to acquire sufficient information about individual neurons. In addition, the unbiased approach used in our study can be difficult to achieve with Golgi staining or intracellular staining (Hamodeh et al. 2014). Our population approach nevertheless enabled us to detect changes in the dendritic bifurcation pattern of DCN neurons.

In summary, our analysis of the major hubs connecting the cerebellar with the cerebral cortex verifies that these hubs can show changes from a predictable scaling (neuron density decrease and dendritic/axonal length increase) to a different scaling mode, with smaller dendritic ROIs allowing for a larger number of modules in the most enlarged DCN of primates, in the LN/dentate. This surprising result is well in keeping with the long-known observation of the unique anatomy of the primate LN/dentate from which its

name is derived: the flattening and folding of its gray matter into a tooth-shaped structure (Voogd 2003; Tellmann et al. 2015). It has already been suggested that the LN/dentate dendritic adaptations lead to reduced mechanical tension with the DCN, thus allowing it to flatten (Sultan et al. 2003), as was already proposed for the cerebral cortex (Van Essen 1997). Mapping the dendritic diameter ratio associated with this dendritic adaptation to the dorsal LN/dentate also agrees well with this proposal, since this so-called microgyric (dorsal) region (Voogd 2003) (Tellmann et al. 2015) shows marked flattening in the macaque (Sultan et al. 2010). Our result of the preponderance of clustered dendrites trees in the primate LN/dentate not only confirms Chan-Palay's earlier description of these neurons (Chan-Palay 1977) but is also the first to relate their special branching pattern to the unique morphology of the primate LN/dentate.

Acknowledgements This study was supported by the Hertie foundation and the Tübingen University. Additional support was obtained from the German Research Foundation (DFG SU171.3-1 grant), China Scholarship Council to HM and by Umeå University to FS. We are grateful to Ute Großhennig for assistance with the histology.

Author contributions SH and HM conducted the histology and, together with FS, analyzed the data. AB counted the cells. FS wrote the manuscript, designed the project, and was responsible for securing funding.

Compliance with ethical standards

Conflict of interest The authors declare that there are no conflicts of interest.

Open Access This article is distributed under the terms of the Creative Commons Attribution 4.0 International License (<http://creativecommons.org/licenses/by/4.0/>), which permits unrestricted use, distribution, and reproduction in any medium, provided you give appropriate credit to the original author(s) and the source, provide a link to the Creative Commons license, and indicate if changes were made.

References

- Abeles M (1991) *Corticonics: neural circuits of the cerebral cortex*. Cambridge University Press, Cambridge
- Aizenman CD, Linden DJ (1999) Regulation of the rebound depolarization and spontaneous firing patterns of deep nuclear neurons in slices of rat cerebellum. *J Neurophysiol* 82:1697–1709
- Andersen BB, Korbo L, Pakkenberg B (1992) A quantitative study of the human cerebellum with unbiased stereological techniques. *J Comp Neurol* 326:549–560
- Andersen BB, Gundersen HJ, Pakkenberg B (2003) Aging of the human cerebellum: a stereological study. *J Comp Neurol* 466:356–365
- Azevedo FA, Carvalho LR, Grinberg LT, Farfel JM, Ferretti RE, Leite RE, Jacob FW, Lent R, Herculano-Houzel S (2009) Equal numbers of neuronal and nonneuronal cells make the human brain an isometrically scaled-up primate brain. *J Comp Neurol* 513:532–541
- Bower JM (1997) Is the cerebellum sensory for motor's sake, or motor for sensory's sake: the view from the whiskers of a rat? *Prog Brain Res* 114:463–496
- Braitenberg V (2001) Brain size and number of neurons: an exercise in synthetic neuroanatomy. *J Comput Neurosci* 10:71–77
- Braitenberg V, Schüz A (1991) *Anatomy of the cortex*. Springer, Berlin
- Buzsaki G, Mizuseki K (2014) The log-dynamic brain: how skewed distributions affect network operations. *Nat Rev Neurosci* 15:264–278
- Chan-Palay V (1977) *Cerebellar dentate nucleus: organization, cytology and transmitters*. Springer, Berlin/Heidelberg/New York
- Chklovskii DB, Schikorski T, Stevens CF (2002) Wiring optimization in cortical circuits. *Neuron* 34:341–347
- Clark DA, Mitra PP, Wang SS (2001) Scalable architecture in mammalian brains. *Nature* 411:189–193
- De Zeeuw CI, Hoebeek FE, Bosman LWJ, Schonewille M, Witter L, Koekkoek SK (2011) Spatiotemporal firing patterns in the cerebellum. *Nat Rev Neurosci* 12:327–344
- Donner A, Zou G (2012) Closed-form confidence intervals for functions of the normal mean and standard deviation. *Stat Methods Med Res* 21:347–359
- Finlay BL, Darlington RB, Nicastro N (2001) Developmental structure in brain evolution. *Behav Brain Sci* 24:263–278
- Fouard C, Malandain G, Prohaska S, Westerhoff M (2006) Blockwise processing applied to brain microvascular network study. *IEEE Trans Med Imaging* 25:1319–1328
- Glickstein M, Waller J, Baizer JS, Brown B, Timmann D (2005) Cerebellum lesions and finger use. *Cerebellum* 4:189–197
- Glickstein M, Sultan F, Voogd J (2011) Functional localization in the cerebellum. *Cortex* 47:59–80
- Hamodeh S, Eicke D, Napper RMA, Harvey RJ, Sultan F (2010) Population based quantification of dendrites: evidence for the lack of microtubule-associate protein 2a,b in Purkinje cell spiny dendrites. *Neuroscience* 170:1004–1014
- Hamodeh S, Sugihara I, Baizer J, Sultan F (2014) Systematic analysis of neuronal wiring of the rodent deep cerebellar nuclei reveals differences reflecting adaptations at the neuronal circuit and internuclear level. *J Comp Neurol* 522:2481–2497
- Haug H (1970) Quantitative Data in Neuroanatomy. In: Schad JP, Smith J (eds) *Computer and brains*, vol. 16129. Elsevier, Amsterdam, pp 113–127
- Jörntell H (2017) Cerebellar physiology—links between microcircuitry properties and sensorimotor functions. *J Physiol* 595:11–27
- Koch C, Poggio T, Torre V (1983) Nonlinear interactions in a dendritic tree: localization, timing, and role in information processing. *Proc Natl Acad Sci USA* 80:2799–2802
- Korbo L, Andersen BB, Ladefoged O, Moller A (1993) Total numbers of various cell types in rat cerebellar cortex estimated using an unbiased stereological method. *Brain Res* 609:262–268
- Llinas R, Muhlethaler M (1988) Electrophysiology of guinea-pig cerebellar nuclear cells in the in vitro brain stem-cerebellar preparation. *J Physiol Lond* 404:241–258
- Middleton FA, Strick PL (1997) Cerebellar output channels. *Int Rev Neurobiol* 41:61–82
- Mwamengele GL, Mayhew TM, Dantzer V (1993) Purkinje cell complements in mammalian cerebella and the biases incurred by counting nucleoli. *J Anat* 183:155–160

- Ramon-Moliner E, Nauta WJ (1966) The isodendritic core of the brain stem. *J Comp Neurol* 126:311–335
- Schüz A, Sultan F (2009) Brain connectivity and brain size. In: Squire LR (ed) *New encyclopedia of neuroscience*, Vol 2. Academic Press, Oxford, pp 317–326
- Stoodley C, Schmahmann J (2009) Functional topography in the human cerebellum: a meta-analysis of neuroimaging studies. *Neuroimage* 44:489–501
- Sultan F, Czubayko U, Thier P (2001) Principal Component Analysis of the Rat Lateral Cerebellar Nuclear Neurons. vol. *Proceedings of the 28th Goettingen Neurobiology Conference*
- Sultan F, König T, Möck M, Thier P (2002) Quantitative organization of neurotransmitters in the deep cerebellar nuclei of the Lurcher mutant. *J Comp Neurol* 452:311–323
- Sultan F, Czubayko U, Thier P (2003) Morphological classification of the rat lateral cerebellar nuclear neurons by principal component analysis. *J Comp Neurol* 455:139–155
- Sultan F, Hamodeh S, Baizer JS (2010) The human dentate nucleus: a complex shape untangled. *Neuroscience* 167:965–968
- Tellmann S, Bludau S, Eickhoff S, Mohlberg H, Minnerop M, Amunts K (2015) Cytoarchitectonic mapping of the human brain cerebellar nuclei in stereotaxic space and delineation of their co-activation patterns. *Front Neuroanat* 9:54
- Van Essen DC (1997) A tension-based theory of morphogenesis and compact wiring in the central nervous system. *Nature* 385:313–318
- Voogd J (2003) The human cerebellum. *J Chem Neuroanat* 26:243–252
- Voogd J, Glickstein M (1998) The anatomy of the cerebellum. *Trends Neurosci* 21:370–375
- Wang SSH, Shultz JR, Burish MJ, Harrison KH, Hof PR, Towns LC, Wagers MW, Wyatt KD (2008) Functional Trade-offs in white matter axonal scaling. *J Neurosci* 28:4047–4056
- Watson C, Provis J, Herculano-Houzel S (2012) What determines motor neuron number? Slow scaling of facial motor neuron numbers with body mass in marsupials and primates. *Anat Rec* 295:1683–1691
- Wolpert DM, Miall RC, Kawato M (1998) Internal models in the cerebellum. *Trends Cogn Sci* 2:338–347
- Yopak KE, Lisney TJ, Darlington RB, Collin SP, Montgomery JC, Finlay BL (2010) A conserved pattern of brain scaling from sharks to primates. *Proc Natl Acad Sci USA* 107:12946–12951

Appendix 2:

Haian Mao, Salah Hamodeh, Fahad Sultan. (2018) Quantitative Comparison Of Vesicular Glutamate Transporters in rat Deep Cerebellar Nuclei. Neuroscience 376 152–161

Quantitative Comparison Of Vesicular Glutamate Transporters in rat Deep Cerebellar Nuclei

Haian Mao,^a Salah Hamodeh^a and Fahad Sultan^{a,b,*}

^a Department of Cognitive Neurology, HIH for Clinical Brain Research, Otfried-Müller-Str. 27, 72076 Tübingen, Germany

^b Department of Integrative Medical Biology, Umeå University, Linnéus väg 9, 901 87 Umeå, Sweden

Abstract—The excitatory synapses of the rat deep cerebellar nuclei (DCN) were quantitatively analyzed by vesicular glutamate transporter 1 and 2 (vGluT1 and vGluT2) immunolabeling. We calculated the number and sizes of the labeled boutons and compared them between lateral/dentate nucleus (LN/DN), posterior interposed nucleus (PIN), anterior interposed nucleus (AIN), and medial nucleus (MN). The density of vGluT1+ boutons differs significantly within these nuclei. In contrast, the vGluT2+ bouton density is more similar between different nuclei. The phylogenetically newer DCN (LN/DN and PIN) have a 39% higher density of vGluT1+ boutons than the phylogenetically older DCN (AIN and MN). The volume of vGluT1+ boutons does not differ between the DCN, however the average volume of vGluT2+ boutons is larger in MN. In summary, our current results confirm and extend our previous findings showing that the increase in dendritic and axonal wiring in phylogenetically newer DCN is associated with an increase in vGluT1+ bouton density. © 2018 IBRO. Published by Elsevier Ltd. All rights reserved.

Key words: vesicular glutamate transporter, quantitative analysis, bouton density, bouton size, deep cerebellar nuclei.

INTRODUCTION

The deep cerebellar nuclei (DCN) are the main output of the cerebellum and have been implicated to play an important role in motor skill learning (De Zeeuw and Ten Brinke 2015). In addition, the evolution and increase in size and shape complexity in primates of one part of these nuclei (the lateral nuclei and in humans termed the dentate nuclei, LN/DN) has led to continued interest and research (Sultan et al., 2010; Bostan et al., 2013; Tellmann et al., 2015; Hamodeh et al., 2017). In our previous work (Hamodeh et al., 2014), we showed that the neuronal wiring is heterogeneous in the four cerebellar nuclei of the rat. Compared to the phylogenetically older (MN and AIN), the newer DCN (PIN and LN/dentate) have a higher length density of dendrites and Purkinje cell axons. In this study, we asked whether the dendritic wiring increase is also accompanied by an increase in the excitatory synaptic density.

The DCN neurons receive the excitatory glutamatergic synapses from mossy and climbing fibers and inhibitory GABAergic synapses from Purkinje cells. The excitatory synapses are divided into two subsets according to different vesicular transporters (vGluT1 and

vGluT2) that are utilized within the presynaptic bouton to load glutamate into the vesicles. These transporters are largely colocalized with vesicles at the presynapse (Bellocchio et al., 1998; Takamori et al., 2000; Herzog et al., 2001; Varoqui et al., 2002). These two subgroups are generally expressed in a complementary pattern in the brain (Ni et al., 1994; Ni et al., 1995; Ni et al., 1996; Aihara et al., 2000; Fremeau et al., 2001; Herzog et al., 2001; Kaneko and Fujiyama 2002; Kaneko et al., 2002; Hartig et al., 2003; Hisano 2003, Fremeau et al., 2004a, b). The cerebellum is among the few brain regions that utilize both classes of transporters, with a small subset of presynapses co-expressing both transporters (Hioki et al., 2003). The climbing fibers from the inferior olive only use vGluT2, while mossy fibers from different precerebellar nuclei use vGluT1, vGluT2 or both (Hisano et al., 2002). vGluT3 is only transiently expressed in the cerebellum during early development (Boulland et al., 2004) and is absent in the adult pre-cerebellar nuclei and cerebellum (Gras et al., 2002; Hisano 2003; Costes et al., 2004; Herzog et al., 2004a).

Previous studies have not quantified the excitatory synapses within DCN. These excitatory afferents are from different precerebellar nuclei and terminate on the proximal and distal dendrites of the DCN neurons (Angaut and Sotelo 1973). The Purkinje cell GABAergic synapses terminate on the somata and proximal dendrites (De Zeeuw and Berrebi 1995). It has been reported that 62% in cat (Palkovits et al., 1977) and 73% in rat (De

*Correspondence to: F. Sultan, Dept. of Integrative Medical Biology, Umeå University, Linnéus väg 9, 901 87 Umeå, Sweden.

E-mail address: fahad.sultan@umu.se (F. Sultan).

Abbreviations: AIN, anterior interposed nucleus; DCN, deep cerebellar nuclei; LN/DN, dentate/lateral nucleus; MN, medial nucleus; PIN, posterior interposed nucleus; vGluT, vesicular glutamate transporter.

Zeeuw and Berrebi 1995) of the DCN synapses are Purkinje cell GABAergic synapses, leaving the rest 38% to 27% of the synapses belonging to be excitatory synapses. In this paper, we used vGluT1 and vGluT2 antibodies to label these excitatory synapses in the DCN and studied the four sub nuclei systematically. We compared the vGluT1- and vGluT2-labeled synaptic terminals and found significant differences in vGluT1+ bouton density within the DCN.

EXPERIMENTAL PROCEDURES

Tissue preparation

All animal experiments were carried out in accordance with the Society for Neuroscience and German Law (approved by the Regierungspräsidium Tübingen). Brains from three adult rats were used in this study (body weight 170–300 g and age 6–12 weeks). A mixture of ketamin (20 mg/100 g body weight) and xylazine (2mg/100 g body weight) was used to induce a deep anesthesia. The rats were perfused transcardially by 0.1 M PB and then by 4% ice-cold paraformaldehyde in 0.1 M phosphate buffer (PB) at pH 7.4. The brain was immediately dissected out of the skull and then cryoprotected in an ascending concentration of sucrose (10%, 20%, and 30% in 0.1 M PB). The cerebellum was cut off and mounted on a freezing microtome with the lateral side facing the platform. Sections of 40 μ m were serially cut and stored in 0.1 M PB. Immunofluorescence staining was carried out on free floating sections. Before primary antibody incubation, sections were washed in 0.1 M PB for 3 times, 5 min each and then blocked in 0.1 M PB with 10% horse serum (PAA Laboratories, Coelbe, Germany) and 0.3% Triton X-100 at room temperature for 1 h.

Immunofluorescence

The working concentration and incubation times were tested for each antibody in single stains. The optimized conditions were then used for the multiple stains. We performed a quadruple staining protocol for vGluT1, vGluT2, Purkinje Cell Protein 2 (PCP2), and KCNC3 (Kv3.3). Data of the Kv3.3 were used for a subsequent publication (Mao et al., in preparation). The sections were first incubated with goat vGluT1 (sc-13320, Santa Cruz Biotechnology, Texas) at 1:1000 at 4 °C for 16 h, followed by 3x washes in 0.1 M PB and then incubated with donkey anti goat Alexa Fluor 488 at 1:500 for 2 h at room temperature. The sections were then washed again before incubation with the combination of three antibodies of vGluT2 (1:1000, lot number: 135404, synaptic systems, North Saanich British Columbia), Kv3.3 (1:500, lot number: APC-102, Alomone labs, Israel) and PCP2 (1:200, lot number: sc-137064, Santa Cruz Biotechnology, Texas) at 4 °C for 16 h. The sections were then washed again and incubated with the combinations of the three secondary antibodies: goat anti guinea-pig Alexa Fluor 633 (1:500, A21105, Invitrogen, California), goat anti rabbit Cy3 (1:500, lot number: 81-6115, Invitrogen, California) and goat anti

mouse Alexa Fluor 405 (1:500, lot number: A31553, Invitrogen, California) for 2 h at room temperature. Sections were washed and mounted with Mowiol 4–88 (Merck, Darmstadt, Germany) in glycerol on glass slides. The slides were stored at 4 °C.

Image acquisition

Images were acquired with the confocal laser microscope (LSM 510, Carl Zeiss, Jena, Germany). We took overview images of vGluT1 staining for every section with 488-nm excitation and emission band pass filtering 505–550 nm at low magnification of 10 \times and probe locations were determined by first marking an identifiable origin (x, y coordinates: 0,0) and then determining the other probes location in the DCN region. These were taken at regular intervals of 250 μ m \times 250 μ m from two rats and at 200 μ m \times 200 μ m for the third rat. The location of the origin point was chosen from an easily identifiable structure (i.e., vessels) within a core region of the DCN, however, this location differs from slice to slice and is not related to the structures to be analyzed. For each probe, a z-stack was acquired under the 63 \times magnification, with a 2 \times zoom. The fluorophores were excited with 405 nm, Argon or HeNe lasers. We stained and analyzed 16 cerebellar sections (5–6 slices from each rat) and 189 probes were sampled in total (44 from the first rat, 55 from the second rat and 90 from the third rat). Details of antibodies, excitation wavelength and emission filters are listed in Table A.1 (see Appendices).

We also determined tissue shrinkage by taking four random positions within the DCN region for each slice and determining the upper and lower section borders by the staining signal for vGluT1 at a magnification of 20 \times dry objective. 64 probes were taken together in 3 rats (16 slices in total). The mean thickness of the slices after mounting was 26 μ m, while the original sectioning thickness was 40 μ m. This corresponds to a shrinkage to 65%, less than what we have observed (to 36%) in our previous studies (Hamodeh et al., 2014).

Classification of the rat DCN was based on the description in the previous paper (Hamodeh et al., 2014).

Data preprocessing

Data were acquired as 8-bit format and exported as such in Zeiss lsm format. Stacks were then deconvoluted using the iterative ($n = 10$) “blind deconvolution” of AutoQuant X3 (Media Cybernetics, Bethesda, MD) with the maximum likelihood estimation and constrained iteration. After deconvolution data were saved in Autoquant to 12-bit Zeiss tiff format. Data were imported and intensity range adjusted in Imaris (Bitplane AG, Switzerland) to unsigned 8-bit format.

The four antibodies showed slightly different tissue penetration abilities. Therefore, the deconvoluted image stacks were manually cropped in Imaris to eliminate the upper and lower slices that were not well stained. We performed a within voxel colocalization analysis in Imaris using Pearson’s coefficient (Costes et al., 2004) and with a threshold of 50/255 for all four channels.

The surfaces of vGluT1+ and vGluT2+ boutons were tracked in Imaris using different thresholding methods. For vGluT1 the Ridler and Calvard (R-C) algorithm (Ridler and Calvard 1978) was used. The R-C algorithm uses an iterative estimate to find the optimal threshold (Ridler and Calvard 1978). This was optimal for vGluT1 where background and foreground were well separated. We carefully checked the thresholding outcome and found that it recognized the weakly stained boutons located deeper in the section and rarely included background noise. For vGluT2, the R-C algorithm yielded on average a lower mean threshold (15.7 compared to 20.5 for vGluT1). This lower threshold was due to the presence of weaker stained vGluT2 DCN somata (lower intensity than the vGluT2+ boutons). Therefore, to exclude the somata we used a higher fixed threshold at 25/255. We checked the staining of structures which had a lower intensity than the somata by manually increasing the image intensity and found that only few of them have long and thin fibers attached and most of them cannot be distinguished from background noise. The surfaces were smoothed at 0.15 μ m and the diameter of largest sphere which fits into the objects was estimated at 0.5 μ m. The surfaces were further filtered by size by excluding surfaces with less than 10 voxels (Haass-Koffler et al., 2012).

The density of vGluT1+ and 2+ boutons were obtained by normalizing the surface number of each probe by the corrected volume of that probe. The probe volumes were corrected for shrinkage and for the Abercrombie error (Abercrombie 1946; Braitenberg and Schüz 1998). Thickness shrinkage was corrected by dividing the section thickness with the shrinkage factor (0.65). The Abercrombie correction was applied by adding the mean diameter of the surface/bouton to the section thickness (1.38 μ m for vGluT1 and 1.02 μ m for vGluT2). The volume of the probe was then calculated by multiplying the width, length and the corrected depth of that probe.

Statistical analysis

The 189 probe density values were assigned to one of the four DCN classes based on its location on the section (45 probes fell into MN, 60 into AIN, 38 into PIN, 46 into LN). Classification of the rat DCN was based on the description in the previous paper (Hamodeh et al., 2014). The mean bouton volume of each nucleus was obtained by averaging the mean surface volumes from the same nucleus category. Therefore for each probe we obtained the density value and mean surface volume for vGluT1 and 2. Values were power transformed to secure normal distribution in R (www.r-project.org) with Tukey's ladder of powers (transformTukey) approach and tested with Shapiro–Wilkes for normality. We also tested the power transformed data on variance equality with the Levene test. All data (vGluT1 and 2 density and volume) were normally distributed and had equal variance after power transformation.

We obtained multiple observations from each subject and therefore used linear mixed effects model analysis to account for dependencies within our data sets (Aarts et al., 2014). The large number of probes obtained per

animal was optimized to cover the variability present within the DCN based on our previous studies (Hamodeh et al., 2014; Hamodeh et al., 2017). We calculated the intra-cluster correlation (ICC) to evaluate the similarity within our probes. We also calculated eta-squared for the effect size by taking the ratio of within group variance and total variance. We applied linear mixed effects models with restricted maximum likelihood estimations as implemented in the lme4 package in R (www.r-project.org). We took the power transformed density or volume (for both vGluT1 and 2) as the models response. The DCN classification was modeled as a fixed effect while subject variance was modeled as a random effect in the model. We also constructed a null model with only the random effect. We compared the two models using likelihood ratio test to see whether these two models were significantly different from each other. If the p value was smaller than the significance level (0.05), it indicated that DCN classification affected the response significantly. Differences in means between nuclei were evaluated through multiple comparisons of means (Tukey contrasts). The confidence level α was set to 0.05 and adjusted for multiple comparisons with the Holm-Bonferroni correction.

We also obtained the individual volume, voxel intensities and shape parameters (sphericity, oblate and prolate ellipticity) of each surface (in total there were 67,643 vGluT1 and 51,393 vGluT2 surfaces) to search for outliers.

RESULTS

Antibody specificity test on rat cerebellar sections

To test for antibody specificity of the vGluT2 we combined the antibody and the antigen which was used for immunization and provided by the supplier and which consisted of Strep-Tag fusion protein (Amino acids 510–582 of the rat vGluT2). We mixed 2- μ g peptide with 1- μ l antibody and 0.5 ml 0.1 M PB. The preabsorption test abolished the immunoreactivity of the antibody in the cerebellar cortex and DCN (Fig. 1). As a positive control another section was stained at the same time with the normal staining protocol. The specificity of vGluT1, Kv3.3 and PCP2 was tested in previous studies (Alonso-Espinaco et al., 2008; Cheng et al., 2011; Hamodeh et al., 2014).

vGluT1, vGluT2, kv3.3 and Pcp2 staining patterns

An overview of the vGluT1, vGluT2, PCP2 channels and the merged image in the AIN and PIN is shown at low magnification (Fig. 2). The Kv3.3 channel is not shown. The staining shows different vGluT1 intensities between AIN and PIN (Fig. 2A). The vGluT2 staining shows the vGluT2-positive boutons and in addition the glutamatergic neuron somata (Fig. 2B). The Purkinje cell axons are shown in Fig. 2C. In Fig. 2D the three images have been merged and little overlap between vGluT1 and PCP2 or vGluT2 and PCP2 can be observed. An example image of the combination of the four antibodies with high magnification is shown in

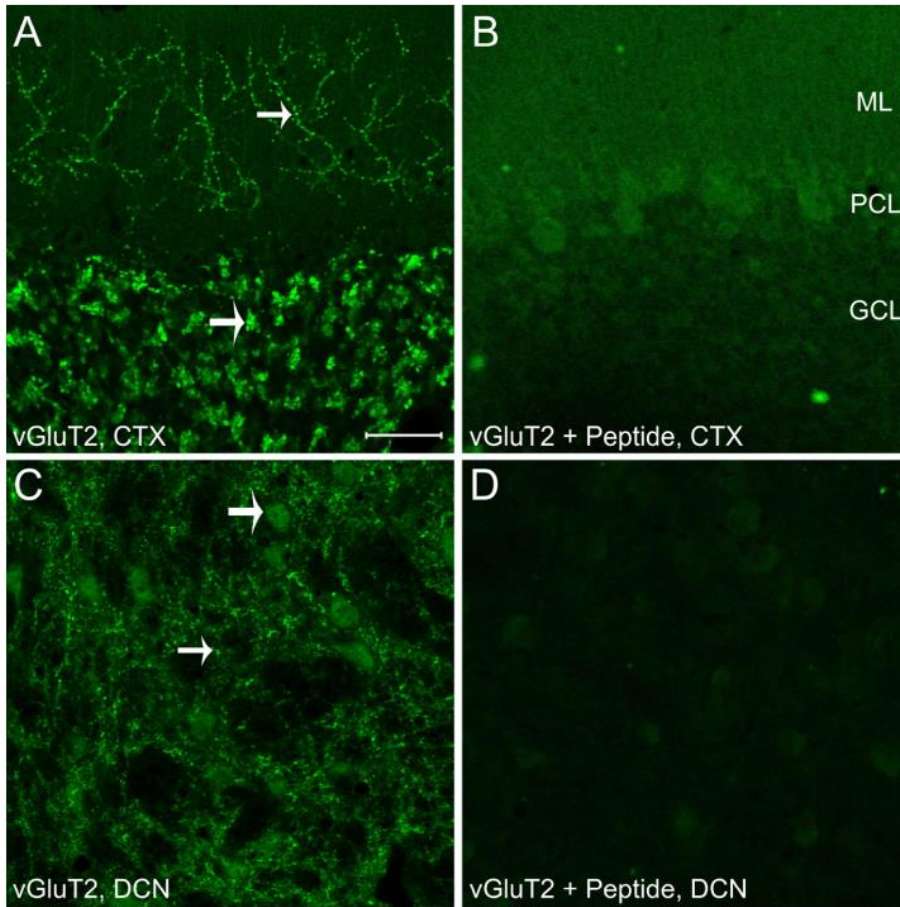


Fig. 1. Specificity test of vGluT2 in cerebellar cortex (CTX) and deep cerebellar nuclei (DCN). (A) and (C) shows the staining using the vGluT2 antibody. (B) and (D) show the abolished staining from the vGluT2 antibody preabsorbed with corresponding peptide. (A): in the cerebellar cortex, the climbing fibers (small arrow) in the molecular layer (ML) and the mossy fiber rosettes (big arrow) in the granule cell layer (GCL) were stained. (C) shows the staining of vGluT2 in DCN. The terminals of mossy or climbing fiber (small arrow) and the glutamatergic DCN neuron somata (big arrow) were stained.

Fig. 3A–E. Unlike vGluT2, vGluT1 only stained the bouton structures (Fig. 3A). However the somata of the DCN neurons were only weakly stained for vGluT2 compared to the bouton staining (Fig. 3B). The Purkinje cell axons can be seen surrounding the DCN neuron (Fig. 3C). The Kv3.3 staining can be seen mainly on the Purkinje cell axons and around the DCN neuron somata (Fig. 3D), confirming previous studies (Alonso-Espinaco et al., 2008; Chang et al., 2007). To further study the specificity of the antibodies we quantified the overlap between the different antibody staining's by performing a colocalization analysis using Pearson's correlation coefficient (Fig. 3F). Our result showed that Pearson's coefficients for the vGluT1&Kv3.3, vGluT2&Kv3.3, vGluT1&PCP2 and vGluT2&PCP2 are between -0.1 and 0. This indicates no or little colocalization between these antibody pairs. In contrast the Kv3.3&PCP2 colocalization yielded Pearson's coefficient of 0.24 (data not shown). This quantitatively confirms previous studies (Chang et al., 2007; Alonso-Espinaco et al., 2008; Puente et al., 2010). Pearson's coefficient of vGluT1 & vGluT2 is 0.17, which indicates some colocalization of vGluT1 and vGluT2, as has been observed in the spinal cord and superior olivary complex (Alvarez et al., 2004; Billups 2005).

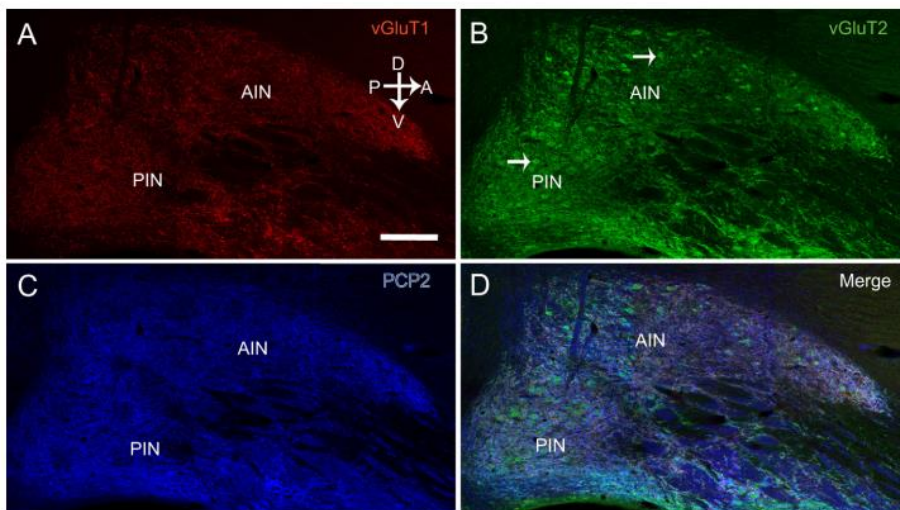


Fig. 2. Comparison of the vGluT1, 2 and PCP2 staining in rat AIN and PIN at low magnification. The quadruple staining was done on parasagittal cerebellar sections of the rat. (A): vGluT1 staining shows punctate structures in both AIN and PIN with heterogeneous density. (B): vGluT2 staining also shows in addition stained neuron soma (arrows) in both nuclei, with more intense staining in the PIN. (C) shows PCP2 staining and (D) shows the merged three channels (A–C). A, anterior; P, posterior; D, dorsal; V, ventral. Scale bar = 200 μm.

Density, volumes and shape parameters of vGluT1 and 2 profiles in the DCN

Our surface analysis allowed for visualization and quantification of the vGluT1 and vGluT2 structures. The z-stacks are shown in a 3-dimensional view for the vGluT1 and vGluT2 labeling from different nuclei (Fig. 4A, C, E, G). The staining in MN and AIN has a more clustered pattern than the ones in LN and PIN, which are more uniformly distributed. The surface view preserves the outlines of the reconstructed objects and removes the background (Fig. 4B, D, F and H). Our surface analysis allows for the following quantification of the number and volume of the labeled structures.

The surface density estimates for vGluT1 ranged from $3.5 \times 10^6 / \text{mm}^3$

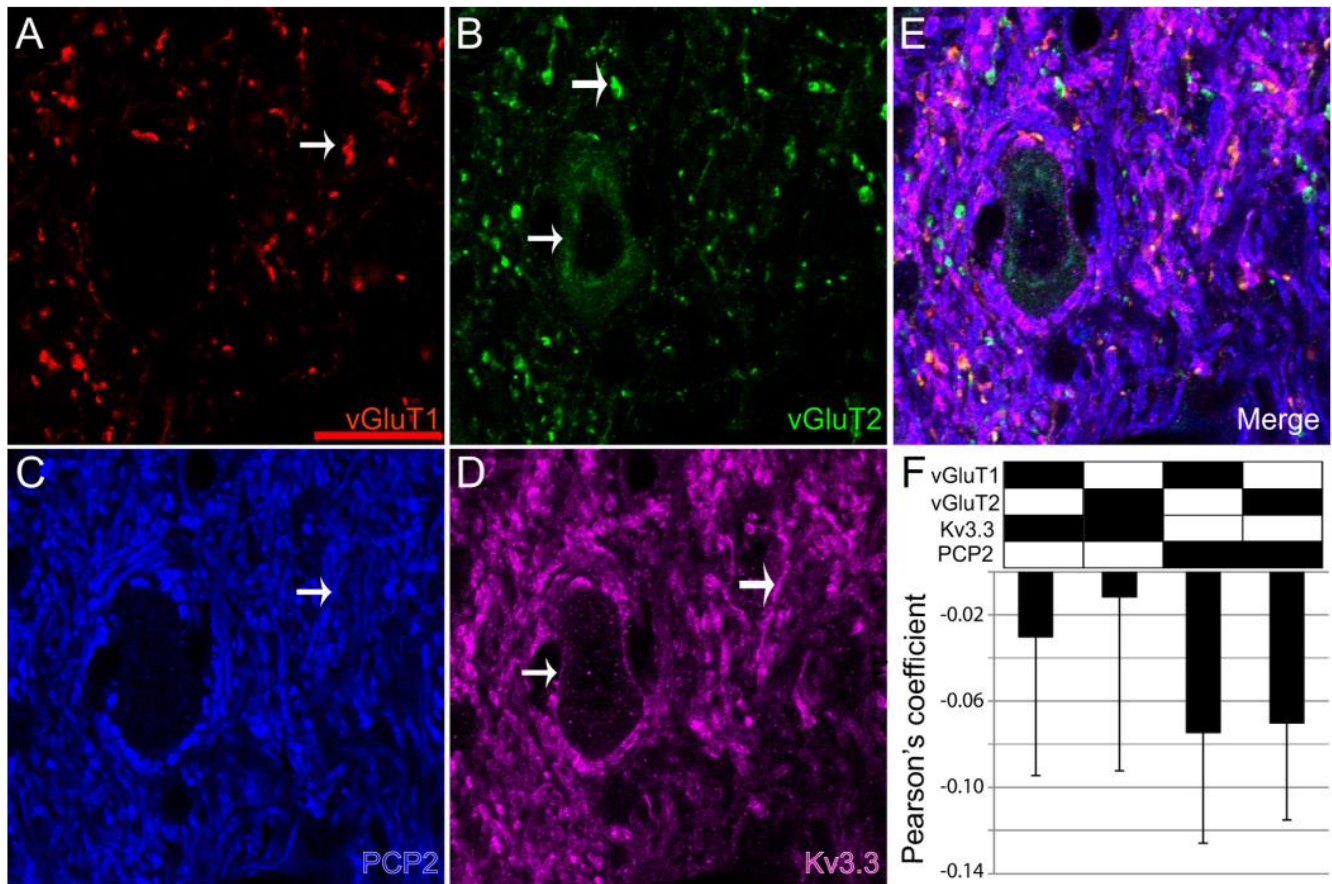


Fig. 3. An example of quadruple staining of the DCN. (A–E) shows the individual and merged channel under higher magnification. In (A) and (B), the vGluTs are shown as punctate structure (small arrow), and the soma of the DCN neuron is also stained by vGluT2 (large arrow). (C, D), the axons of Purkinje cells are stained by PCP2 and most of the Kv3.3 staining has a close relationship with Purkinje cell axons (small arrows in (C) and (D)). Kv3.3 can be seen on larger DCN neurons which outline the neuronal somata (large arrow in (D)). (F), Pearson's coefficient of within-voxel colocalization are shown for vGluT1 colocalization with Kv3.3 or PCP2, and vGluT2 colocalization with Kv3.3 or PCP2 in DCN. Scale bar in (A) is 20 μ m and also valid for (B–E).

(SEM = 8.5×10^5) to $7.2 \times 10^6/\text{mm}^3$ (SEM = 8.6×10^5), while vGluT2 ranged from $3.7 \times 10^6/\text{mm}^3$ (SEM = 3.2×10^5) to $5 \times 10^6/\text{mm}^3$ (SEM = 6.9×10^5) depending on the DCN sub nucleus. Data were power transformed and checked for normal distribution (Fig. 5A–D). A linear mixed effects model was performed (lmer in R) to test the variance explained by the different nuclei classification as a fixed effect and between subject variance as a random effect. The mean vGluT1 density was significantly higher in phylogenetically newer DCN: $7.2 \times 10^6/\text{mm}^3$ (SEM = 8.6×10^5) and $6.8 \times 10^6/\text{mm}^3$ (SEM = 7.4×10^5) in LN and PIN versus $3.5 \times 10^6/\text{mm}^3$ (SEM = 8.5×10^5) and $5.1 \times 10^6/\text{mm}^3$ (SEM = 5.6×10^5) in MN and AIN (analysis of variance of linear mixed effects model, chi-square = 50.339, df = 3, $p = 6.77 \times 10^{-11}$, eta squared = 0.21). The mean vGluT2 density was similar within most DCN between $3.7 \times 10^6/\text{mm}^3$ (SEM = 3.2×10^5) and $4.5 \times 10^6/\text{mm}^3$ (SEM = 4.6×10^5). Only the PIN had a slightly higher density ($5 \times 10^6/\text{mm}^3$; SEM = 6.9×10^5) significantly different from AIN (analysis of variance of linear mixed effects model, chi-square = 8.45, df = 3, $p = 0.037$, eta squared = 0.053) (Fig. 5E). The LN had a vGluT2 density of $4.5 \times 10^6/\text{mm}^3$ (SEM = 4.6×10^5) comparable to the

MN ($4.1 \times 10^6/\text{mm}^3$; SEM = 2.9×10^5) and AIN ($3.7 \times 10^6/\text{mm}^3$; SEM = 3.2×10^5).

The volumes of vGluT1+ and vGluT2+ boutons for all DCN were around $0.69 \mu\text{m}^3$ (SEM = 6.1×10^{-3}) and $0.51 \mu\text{m}^3$ (SEM = 3.1×10^{-2}), respectively (Fig. 5F). No significant differences were found for vGluT1 volumes (analysis of variance of linear mixed effects model, chi-square = 0.79, df = 3, $p = 0.85$). In contrast vGluT2 surfaces showed significant differences in size with the largest profiles found within the MN (analysis of variance of linear mixed effects model, chi-square = 21.28, df = 3, $p = 9.2 \times 10^{-5}$, eta squared = 0.13). The results from analysis of variance of the linear mixed effects models are summarized in Table A.2 and the post hoc test is summarized in Table A.3 (see Appendices).

We also studied the shape parameters of the surfaces (sphericity and ellipticity) to detect any outliers within the vGluT1 and 2 profiles. In Fig. 6 we plot sphericity and prolate ellipticity (detects object elongation) against surface size (diameter obtained from volume estimates). The 3D plots show a large homogenous cluster with only some surfaces forming a distinct cluster at low prolate ellipticity values (<0.2). We also obtained the

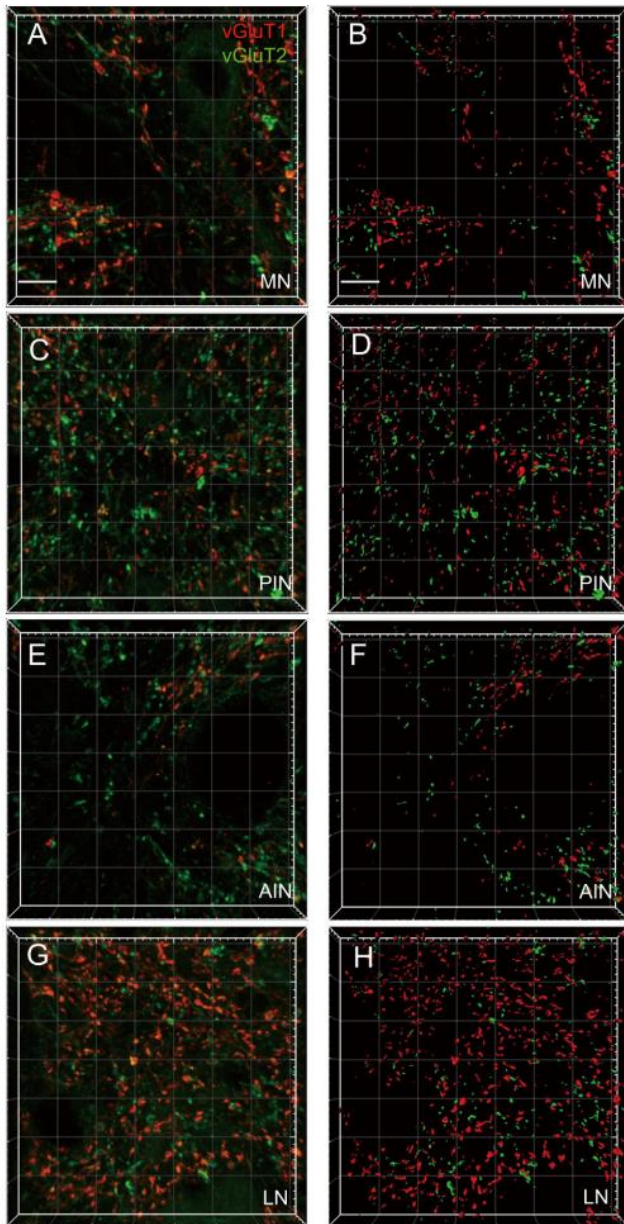


Fig. 4. Comparison of vGluT1- and vGluT2-stained structures and their surface reconstructions in different nuclei. The first column (A, C, E and G) are the projection views through a z-stack of confocal images (perspective at 45 degree). The second column (B, D, F and H) are the constructed surface views from Imaris. For vGluT1, the red channel, the thresholding method was based on Ridler-Calvard algorithm implemented in Imaris, for vGluT2, the green channel, the threshold level was user defined, at 25/255. Scale bar = 10 μ m in (A) and (B) and valid to all the other images.

percentage of the profiles within these distinct small clusters for the different sub nuclei for vGluT1 (MN: 0.06; AIN: 0.054; PIN: 0.054; LN: 0.051) and vGluT2 (MN: 0.06; AIN: 0.043; PIN: 0.047; LN: 0.041) and found comparable proportions in the different subnuclei.

DISCUSSION

Our results show that the subdivisions of the DCN have distinct organizations that show mainly differences in the density of vGluT1 immunolabeled profiles. This result

can be related to our previous findings of differences in dendritic and axonal wiring in the phylogenetically newer DCN (Hamodeh et al., 2014). However, we will first discuss the potential bias introduced by our approach to these differences and thereafter discuss its potential functional significance.

In this study we used systematic random sampling to obtain a sufficiently large number of probes to cover the variability between the different parts of the rat DCN. We took 3D z-stacks of laser confocal images in all probes to be able to reconstruct vGluT1 and 2 labeled surfaces with the Imaris software package to obtain their density and volumes. The size of boutons made by the climbing fiber collaterals in the DCN which express vGluT2 (Fremeau et al., 2001; Hisano et al., 2002) was estimated by Sugihara and colleagues (Sugihara et al., 1996) at 0.8–1.4 μ m comparable to our mean of 1 μ m. We have checked the shape parameters of our profiles and found only a small similar percentage (4–6%) of outliers in all DCN that could be due to false detections. Therefore this would not explain the difference we found in vGluT1 density in the different DCN.

We also compared our density estimates with values obtained previously. The density of the excitatory synapses has not been obtained so far. However, based on the number of boutons made by the climbing fiber collaterals in the DCN (54) and the number of climbing fiber branches to the Purkinje cells of 6.1 (Sugihara et al., 1996) together with the number of Purkinje cells (Harvey and Napper 1988), we would estimate a total of $54 \times 3.4 \times 10^5 / 6.1 = 3 \times 10^6$ climbing fiber boutons in the DCN. For the mossy fibers we would estimate 4×10^4 fibers (Sultan and Heck 2003) and 129 boutons per fiber (Wu et al., 1999) for a total of 5×10^6 . These two estimates together are an order of magnitude less than our vGluT1 and 2 profile estimates of 5.9×10^7 , which we would presume would be to some larger proportion originating from climbing fibers and mossy fibers. Our estimate would yield 240 vGluT1 and 184 vGluT2 boutons per DCN neuron (DCN neuron number of 1.4×10^5 (Hamodeh et al., 2014)). Based on these estimates it is not clear whether our approach has yielded an overestimate by detecting small profiles ($\sim 0.5 \mu$ m) or whether the climbing and mossy fiber boutons estimate by tracer injection (Sugihara et al., 1996) did not detect the smaller profiles. We have also taken tissue shrinkage into account and have found it less than our previous estimate yielding an additional potential source of bias. A comparison to the number of Purkinje cell synapses based on the number of boutons on an individual Purkinje cell axon makes in the DCN (122 (Sugihara et al., 2009)) and the number of Purkinje cells yields $122 \times 3.4 \times 10^5 = 4.15 \times 10^7$ Purkinje cell synapses in the DCN. This would then predict 296 Purkinje cell synapses per DCN neuron and an amount comparable to the vGluT1 and vGluT2 profiles that we would estimate based on our current approach (i.e., 240 vGluT1 labeled boutons + 184 vGluT2 labeled boutons – 28 (the vGluT1 and 2 colabeled bouton number, which we estimated at 11.6% of vGluT1 labeled boutons).

We found comparable levels of vGluT1 and 2 expressions in the DCN ($5.6 \times 10^6 / \text{mm}^3$ vs. $4.3 \times 10^6 / \text{mm}^3$).

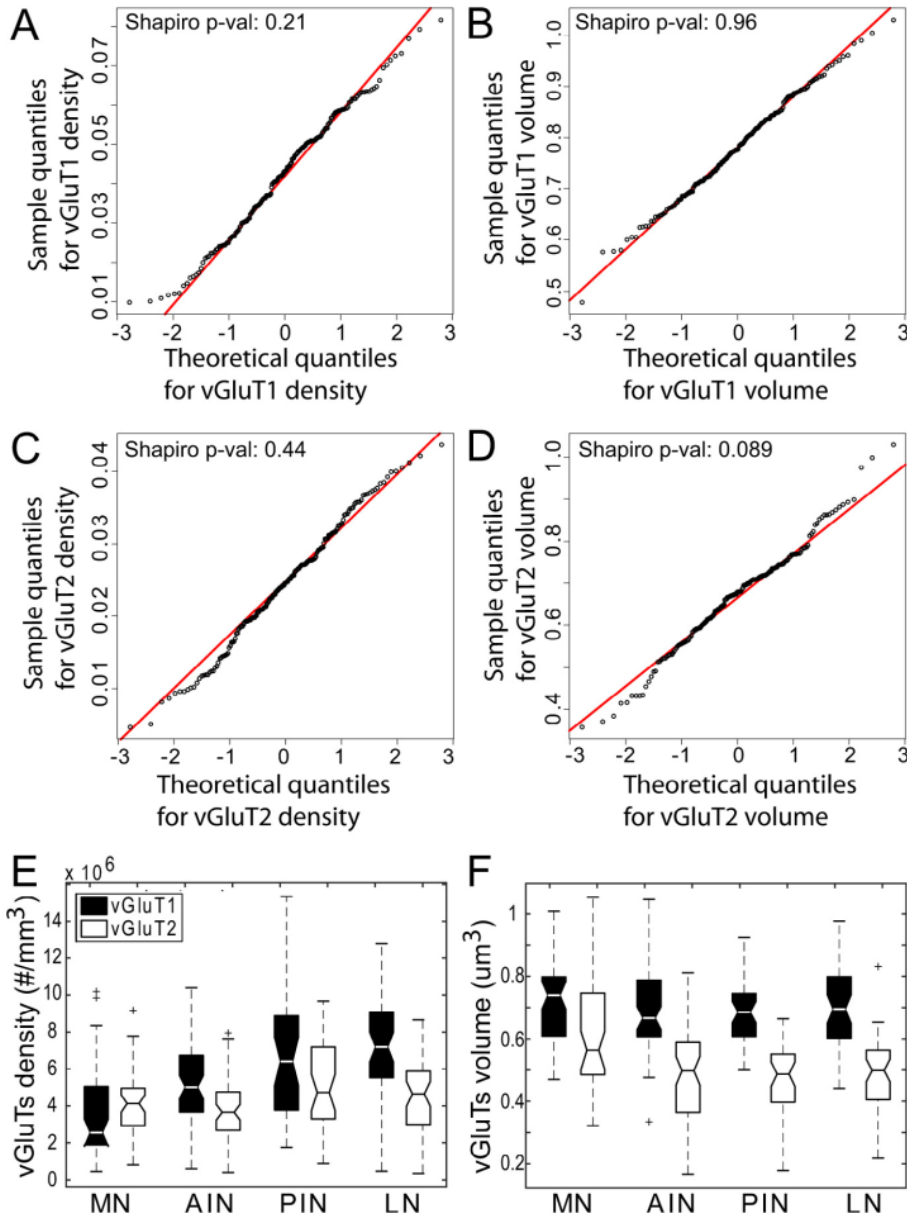


Fig. 5. Quantile-quantile plots of the power transformed data (A–D) and boxplots of the density and volume of vGluT1- and vGluT2-labeled boutons in different nuclei (E, F). The Shapiro p-values in (A–D) are larger than 0.05 indicating that the transformed vGluT1 and 2 density and volume data are derived from normally distributed populations. (E) shows the density of vGluT1 and vGluT2 profiles. The vGluT1 density is highest in LN and PIN and lowest in MN and AIN ($p = 6.77 \times 10^{-11}$). The vGluT2 density is highest in PIN and lowest in AIN ($p = 0.037$). (F) shows the volumes of vGluT1 and 2 profiles. The vGluT1 bouton volumes are not significantly different within the DCN ($p = 0.85$) while vGluT2 volume is bigger in MN ($p = 9.2 \times 10^{-5}$).

Our quantification confirms previous qualitative observations that indicate that both transporters are important in the cerebellum (Hioki et al., 2003). This is in contrast to most other brain regions where either of the transporters is expressed and indicates that those brain regions make specific use of the different properties of these two transporters. It has been suggested that vGluT1 is related to synapses with a low probability of vesicular release, whereas vGluT2 is related to high release probability (Fremeau et al., 2001; Varoqui et al., 2002; Petrof and Sherman 2013). In the DCN the presence of both transporters is likely due to the presence of

two separate pathways: the climbing and mossy fibers which process information differently, with the climbing fibers having a much lower firing frequency than the mossy fibers (Sultan et al., 2012; Delvendahl and Hallermann 2016). However, the presence of vGluT2 in a subpopulation of mossy fibers complicates this simplified view and further studies are required to quantify the proportion of mossy fibers expressing vGluT2 and clarify which brain regions they origin from.

Increased vGluT1 density in phylogenetically newer DCN

Our current analysis also yielded important differences in the density of vGluT1 and 2 profiles. We found a significantly higher density in the phylogenetically newer DCN (LN and PIN) compared to the older DCN (AIN and MN). The combined vGluT1 and 2 excitatory synaptic density is highest in PIN and LN, with the value of 11×10^6 and $10.9 \times 10^6/\text{mm}^3$ compared to $7.2 \times 10^6/\text{mm}^3$ and $8.2 \times 10^6/\text{mm}^3$ in the MN and AIN, respectively. Our previous analysis of dendrites and Purkinje cell axons showed that the LN and the PIN had higher fiber density in comparison to the AIN and MN (Hamodeh et al., 2014). One interpretation of the higher fiber density depended on whether the number of synapses is equally increased in these regions. Our current results show that this is indeed the case for the excitatory synapses. It is well established that during brain maturation there is an overshoot in the number of synapses at early developmental stages, which is then reduced later in the adult stage by synaptic pruning. This could reflect a pruning process that is more elaborated in phylogenetically newer parts

of the brain (Petanjek et al., 2011). Our observation implicates that this could affect mainly the vGluT1 synapses which is in line with the distribution pattern of this transporter in the phylogenetically newer and more modifiable parts of the brain (Hisano 2003; Herzog et al., 2004b).

ACKNOWLEDGMENTS

HM was funded by the Chinese Scholarship Council. This study was also supported by the Hertie foundation and the Tübingen University, by the German Research Foundation (DFG SU171.3-1 grant) and by Umeå

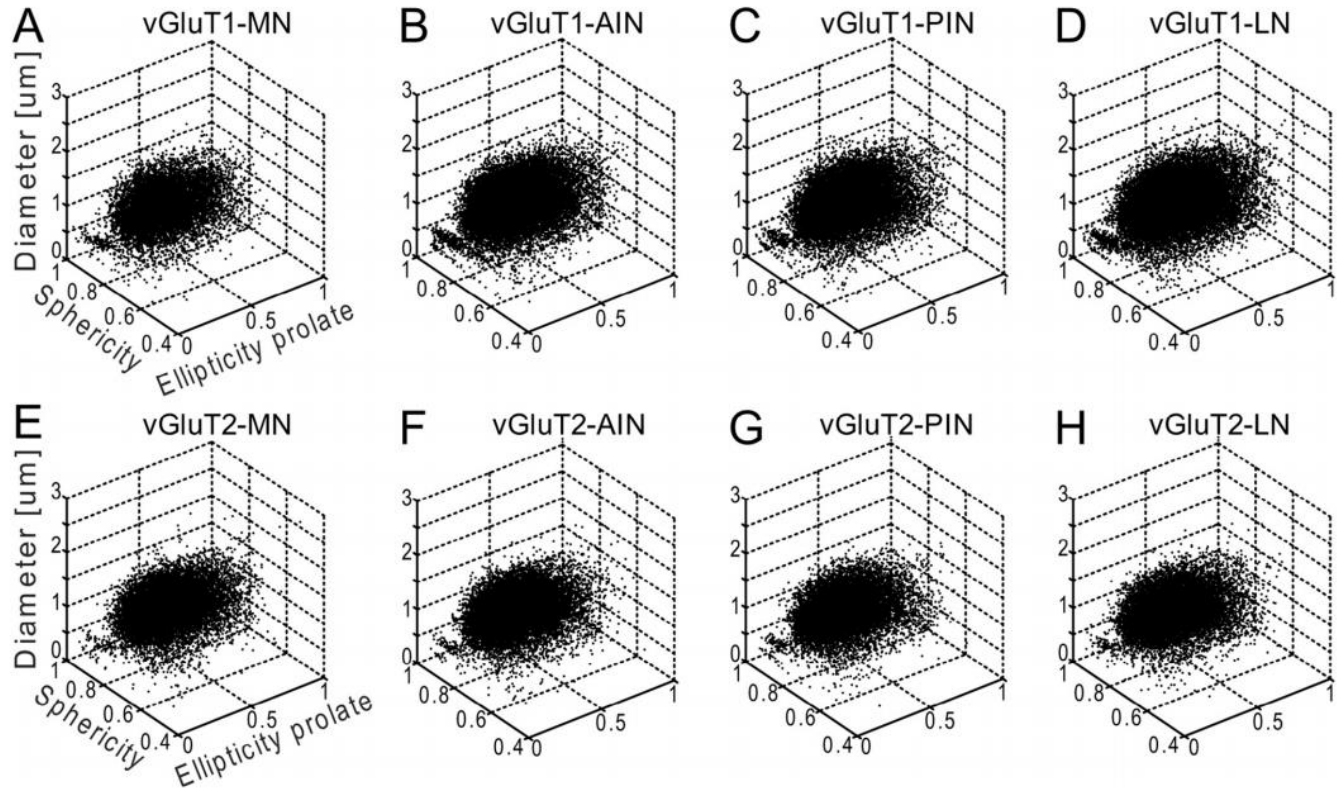


Fig. 6. Scatter plots of two shape parameters (sphericity and prolate ellipticity) and their relation to the profile diameters for vGluT1 (A–D) and vGluT2 (E–H). Plotted are the values for the different DCN subnuclei. The overall pattern is very similar with one large cluster encompassing most of the profiles and one smaller cluster (to the left of the larger cluster) showing potential outliers.

University to FS. We are thankful to Ute Grosshennig for assistance with the histology and Dr. Angelos Skodross for providing help with the laser confocal microscopy.

CONFLICT OF INTEREST STATEMENT

The authors have no conflicts of interest.

ROLE OF AUTHORS

HM and SH conducted the experiments and together with FS analyzed the data and wrote the manuscript. FS designed the project and provided for funding.

REFERENCES

- Aarts E, Verhage M, Veenliet JV, Dolan CV, van der Sluis S (2014) A solution to dependency: using multilevel analysis to accommodate nested data. *Nat Neurosci* 17:491–496.
- Abercrombie M (1946) Estimation of nuclear population from microtome sections. *Anat Record* 94:239–247.
- Aihara Y, Mashima H, Onda H, Hisano S, Kasuya H, Hori T, Yamada S, Tomura H, Yamada Y, Inoue I, Kojima I, Takeda J (2000) Molecular cloning of a novel brain-type Na(+)-dependent inorganic phosphate cotransporter. *J Neurochem* 74:2622–2625.
- Alonso-Espinaco V, Elezgarai I, Diez-Garcia J, Puente N, Knopfel T, Grandes P (2008) Subcellular localization of the voltage-gated potassium channels Kv3.1b and Kv3.3 in the cerebellar dentate nucleus of glutamic acid decarboxylase 67-green fluorescent protein transgenic mice. *Neuroscience* 155:1059–1069.
- Alvarez FJ, Villalba RM, Zerda R, Schneider SP (2004) Vesicular glutamate transporters in the spinal cord, with special reference to sensory primary afferent synapses. *J Comp Neurol* 472:257–280.
- Angaut P, Sotelo C (1973) The fine structure of the cerebellar central nuclei in the cat. II. Synaptic organization. *Exp Brain Res* 16:431–454.
- Bellocchio EE, Hu H, Pohorille A, Chan J, Pickel VM, Edwards RH (1998) The localization of the brain-specific inorganic phosphate transporter suggests a specific presynaptic role in glutamatergic transmission. *J Neurosci* 18:8648–8659.
- Billups B (2005) Colocalization of vesicular glutamate transporters in the rat superior olivary complex. *Neurosci Lett* 382:66–70.
- Bostan AC, Dum RP, Strick PL (2013) Cerebellar networks with the cerebral cortex and basal ganglia. *Trends Cogn Sci* 17:241–254.
- Boulland JL, Qureshi T, Seal RP, Rafiki A, Gundersen V, Bergersen LH, Fremereau Jr RT, Edwards RH, Storm-Mathisen J, Chaudhry FA (2004) Expression of the vesicular glutamate transporters during development indicates the widespread corelease of multiple neurotransmitters. *J Comp Neurol* 480:264–280.
- Braitenberg V, Schüz A (1998) *Cortex: Statistics and Geometry of Neuronal Connectivity*. Berlin Heidelberg New York: Springer-Verlag.
- Chang SY, Zagha E, Kwon ES, Ozaita A, Bobik M, Martone ME, Ellisman MH, Heintz N, Rudy B (2007) Distribution of Kv3.3 potassium channel subunits in distinct neuronal populations of mouse brain. *J Comp Neurol* 502:953–972.
- Cheng X-R, Yang Y, Zhou W-X, Zhang Y-X (2011) Expression of VGLUTs contributes to degeneration and acquisition of learning and memory. *Neurobiol Learn Mem* 95:361–375.
- Costes SV, Daelemans D, Cho EH, Dobbin Z, Pavlakis G, Lockett S (2004) Automatic and quantitative measurement of protein-protein colocalization in live cells. *Biophys J* 86:3993–4003.
- De Zeeuw CI, Berrebi AS (1995) Postsynaptic targets of Purkinje cell terminals in the cerebellar and vestibular nuclei of the rat. *Eur J Neurosci* 7:2322–2333.
- De Zeeuw CI, Ten Brinke MM (2015) Motor Learning and the Cerebellum. *CSH Perspec Biol* 7:a021683.

- Delvendahl I, Hallermann S (2016) The Cerebellar Mossy Fiber Synapse as a Model for High-Frequency Transmission in the Mammalian CNS. *Trends Neurosci* 39:722–737.
- Fremeau Jr RT, Voglmaier S, Seal RP, Edwards RH (2004) VGLUTs define subsets of excitatory neurons and suggest novel roles for glutamate. *Trends Neurosci* 27:98–103.
- Fremeau RT, Kam K, Qureshi T, Johnson J, Copenhagen DR, Storm-Mathisen J, Chaudhry FA, Nicoll RA, Edwards RH (2004) Vesicular glutamate transporters 1 and 2 target to functionally distinct synaptic release sites. *Science* 304:1815–1819.
- Fremeau RT, Troyer MD, Pahner I, Nygaard GO, Tran CH, Reimer RJ, Bellocchio EE, Fortin D, Storm-Mathisen J, Edwards RH (2001) The expression of vesicular glutamate transporters defines two classes of excitatory synapse. *Neuron* 31:247–260.
- Gras C, Herzog E, Bellenchi GC, Bernard V, Ravassard P, Pohl M, Gasnier B, Giros B, El Mestikawy S (2002) A third vesicular glutamate transporter expressed by cholinergic and serotonergic neurons. *J Neurosci* 22:5442–5451.
- Haass-Koffler CL, Naeemuddin M, Bartlett SE (2012), An analytical tool that quantifies cellular morphology changes from three-dimensional fluorescence images. *JOVE-J Vis*: e4233.
- Hamodeh S, Sugihara I, Baizer J, Sultan F (2014) Systematic analysis of neuronal wiring of the rodent deep cerebellar nuclei reveals differences reflecting adaptations at the neuronal circuit and internuclear level. *J Comp Neurol* 522:2481–2497.
- Hamodeh S, Bozkurt A, Mao H, Sultan F (2017) Uncovering specific changes in network wiring underlying the primate cerebrotypes. *Brain Struct Funct*. <https://doi.org/10.1007/s00429-017-1402-6>.
- Hartig W, Riedel A, Grosche J, Edwards RH, Fremeau RT, Harkany T, Brauer K, Arendt T (2003) Complementary distribution of vesicular glutamate transporters 1 and 2 in the nucleus accumbens of rat: Relationship to calretinin-containing extrinsic innervation and calbindin-immunoreactive neurons. *J Comp Neurol* 465:1–10.
- Harvey RJ, Napper RM (1988) Quantitative study of granule and Purkinje cells in the cerebellar cortex of the rat. *J Comp Neurol* 274:151–157.
- Herzog E, Bellenchi GC, Gras C, Bernard V, Ravassard P, Bedet C, Gasnier B, Giros B, El Mestikawy S (2001), The existence of a second vesicular glutamate transporter specifies subpopulations of glutamatergic neurons. *J Neurosci* 21: RC181.
- Herzog E, Gilchrist J, Gras C, Muzerelle A, Ravassard P, Giros B, Gaspar P, El Mestikawy S (2004) Localization of VGLUT3, the vesicular glutamate transporter type 3, in the rat brain. *Neuroscience* 123:983–1002.
- Herzog E, Landry M, Buhler E, Bouali-Benazzouz R, Legay C, Henderson CE, Nagy F, Dreyfus P, Giros B, El Mestikawy S (2004) Expression of vesicular glutamate transporters, VGLUT1 and VGLUT2, in cholinergic spinal motoneurons. *Eur J Neurosci* 20:1752–1760.
- Hioki H, Fujiyama F, Taki K, Tomioka R, Furuta T, Tamamaki N, Kaneko T (2003) Differential distribution of vesicular glutamate transporters in the rat cerebellar cortex. *Neuroscience* 117:1–6.
- Hisano S (2003) Vesicular glutamate transporters in the brain. *Anat Sci Int* 78:191–204.
- Hisano S, Sawada K, Kawano M, Kanemoto M, Xiong G, Mogi K, Sakata-Haga H, Takeda J, Fukui Y, Nogami H (2002) Expression of inorganic phosphate/vesicular glutamate transporters (BNPI/VGLUT1 and DNPI/VGLUT2) in the cerebellum and precerebellar nuclei of the rat. *Mol Brain Res* 107:23–31.
- Kaneko T, Fujiyama F (2002) Complementary distribution of vesicular glutamate transporters in the central nervous system. *Neurosci Res* 42:243–250.
- Kaneko T, Fujiyama F, Hioki H (2002) Immunohistochemical localization of candidates for vesicular glutamate transporters in the rat brain. *J Comp Neurol* 444:39–62.
- Ni B, Du Y, Wu X, DeHoff BS, Rosteck PR, Paul SM (1996) Molecular cloning, expression, and chromosomal localization of a human brain-specific Na(+)-dependent inorganic phosphate cotransporter. *J Neurochem* 66:2227–2238.
- Ni B, Rosteck PR, Nadi NS, Paul SM (1994) Cloning and expression of a cDNA encoding a brain-specific Na(+)-dependent inorganic phosphate cotransporter. *P Natl Acad Sci USA* 91:5607–5611.
- Ni B, Wu X, Yan GM, Wang J, Paul SM (1995) Regional expression and cellular localization of the Na(+)-dependent inorganic phosphate cotransporter of rat brain. *J Neurosci* 15:5789–5799.
- Palkovits M, Mezey E, Hamori J, Szentagothai J (1977) Quantitative histological analysis of the cerebellar nuclei in the cat. I. Numerical data on cells and on synapses. *Exp Brain Res* 28:189–209.
- Petanjek Z, Judas M, Simic G, Rasin MR, Uylings HB, Rakic P, Kostovic I (2011) Extraordinary neoteny of synaptic spines in the human prefrontal cortex. *P Natl Acad Sci USA* 108:13281–13286.
- Petrof I, Sherman SM (2013) Functional significance of synaptic terminal size in glutamatergic sensory pathways in thalamus and cortex. *J Physiol* 591:3125–3131.
- Puente N, Mendizabal-Zubiaga J, Elezgarai I, Reguero L, Buceta I, Grandes P (2010) Precise localization of the voltage-gated potassium channel subunits Kv3.1b and Kv3.3 revealed in the molecular layer of the rat cerebellar cortex by a pre-embedding immunogold method. *Histochem Cell Biol* 134:403–409.
- Ridler TW, Calvard S (1978) Picture thresholding using an iterative selection method. *IEEE T Syst Man Cyb* 8:630–632.
- Sugihara I, Fujita H, Na J, Quy PN, Li BY, Ikeda D (2009) Projection of reconstructed single Purkinje cell axons in relation to the cortical and nuclear aldolase C compartments of the rat cerebellum. *J Comp Neurol* 512:282–304.
- Sugihara I, Wu H, Shinoda Y (1996) Morphology of axon collaterals of single climbing fibers in the deep cerebellar nuclei of the rat. *Neurosci Lett* 217:33–36.
- Sultan F, Augath M, Hamodeh S, Murayama Y, Oeltermann A, Rauch A, Thier P (2012) Unravelling cerebellar pathways with high temporal precision targeting motor and extensive sensory and parietal networks. *Nat Commun* 3:924.
- Sultan F, Hamodeh S, Baizer JS (2010) The human dentate nucleus: a complex shape untangled. *Neuroscience* 167:965–968.
- Sultan F, Heck D (2003) Detection of sequences in the cerebellar cortex: numerical estimate of the possible number of tidal-wave inducing sequences represented. *J Physiol-Paris* 97:591–600.
- Takamori S, Rhee JS, Rosenmund C, Jahn R (2000) Identification of a vesicular glutamate transporter that defines a glutamatergic phenotype in neurons. *Nature* 407:189–194.
- Tellmann S, Bludau S, Eickhoff S, Mohlberg H, Minnerop M, Amunts K (2015) Cytoarchitectonic mapping of the human brain cerebellar nuclei in stereotaxic space and delineation of their co-activation patterns. *Front Neuroanat* 9:54.
- Varoqui H, Schafer MK, Zhu H, Weihe E, Erickson JD (2002) Identification of the differentiation-associated Na⁺/PI transporter as a novel vesicular glutamate transporter expressed in a distinct set of glutamatergic synapses. *J Neurosci* 22:142–155.
- Wu HS, Sugihara I, Shinoda Y (1999) Projection patterns of single mossy fibers originating from the lateral reticular nucleus in the rat cerebellar cortex and nuclei. *J Comp Neurol* 411:97–118.

APPENDICES

See Tables A.1–A.3

Table A.1. Multichannel laser confocal microscopy parameters. Four different secondary antibodies were used with the corresponding primary antibodies. The fluorophores were excited at their optimal wavelength and the emissions were collected by different band pass or long pass filters. Two tracks were used during acquisition process in order to minimize channel interference. The pinhole for every channel was optimized to 1 airy unit. XY voxel size was set to 0.14um X 0.14um by choosing a matrix size of 512 × 512 pixels. The z-stack interval was 0.32um and we took on average 30 optical sections

1st Antibody	2rd Antibody	Excitation(nm)	Emission(nm)	Track number
Goat vGluT1	Donkey anti goat Alexa flour 488	488	505–550	1
Guinea pig vGluT2	Goat anti guinea pig Alexa flour 633	633	LP 650	1
Mouse PCP2	Goat Anti mouse Alexa flour 405	405	420–480	2
Rabbit kv3.3	Goat anti rabbit cy3	543	560–615	2

Table A.2. Analysis of variance of linear mixed effects models and summary of post hoc analysis (Tukey) of vGluT1+ and vGluT2+ bouton density and volume size (dependent variables) and DCN classification (fixed effect). Smaller than symbol in the post hoc test means significantly lower while larger than symbol means significantly higher. df, degrees of freedom; lambda: exponent of power transformation; ICC: intra cluster correlation; chi-square and *p*-value for ANOVA test which compares lmer models with and without the fixed effect (nuclei)

	Threshold level	Dependent variables	df	Lambda	ICC	chi-square	<i>p</i> -value	Summary of post hoc tests
vGluT1	R-C (20.5 ± 5.7)	Density	3	0.6	0.05	50.34	6.77*10 ⁻¹¹	MN < AIN < (PIN&LN)
	R-C (20.5 ± 5.7)	Volume	3	0.68	0.07	0.79	0.85	n.s.
vGluT2	25	Density	3	0.68	0.07	8.45	0.037	AIN < PIN
	25	Volume	3	0.58	0.11	21.28	9.2*10 ⁻⁵	MN > (AIN&PIN&LN)

Table A.3. Post-hoc analysis (Tukey) of power transformed vGluT1+ and vGluT2+ bouton density and volume size. Estimates of the mean differences of the power transformed data, standard errors, *z*-values and *p*-values between nuclei were obtained from the post hoc analysis. *P* values were adjusted with Holm-Bonferroni correction

	Contrast	Estimate of difference	SE	<i>z</i> -value	<i>p</i> -value (corr.)
vGluT1 density	MN–AIN	–0.01	0.0027	–3.92	0.0004
	LN–AIN	0.0088	0.0026	3.34	0.0026
	PIN–AIN	0.0068	0.0028	2.46	0.027
	LN–MN	0.019	0.0028	6.91	2.86*10 ⁻¹¹
	PIN–MN	0.017	0.0029	5.89	1.99*10 ⁻⁸
	PIN–LN	–0.0020	0.0029	–0.68	0.50
vGluT1 volume	MN–AIN	0.0030	0.019	0.16	1
	LN–AIN	–0.0081	0.019	–0.43	1
	PIN–AIN	–0.013	0.020	–0.66	1
	LN–MN	–0.011	0.020	–0.56	1
	PIN–MN	–0.016	0.021	–0.77	1
	PIN–LN	–0.0048	0.021	–0.23	1
vGluT2 density	MN–AIN	0.00088	0.0016	0.56	0.83
	LN–AIN	0.0022	0.0016	1.43	0.61
	PIN–AIN	0.0045	0.0016	2.77	0.034
	LN–MN	0.0013	0.0016	0.82	0.83
	PIN–MN	0.0037	0.0017	2.10	0.18
	PIN–LN	0.0023	0.0017	1.33	0.61
vGluT2 volume	MN–AIN	0.075	0.021	3.54	0.0016
	LN–AIN	–0.012	0.021	–0.59	1
	PIN–AIN	–0.017	0.022	–0.78	1
	LN–MN	–0.088	0.022	–3.95	0.00046
	PIN–MN	–0.092	0.023	–3.95	0.00046
	PIN–LN	–0.0048	0.023	–0.20	1

Appendix 3:

Haian Mao, Salah Hamodeh, Angelos Skodras, Fahad Sultan. Quantitative organization of the excitatory synapses of the primate cerebellar nuclei: further evidence for a specialized architecture underlying the primate cerebellum. Brain Structure and Function, accepted

[Click here to view linked References](#)

1 *Title: Quantitative organization of the excitatory synapses of the primate*
2 *cerebellar nuclei: further evidence for a specialized architecture*
3 *underlying the primate cerebellum*

4 Haian Mao¹, Salah Hamodeh¹, Angelos Skodras², Fahad Sultan^{3*}

5 1, Department of Cognitive Neurology, Hertie Institute for Clinical Brain Research, Otfried-Müller-Str. 27,
6 72076 Tübingen, Germany

7 2, Department of Cellular Neurology, Hertie Institute for Clinical Brain Research, Otfried-Müller-Str. 27,
8 72076 Tübingen

9 3, Department of Integrative Medical Biology, Umeå University, Linnéus väg 9, 901 87 Umeå, Sweden

10 **Corresponding author:*

11 Fahad Sultan

12 Department of Integrative Medical Biology

13 Umeå University, Linnéus väg 9, 901 87 Umeå, Sweden

14 Tel: +46-90-786-5352

15 E-mail: fahad.sultan@umu.se

16

17 *Number of figures:* 5 main figure +5 extended data figures

18 *Number of tables:* 2

19 *Abstract:* 250 words (Maximum 250)

20 *Significance:* 105 words

21 *Introduction:* 680 words

22 *Discussion:* 1311 words

23

24 **Conflict of Interest:** The authors declare no competing financial interests.

25 **Acknowledgments:** HM was funded by the Chinese Scholarship Council. This study was also supported by
26 the Hertie Foundation, Tübingen University, the German Research Foundation (DFG SU171.3-1 grant) and
27 (FS) the Department of Integrative medical biology, Umeå University. We are thankful to Ute Grosshennig
28 for excellent assistance with the histology.

29

30

31

32

33

1 Abstract

2 The cerebellar intrinsic connectivity is of remarkable regularity with a similar build repeated many times
3 over. However, several modifications of this basic circuitry occur that can provide important clues to
4 evolutionary adaptations. We have observed differences in the wiring of the cerebellar output structures
5 (the deep cerebellar nuclei, DCN) with higher dendritic length density in the phylogenetically newer DCN.
6 In rats, we showed that an increase in wiring is associated with an increase in the presynaptic vesicular
7 glutamate transporter 1 (vGluT1). In this study, we have extended our analysis to the rhesus monkey and
8 can show similarities and differences between the two species. The similarities confirm a higher density
9 in vGluT1+ boutons in the lateral (LN/dentate) and posterior interpositus nucleus (PIN) compared to the
10 phylogenetically older DCN. In general, we also observe a lower density of vGluT1 and 2+ boutons in the
11 monkey, which however, yields a similar number of excitatory boutons per neuron in both species. The
12 only exception is the vGluT1+ boutons in the macaque LN/dentate, which showed a significantly lower
13 number of vGluT1+ boutons per neuron. We also detected a higher percentage of co-labelled vGluT1 and
14 2 boutons in the macaque than we found in the rat. In summary, these results confirm that the
15 hyposcaled dendrites of the monkey LN/dentate also show a lower number of vGluT1+ boutons per
16 neuron. These results provide further support of our model relating the dendritic morphology of the
17 LN/dentate neurons to the morphology of the specially enlarged LN/dentate nucleus in primates.

18 **Key words:** vesicular glutamate transporter, lipofuscin fluorescence removal, deep cerebellar nuclei,
19 quantitative immunofluorescence, comparative neuroanatomy.

20 **Significant statement:** We have quantified the excitatory synapses by studying the vesicular glutamate
21 transporter (vGluT) 1 and 2 in the primate cerebellar nuclei by using a novel approach to mask lipofuscin
22 autofluorescence. Our findings confirm our previous data from the rat of a higher vGluT1+ bouton density
23 in the phylogenetically newer cerebellar nuclei of the macaque. We also find a similar number of
24 excitatory boutons per neuron comparing rat and monkey pointing to a conserved modular organization
25 of the cerebellum with similar number of neurons per module. Our findings also confirm our model of
26 hyposcaled dendrites and vGluT1+ inputs to the specifically enlarged LN/ dentate of primates.

27

28

1 Introduction

2 The deep cerebellar nuclei (DCN) are a key component of the cerebellar circuitry and the main output of
3 the cerebellum. The activity of DCN neurons is controlled by the integration of inhibitory synaptic input
4 from the cerebellar cortex (i.e., the Purkinje cell axons) and excitatory input from the precerebellar nuclei.
5 The precerebellar afferents are from a wide source of brainstem nuclei conveying vestibular,
6 somatosensory, visual, auditory stimuli and from the basilar pontine nuclei conveying cerebral
7 information. There are two large groups of output neurons within the DCN. An excitatory projection group
8 that provides glutamatergic inputs to different brain regions within the brainstem (e.g., the red nucleus)
9 and the cerebral cortex (via specific thalamic relay nuclei). In contrast, the other group is GABAergic and
10 only targets the inferior olive nuclei. Both paths are also involved in recurrent circuits that feed back to
11 the DCN and cerebellar cortex either via the collaterals of the mossy fibers or of the climbing fibers. In
12 classical conditioning learning tasks, such as the Pavlovian eyeblink conditioning, the mossy fibers have
13 been shown to convey the conditioned stimulus, whereas the climbing fibers provide the unconditioned
14 stimulus to the DCN and cerebellar cortex [1, 2]. This dichotomy is further underlined by the presence of
15 two vesicular glutamate transporters (vGluT1 and 2) used by the two paths in different ways: the climbing
16 fibers exclusively use vGluT2, while all mossy fiber express vGluT1. It is noteworthy that a substantial
17 subpopulation of mossy fibers also co-expresses vGluT2 [3-5] and it is still unclear what functional role
18 this colabelling provides.

19 Based on the expression of vGluT1 and 2 in the climbing and mossy fiber DCN collaterals, immunolabeling
20 these two transporters is an ideal way of marking all the excitatory axon terminals in the DCN. Using this
21 approach together with systematic unbiased sampling of the rat DCN we were able to show that both
22 transporters are expressed in the DCN in similar proportions. However, we also found that vGluT1+
23 bouton density is significantly higher in the phylogenetically newer lateral nucleus/dentate (LN/dentate)
24 and posterior interpositus nucleus (PIN) compared to the phylogenetically older DCN (medial nucleus: MN
25 and anterior interpositus nucleus: AIN). In contrast the vGluT2+ bouton density did not show any
26 significant difference between the different DCN [6]. These findings is in agreement with the general brain
27 pattern of vGluT1 and 2 expression, with the former predominantly expressed in the phylogenetically
28 newer brain regions (cerebral cortex) and the later in subcortical regions such as the midbrain and
29 thalamic nuclei [7]. Based on this view our first prediction would be that in primates with an enlarged
30 neocerebellum the density of vGluT1+ boutons in the LN/dentate should also be increased within this
31 nucleus. However, it is not clear whether the results from the rat LN/dentate can be generalized to
32 primates. In fact a different prediction emerges if we look at the wiring components within the DCN. In a
33 previous study [8], we quantified and compared the wiring components between the rat and rhesus
34 monkey DCN. We found that although the dendritic length density (dendritic length per tissue volume)
35 was increased within the LN/dentate, a different picture emerged when we compared the dendritic length

1 per neuron (dendritic length density normalized by neuron density). Here we found that the LN/dentate
2 had less dendritic length per neuron than would have been predicted by the overall volume of the primate
3 LN/dentate. We termed this observation hyposcaling of dendrites and related it to the flattened shape of
4 the LN/dentate. Therefore, the quantification of the vGluTs in the primate LN/dentate could clarify
5 whether we also observe a hyposcaling of the excitatory synapses in this nucleus.

6 Our immunofluorescence approach that we established in the rodent should also be applicable to the
7 primate brain tissue on the basis of antigen homology [9]. However, the presence of lipofuscin
8 complicates this approach [10], due to its broad emission spectrum. In this study, we therefore modified
9 an approach from flow cytometry [11-13] to remove the lipofuscin emission. This required acquiring an
10 additional lipofuscin specific channel and using that to mask the vGluT1 and vGluT2 signals during
11 postprocessing.

12 Experimental procedure

13 Tissue preparation

14 All animal experiments were carried out in accordance with the Society for Neuroscience and local
15 German authorities (approved by the regional authorities (Regierungspräsidium Tübingen). Brain tissue
16 from two male adult macaques was used in this study (D98: body weight 17kg and 18 years old, H01: body
17 weight 9kg and 13 years old). Following premedication with a mixture of ketamine (20mg/100g body
18 weight), xylazine (2mg/100g body weight) deep anesthesia was induced with pentobarbital (400 mg/kg).
19 The animals were then perfused transcardially by 0.1M PB and then by 4% ice-cold paraformaldehyde in
20 0.1M phosphate buffer (PB) at pH 7.4. The brain was immediately dissected out of the skull and then
21 cryoprotected in an ascending concentration of sucrose (10%, 20%, and 30% in 0.1M PB). The cerebellum
22 was removed from the brainstem and mounted on a microtome with the lateral side facing the freezing
23 platform. Sections of 40 μ m (D98) or 50 μ m (H01) were serially acquired and stored in 0.1M PB.
24 Immunofluorescence staining was carried out on free floating sections. Prior to primary antibody
25 incubation, sections were washed 3 times in 0.1M PB for 5 minutes each time and then blocked in 0.1M
26 PB with 10% horse serum (PAA Laboratories, Coelbe, Germany) and 0.3% Triton X-100 at room
27 temperature for 1 hour.

28 Immunofluorescence

29 The concentration and incubation times were tested for each antibody in single stains. The optimized
30 conditions were then used for the multiple stains. We performed a quadruple staining protocol for vGluT1,
31 vGluT2, Purkinje Cell Protein 2(PCP2), and potassium channel KCNC3/Kv3.3 on H01, and a further
32 quadruple staining protocol for vGluT1, vGluT2, MAP2 and KCNC3/kv3.3 on D98. Data of the Kv3.3 were
33 used for a subsequent publication. The sections were first incubated with goat vGluT1 (sc-13320, Santa
34 Cruz Biotechnology, Texas) at 1:1000 and 4°C for 16hrs, followed by 3x washes in 0.1M PB and then

1 incubated with donkey anti goat Alexa Fluor 488 at 1:500 for 2hrs at room temperature. The sections were
2 then washed 3 times in PB before incubation with a combination of three antibodies of vGluT2 (1:1000,
3 lot number: 135404, Synaptic systems, North Saanich British Columbia) , Kv3.3 (1:500, lot number: APC-
4 102, Alomone labs, Israel) and PCP2 (1:200, lot number: sc-137064, Santa Cruz Biotechnology, Texas) or
5 MAP2 (1:200, lot number: M1406, Sigma Aldrich) at 4°C for 16 hrs. The sections were then washed and
6 incubated with the combinations of the three secondary antibodies: goat anti guinea pig Alexa Fluor 633
7 (1:500, A21105, Invitrogen, California), goat anti rabbit Cy3 (1:500, lot number: 81-6115, Invitrogen,
8 California) and goat anti mouse Alexa Fluor 405 (1:500, lot number: A31553, Invitrogen, California) for
9 2hrs at room temperature. Sections were then washed and mounted in glycerol on glass slides with
10 Mowiol 4–88 (Merck, Darmstadt, Germany). The slides were stored at 4°C.

11 *Preabsorption test of vGluT2 antibody*

12 To test for vGluT2 antigen-antibody specificity, we mixed 1ul vGluT2 antibody with 2ul of the peptide that
13 was used for immunization and was provided by the supplier. This consisted of Strep-Tag fusion protein
14 (Amino acids 510-582 of the rat vGluT2) in 500ul 0.5M PB solution with 2% horse serum and 0.1% tritonX-
15 100. The mixture was rotated at room temperature for 1 hour to allow for full interaction of the peptide
16 with the antibody. As a control solution we used 1ul vGluT2 antibody diluted in 500ul 0.5M PB solution
17 with 2% horse serum and 0.1% tritonX-100. Two adjacent cerebellar sections from the same series of
18 monkey H01 were washed and blocked. One section was incubated in the antigen-antibody mixture and
19 the other in the control solution for 48 hours at 4 degrees with constant rotation. The two sections were
20 washed and incubated with goat anti guinea pig Alexa Flour 633 1:1000 for 2 hours at room temperature.
21 The sections were washed, mounted, and scanned with laser confocal microscope LSM 510. VGLuT2
22 channel was scanned under the excitation of 633nm and emission at 650-750nm, while lipofuscin channel
23 was scanned under the excitation of 405nm and emission at 650-750nm.

24 *Data acquisition*

25 Images were acquired on a laser scanning confocal microscope (LSM 510, Carl Zeiss, Jena, Germany). We
26 took overview images of vGluT1 staining for every section with 488nm excitation and emission band pass
27 filtering 505-550nm at low magnification (10x objective). Probe positions were determined by first
28 marking an identifiable origin (x, y coordinates: 0,0) and then determining the position of the other probes
29 in the DCN region at a regular spacing of 1000um X 1000um. The location of the origin point was chosen
30 from an easily identifiable structure (i.e., vessels) within a core region of the DCN. However, this location
31 differs from slice to slice and is not related to the structures to be analyzed. A z-stack was acquired using
32 a 63x (NA1.4, Oil immersion) objective, applying a 2x zoom for each probe. The pinhole was set to 1 airy
33 unit and subsequently optimized for every detection channel to achieve an equal optical slice thickness
34 on all channels. XY voxel size was set to 0.14 um X 0.14 um; image digital resolution was set to 512x512

1 pixels. The z-stack step size was 0.32um and we took an average of 30 optical sections. We stained and
 2 analyzed 13 cerebellar sections (5 slices from D98 and 8 slices from H01) and 168 probes in total were
 3 sampled (90 from D98, 78 from H01). The fluorescence emitted by lipofuscin granules were recorded with
 4 excitation wavelength at 405nm and emission wavelength at 650-750nm. Details of antibodies, excitation
 5 wavelength and emission filters are listed in table 1.

6

1 st Antibody	2 rd Antibody	Excitation(nm)	Emission(nm)	Track number
Goat vGluT1	Donkey anti goat Alexa flour 488	488	505-550	1
Guinea pig vGluT2	Goat anti guinea pig Alexa flour 633	633	650-750	1
Mouse PCP2 Or mouse MAP2	Goat Anti mouse Alexa flour 405	405	420-480	2
Rabbit kv3.3	Goat anti rabbit cy3	543	560-615	2
None	None	405	650-750	3

7

8 *Table 1:*

9 Multichannel laser confocal microscopy parameters. Four different secondary antibodies were used with
 10 the corresponding primary antibodies. The fluorophores were excited at their optimal wavelength and
 11 the emissions were collected using different band pass or long pass filters. Lipofuscin was excited such as
 12 to obtain maximal difference between excitation and emission wave length, thereby dissociating it from
 13 the other fluorophores. Three tracks were used during the acquisition process to minimize channel
 14 interference.

1 We also determined tissue shrinkage in section thickness by taking four random positions within DCN
2 region for each slice and determining the upper and lower section borders by the staining signal for vGluT1
3 at a magnification of 20x (NA0.8, dry). Fifty-two probes were taken from 13 sections. The mean thickness
4 of the slices after mounting was 24.6um for D98 and 26um for H01, while the original sectioning thickness
5 was 40um and 50um, respectively. Classification of the macaca DCN was based on the description in an
6 earlier paper (Hamodeh et al. 2014).

7 *Data preprocessing and analysis*

8 Data were acquired as 8-bit format and saved in Zeiss lsm format. Stacks were then deconvoluted using
9 the iterative (n=10) "blind deconvolution" of AutoQuant X3 (Media Cybernetics, Bethesda, MD) with the
10 maximum likelihood estimation and constrained iteration. Following deconvolution, data were saved in
11 Autoquant to 8-bit lsm format.

12 *Lipofuscin masking and extraction of vGluTs boutons*

13 Lipofuscin has a broader excitation and emission spectrum than commercial fluorophores which are
14 designed with narrow spectra. We acquired the signals from our own fluorophores by regular microscopic
15 settings while simultaneously recording lipofuscin fluorescence signal in an additional channel and
16 subtracted the lipofuscin fluorescence during post-processing.

17 We performed surface reconstruction to get boundaries of lipofuscin granules using the Imaris software
18 (Bitplane). The lipofuscin surfaces were smoothed at 0.279um and the background was subtracted using
19 the Ridler and Calvard (R-C) algorithm [14]) to determine the best thresholding level for this channel. The
20 thresholding level was about 35/255. The reconstructed lipofuscin surfaces were subsequently used to
21 mask the vGluT1 and vGluT2 channel. The voxels inside the lipofuscin mask were set to 0, while the voxels
22 outside the lipofuscin mask remained unchanged. The background of the masked vGluT1 channel was
23 subtracted. The surface bounding of vGluT1 boutons was smoothed at 0.15um and the diameter of the
24 largest sphere fitting into the objects was taken at 0.5um. The masked vGluT2 channel was similarly
25 surface-rendered, except that we fitted a Gaussian filter (s.d.=0.3um) beforehand and used a user-defined
26 fixed threshold of 68/255. The threshold for masked vGluT1 channel was determined by the Ridler and
27 Calvard (R-C) algorithm and the resulting mean threshold was 20.1/255 for D98 and 26.2/255 for H01. We
28 used Gaussian filter and user-defined threshold for the masked vGluT2 channel to effectively exclude the
29 background and DCN neuron somata [6]. The surface reconstructed boutons were further filtered
30 according to size by excluding surfaces with less than 10 voxels [15].

31 *Shrinkage and density calculation*

32 The number of surface reconstructed boutons for each probe was exported and normalized to the
33 corrected volume of probe in question. First, we obtained the (uncorrected) section thickness by adding

1 the average diameter of the contours, 1.12 μm for vGluT1 and 1.19 μm for vGluT2 in order to account for
2 boutons being only partly contained within a section [16]. The uncorrected probe volume was then
3 obtained by multiplying the probe length (71.4 μm) and the probe width (71.4 μm) and the corrected depth
4 (varying from probe to probe). Tissue shrinkage affected the thickness of the section and was therefore
5 taken into consideration. To determine the extent of the shrinkage, four random positions were chosen
6 within the DCN region for each stain section. All the values were then averaged and the cerebellar sections
7 from D98 were shrunk to 24.6 μm thickness, while those of H01 were shrunk to a thickness of 26 μm , the
8 original sectioning thicknesses being 40 μm for D98 and 50 μm for H01. Finally, we divided the uncorrected
9 probe volume with 24.6/40 for D98 and 26/50 for H01 to obtain the corrected probe volumes.

10 *Calculating the co-labelling of vGluT1 and vGluT2 boutons*

11 The quantification of co-labelling of vGluT1 and 2 was performed by obtaining the intersection of the
12 surface boundaries of the two vGluT channels ($v\text{GluT1} \cap 2$). However, we could only perform channel
13 subtractions in Imaris. We therefore subtracted vGluT1 from the vGluT1-only channel. The vGluT1-only
14 channel was obtained for each probe by subtracting the vGluT2 channel from the original vGluT1 channel
15 for the rats and from the lipofuscin cleaned vGluT1 channel in the case of the monkey. The number of the
16 co-labelled boutons were divided by the vGluT1 bouton number or the vGluT2 bouton number to
17 ascertain the co-labelled percentage for vGluT1 boutons or vGluT2 boutons. The percentages were
18 compared between different nuclei and between the two species.

19 *Statistical analysis*

20 The vGluT1 and 2 density and volume values were checked for normal distribution and variance
21 homogeneity. Quantile-quantile plots (qqnorm in R, www.r-project.org) and Shapiro-tests (package lme4
22 in R) indicated normal distribution for vGluT1 and vGluT2 volume. Levene's tests (package Rcmdr in R)
23 indicated equal variance for vGluT1 and vGluT2 volume. The vGluT1 and vGluT2 density values were
24 power transformed by transformTukey (package rcompanion in R) to secure normal distribution and equal
25 variance. Since multiple data points were obtained in each subject [17], a linear mixed effect model was
26 used to accommodate the dependence of the data. The linear mixed effects model via restricted
27 maximum likelihood estimations were performed using lme4 package in R. The response was the
28 transformed density or non-transformed volume (for both vGluT1 and 2). The nuclei variance was
29 modelled as a fixed effect, while subject variance was modelled as a random effect in the model. We also
30 constructed a null model with only the random effect. We then compared the two models using a
31 likelihood ratio test to ascertain whether these two models differed significantly from each other. Post
32 hoc multiple comparisons (Tukey contrast) with Holm-Bonferroni correction were performed. The
33 significance level α was set to 0.05. We also plotted the data with intensity color-coded scatter plots using
34 matlab scripts [18].

1 Results

2 vGluT1+ and vGluT2+ staining patterns in the cerebellum

3 The vGluT2 immunofluorescence showed a puncta pattern organized in a linear beaded fashion in the
4 molecular layer (ML) and glomeruli-like pattern in the granule cells layer (GCL) of the cerebellar cortex
5 (small arrows in Fig. S1a). There are also granular structures in the Purkinje cells layer (PCL) as described
6 for lipofuscin in the literature (big arrow in Fig. S1a, [19]). Not surprisingly, these structures are obtained
7 again under our setting which is used for lipofuscin fluorescence (big arrow, Fig. S1b). The staining pattern
8 of vGluT2 after lipofuscin channel subtraction is consistent with our previous study in the rat using the
9 same antibody (Fig. S1c) [6]. Preabsorption of vGluT2 antibody with its corresponding peptide abolished
10 the vGluT2 signals in the cortex, pointing to the specificity of the vGluT2 antibody (Fig. S1d, e, f). Similarly,
11 the vGluT2 antibody is also specific in the DCN region (Fig. S1g-l). We also controlled the multiple staining
12 patterns in the cerebellar cortex (molecular layer) and DCN of the monkey. As anticipated, parallel fibers
13 were stained by vGluT1 only whereas climbing fiber presynapses were stained by vGluT2 only (Fig. 1a, b).
14 The vGluT1 and vGluT2 were separated from each other in the molecular layer, as the negative Pearson's
15 coefficient indicates (Fig. 1c). We also compared the staining of vGluT1 and 2 with the PCP2 staining in
16 the DCN and found them to be segregated as in the molecular layer (Fig. 1d, e). However, unlike in the
17 cortex, the vGluT1 and vGluT2 show some colocalization (Pearson's coefficient: 0.47). These colabelled
18 boutons may come from mossy fibers that express both vGluT1 and vGluT2 [5]. A comparison of labelling
19 intensity within a voxel confirmed the different patterns: in contrast to the DCN there was no above-
20 threshold intensity co-labelling of vGluT1 and 2 in the molecular layer (Fig. 1c, f). The spatial relationship
21 of the vGluT1 and 2 labelled puncta with their postsynaptic partner, the dendrites from DCN neurons, was
22 also examined in a quadruple staining environment. Most of the vGluT1 and 2 labelled puncta can be
23 observed around the dendrites (Fig. 1g, h). Again, the colocalization of vGluT1 and vGluT2 in the DCN can
24 be seen in this example (Fig. 1i).

25 Comparison of vGluT1+ and vGluT2+ boutons within DCN

26 To obtain the quantitative data of vGluT1+ and vGluT2+ bouton density and compare between nuclei, the
27 lipofuscin signal were first detected and eliminated from the vGluT1 and vGluT2 channels. First, we
28 verified the lipofuscin excitation and emission characteristics in unstained macaque cerebellar sections
29 (see supplementary material and Fig. S2). Then we validated our lipofuscin masking approach in the
30 vGluT1 and vGluT2 channels and this is summarized in the supplementary material (see also Fig S2-4).

31 The structures that are labelled by vGluT1, vGluT2 or both are shown in different nuclei (Fig. 2). Double
32 labelled structures can be found in all the different nuclei. However, the vGluT1+ boutons are sparser in
33 MN and AIN than in LN and PIN. Nevertheless, the vGluT2+ boutons are more similar between nuclei (Fig.
34 2a, c, e, g). The surface analysis allowed for a detailed visualization of vGluT1 and vGluT2-labelled

1 structures and quantification of the number and volume of the boutons as well as the co-labelled boutons
 2 (Fig. 2b, d, f, h).

	Threshold level	Dependent variables	df	Lambda	ICC	Chisq	p-value	Post-hoc test
vGluT1	R-C (23/255)	density	3	0.25	0.0526	29.38	$1.87 \cdot 10^{-6}$	MN&AIN< PIN&LN
	R-C (23/255)	volume	3	1	0.0338	35.69	$8.69 \cdot 10^{-8}$	MN<AIN; MN<PIN<LN
vGluT2	68/255	density	3	0.05	0.0526	7.85	0.049	n.s.
	68/255	volume	3	0.25	0.0284	9.47	0.023	PIN<LN

3 *Table 2:*

4 Post-hoc analysis (Tukey) of power transformed vGluT1+ and vGluT2+ bouton density and volume size.
 5 The df denotes degree of freedom; lambda denotes the power used for power transformation to ensure
 6 normality and equal variance and ICC is the intraclass correlation (indicates the amount of dependence
 7 in the data). P values were obtained by ANOVA. Post hoc test shows the comparisons which are
 8 statistically significant. P-values were adjusted by Holm-Bonferroni correction.

9 vGluT1+ and vGluT2+ bouton density and volume within DCN

10 We quantified the vGluTs bouton density in the different DCN. The vGluT1+ bouton density is higher in
 11 the PIN and LN, with $1.97 \cdot 10^6$ (SEM = $1.78 \cdot 10^5$) and $1.84 \cdot 10^6/\text{mm}^3$ (SEM = $4.96 \cdot 10^5$), and lower in
 12 AIN and MN, $1.21 \cdot 10^6$ (SEM = $3.04 \cdot 10^5$) and $1.12 \cdot 10^6/\text{mm}^3$ (SEM = $3.3 \cdot 10^5$) (ANOVA of mixed
 13 effect model, df: 3, Chi-square: 29.38, p: $1.87 \cdot 10^{-6}$). The vGluT2+ bouton density differed less intensely
 14 than the vGluT1 between subnuclei, although there was still a significant difference (ANOVA of mixed
 15 effect model, df: 3, Chi-square: 7.85, p: 0.049), mainly due to the lower density of vGluT2 in AIN. The mean
 16 density for vGluT2 was $1.7 \cdot 10^6/\text{mm}^3$ (SEM = $8.29 \cdot 10^4$) for the total DCN. The vGluT1 and 2+ bouton
 17 density data were power transformed to secure normal distribution and equal variance to satisfy the
 18 criterion for the statistic tests (Fig. S5a, c). The density and the volume of vGluT1+ and vGluT2+ boutons
 19 is shown for the four nuclei (Fig. 3a, b). The co-labelling of vGluT1 and vGluT2 is comparable in the AIN,
 20 PIN and LN, around 30%, with slightly lower values in MN (Fig. 3c). However, both the rat vGluT1 and
 21 vGluT2 co-labelling, which was obtained from our previous study, is significantly lower in the rat DCN than
 22 in the macaque DCN (Fig. 3d). The mean vGluT1+ and 2+ bouton volume is around $0.7 \mu\text{m}^3$ and $0.9 \mu\text{m}^3$,
 23 respectively (Fig. 3b). The vGluT1 volume was slightly larger in the AIN ($0.78 \mu\text{m}^3$) and LN ($0.8 \mu\text{m}^3$) than in
 24 the other DCN (MN: 0.61 and PIN: $0.70 \mu\text{m}^3$) and the vGluT2 volumes was larger in the LN ($0.97 \mu\text{m}^3$) than
 25 in the other DCN (PIN: 0.84 , AIN: 0.89 , MN: $0.86 \mu\text{m}^3$), albeit with a larger variability. A one-way ANOVA
 26 was used to test the variance by different nuclei classification and the results are summarized in Table 2.

1 We also scrutinized our reconstructed vGluT1 and 2 boutons for any cluster outliers, such as axonal
2 regions where the vGluTs are detected on their way to the presynaptic terminals [20]. These elongated
3 fragments would have a large ellipticity prolate value (close to 1) and a small diameter. Fig. 4 displays
4 density color-coded scatter plots of vGluT1 and 2 presynapse diameter versus the shape parameter
5 ellipticity prolate for the different DCN. Data show one large cluster with diameters larger than 0.5um and
6 ellipticity prolate larger than 0.2 and one small cluster with ellipticity prolate smaller than 0.2. Based on
7 these values they cannot be considered as axon fragments, because of their round shape. The number of
8 boutons in the small cluster in the MN, AIN, PIN and LN amounted to 2.9%, 3.8%, 4.1%, 3.8% for vGluT1
9 and 4.2%, 3.8%, 3.6%, 4.2% for vGluT2, respectively. These boutons may come from a distinct population,
10 e.g., the intrinsic DCN glutamatergic synapses.

11 Number of vGluT1+ and 2+ bouton per neuron

12 We calculated the mean bouton number per DCN neuron on the basis of our vGluT1 and vGluT2 labelled
13 boutons in the current study and the neuron density in our previous study [21, 22]. The vGluT1 and 2
14 bouton number per neuron is similar in rat and monkey. However, the vGluT1 bouton number per neuron
15 is significantly lower in the macaque LN/ dentate (Fig.5a). The total excitatory synaptic number per neuron
16 was calculated by subtracting the co-labelled vGluT1 bouton number per neuron from the total vGluT1
17 bouton number per neuron and adding the total vGluT2 bouton number per neuron (Fig. 5c, d). The total
18 bouton number per neuron in macaque DCN is lower than in the rat, except for the MN. Within the
19 macaque, PIN has the largest bouton number per neuron (Fig. 5c, d).

20 Discussion

21 In this study, we quantified vGluT1 and 2 in a region of a primate brain for the first time by also taking the
22 confounding contribution of lipofuscin autofluorescence into account. Our quantification shows that the
23 largest differences are observed between the DCN in the vGluT1 densities. This result is in agreement with
24 our previous observation finding similar differences in the rat vGluT1 densities [6]. This result also
25 confirms that our observation of variation in the dendritic length density in the macaque DCN [8, 23] are
26 accompanied by similar vGluT1 variations, i.e., regions with higher dendritic length densities show higher
27 vGluT1+ densities. In addition, our results also point to some important differences between the rat and
28 monkey LN/dentate, also confirming our previous dendritic quantifications showing hyposcaled dendrites
29 in the LN/dentate. We will first discuss the potential biases and limitations of our method and then return
30 to the interpretation of our results.

31 Our quantitative approach used systematic random sampling of series of multiple immunofluorescence-
32 stained sections. In total we acquired 168 probes with 3D- stacks covering the monkey DCN from two
33 monkeys. We adopted a new approach that involves recording an additional lipofuscin channel rather
34 than using chemicals to diminish the lipofuscin autofluorescence. This channel was used to mask the
35 lipofuscin fluorescence from the other fluorescence channels. Although the 405nm wavelength laser used

1 to excite the lipofuscins had the potential to bleach other fluorophores, we did not observe any indications
2 that this was the case at our laser excitation powers. We generated surfaces from the lipofuscin
3 fluorescence and used these to mask the other channels. When the lipofuscin regions are masked, their
4 intensities change to zero. Therefore, if the structure of interest is also located in the cytoplasm, they
5 could be affected. In our case, this did not occur since the glutamate transporters we quantified were
6 located in the presynapses.

7 One of our main finding is that the density of vGluT1 labelled boutons is higher in phylogenetically newer
8 parts of DCN, the LN/dentate and PIN, thus confirming our previous findings in the rat [6]. This is also in
9 agreement with our previous result of higher dendritic length density in these parts of the DCN.
10 Nevertheless, the comparison of the vGluT1 densities showed that the monkey DCN ($1.5 \cdot 10^6$ vs.
11 $6.1 \cdot 10^6$) had a lower overall synaptic density of about 25% of the rat values [6]. This is comparable to
12 the reduction in neuronal density (8640 vs. 25300) to 34% of the rat densities and shows that the overall
13 vGluT1 synapses per neuron remain comparable. A comparison of the dendritic length density [22] of
14 monkeys vs. rats (51.5 vs. 39.8m/mm³), shows a lower reduction to 77% of the rat values and would
15 point to a general reduction in the number of vGluT synapses per dendritic length. Excitatory synapses to
16 the DCN neurons largely originate from the precerebellar nuclei. The largest of these nuclei is the basilar
17 pontine nuclei which increases considerably in size and neuron number in primates. Therefore, we would
18 have anticipated a higher number of vGluT synapses per neuron in the LN/dentate and PIN.

19 [Comparable number of excitatory synapses per neuron in rat and monkey DCN](#)

20 One explanation of the comparable values of excitatory synapses per neuron could be due to the modular
21 organization of the cerebellum with similar number of units/neurons per module. However, other,
22 potentially confounding factors may have led to a reduction of vGluT immunostaining in the monkey. The
23 antibodies we used were optimized to stain the rodent's vGluT c-terminal (unspecified peptide length for
24 vGluT1 and amino acids 510-582 for vGluT2). A comparison of the amino acid sequence of the two
25 transporters between rat and macaca mulatta shows that vGluT1 has an essentially conserved sequence,
26 whereas the vGluT2 shows multiple amino acid changes in the last 72 amino acids. It is therefore possible
27 that the vGluT2 immunostaining in the monkey tissue could be altered, which would also explain the
28 higher threshold used for vGluT2 compared to the rat. However, a comparison of the staining pattern
29 within the molecular layer did not show colocalization at above-threshold intensities for the vGluT2+ only
30 climbing fibers and the vGluT1+ only parallel fibers. Our calculation of the individual excitatory inputs per
31 neuron were based on different individuals and this may have introduced additional variability in our
32 results. We used systematic unbiased sampling in both cases and tried to minimize the influence of such
33 bias. Finally, our two monkeys, aged 13 and 18 years, may have already shown signs of age-related
34 synapse elimination. As anticipated, our quantification of the lipofuscin did show a higher lipofuscin
35 density in the older monkey [24] However, we did not observe systematically lower vGluT densities in the
36 older monkey (D98 vs. H01: $1.5 \cdot 10^6$ vs. $2.3 \cdot 10^6$ /mm³ for vGluT1 and $1.8 \cdot 10^6$ vs. $1.2 \cdot 10^6$ /mm³

1 for vGluT2). In summary, our data could point to the importance of a rather constant number of excitatory
2 synapses per DCN neuron, reflecting a limited number of input units per DCN neuron.

3 Increased vGluT1 and 2 co-labelling in the monkey DCN

4 One unexpected finding of our study is that the monkey DCN contain a higher percentage of vGluT1 and
5 2 co-labelled presynapses than those of the rat DCN (30 vs. 15%). This is probably due to the fact that the
6 density of vGluT2 in the monkey is higher than in the rat. The cerebellum is one of the few brain regions
7 that shows the presence of both kinds of vGluTs (in climbing and mossy fibers), as well as presynapses
8 with both kinds of vGluTs in a subset of mossy fibers. Developmental studies have shown that, during the
9 early stages of development, vGluT2 synapses change to vGluT1 following the switch of vGluT2 mRNA
10 expression to vGluT1 mRNA expression in the neuron somata [25]. This suggests that a change occurs at
11 the transcription and translation level of protein synthesis. This could thus imply that the mossy fibers
12 retain a status comparable to that of the early stages of development, allowing for prolonged modification
13 from vGluT2 to vGluT1. A different scenario emerges if we look at a recent learning/plasticity study in the
14 DCN. The study by Boele and colleagues showed an increase in basilar pontine nuclei vGluT2 mossy fiber
15 presynapses in the DCN following Pavlovian eyeblink conditioning [1]. So far, it remains unclear whether
16 this kind of learning in the DCN requires the sprouting and formation of new vGluT2 synapses, or whether
17 it is achieved by an increase in vGluT2 levels in vGluT1 mossy fiber collaterals. The latter has not been
18 described so far and therefore currently appears to be the less likely scenario.

19 Hyposcaling of vGluT1+ inputs to the primates LN/dentate

20 A further new finding of our study is that there is a lower number of vGluT1+ excitatory synapses per
21 neuron in the LN/dentate of the rhesus monkey compared to the rat's LN/dentate. This result tallies well
22 with the lower dendritic length per neuron that we already reported in the monkey LN/dentate [22] and
23 lends further support to our model of hyposcaled dendrites that underlie the special architecture of the
24 LN/dentate. The hyposcaled dendritic arbors [22] and vGluT1+ inputs (this study) could allow for an
25 increase in the number of independent/segregated parasagittal strips in the cerebellar hemispheres
26 connected to the LN/dentate, which would confirm a recent prediction [26]. A theory proposed by van
27 Essen (1997) on how and why structures in the central nervous system tend to fold was based on the
28 amount of mechanical tension that arises from the connectivity pattern of a given brain region [27]. If we
29 assume that the hyposcaled dendrites with smaller region of influence and with less excitatory synaptic
30 connections would lead to less tightly connected tissue, then these less tightly connected regions would
31 lead to a reduction of tension, which in turn would lead to some indentation and folding at these sites
32 during the ontogenetic and phylogenetic volume increase of the nucleus. These changes could then first
33 lead to the emergence of a torus-like or cup-shaped nucleus, as indeed the rhesus monkey LN/dentate
34 exhibits [28], whereas, in the nucleus with more similar connectivity tension would be basically the same
35 all across the nucleus and would help in preserving a globose structure.

1 References

- 2 [1] H.J. Boele, S.K. Koekkoek, C.I. De Zeeuw, T.J. Ruigrok, Axonal sprouting and formation of terminals in
3 the adult cerebellum during associative motor learning, *J Neurosci*, 33 (2013) 17897-17907.
- 4 [2] K.H. Lee, P.J. Mathews, A.M. Reeves, K.Y. Choe, S.A. Jami, R.E. Serrano, T.S. Otis, Circuit mechanisms
5 underlying motor memory formation in the cerebellum, *Neuron*, 86 (2015) 529-540.
- 6 [3] S. Hisano, K. Sawada, M. Kawano, M. Kanemoto, G. Xiong, K. Mogi, H. Sakata-Haga, J. Takeda, Y.
7 Fukui, H. Nogami, Expression of inorganic phosphate/vesicular glutamate transporters (BNPI/VGLUT1
8 and DNPI/VGLUT2) in the cerebellum and precerebellar nuclei of the rat, *Brain research. Molecular brain
9 research*, 107 (2002) 23-31.
- 10 [4] H. Hioki, F. Fujiyama, K. Taki, R. Tomioka, T. Furuta, N. Tamamaki, T. Kaneko, Differential distribution
11 of vesicular glutamate transporters in the rat cerebellar cortex, *Neuroscience*, 117 (2003) 1-6.
- 12 [5] J.L. Boulland, T. Qureshi, R.P. Seal, A. Rafiki, V. Gundersen, L.H. Bergersen, R.T. Fremeau, Jr., R.H.
13 Edwards, J. Storm-Mathisen, F.A. Chaudhry, Expression of the vesicular glutamate transporters during
14 development indicates the widespread corelease of multiple neurotransmitters, *J Comp Neurol*, 480
15 (2004) 264-280.
- 16 [6] H. Mao, S. Hamodeh, F. Sultan, Quantitative comparison of vesicular glutamate transporters in rat
17 deep cerebellar nuclei, *Neuroscience*, DOI 10.1016/j.neuroscience.2018.02.020(2018).
- 18 [7] R.T. Fremeau Jr, S. Voglmaier, R.P. Seal, R.H. Edwards, VGLUTs define subsets of excitatory neurons
19 and suggest novel roles for glutamate, *Trends in Neurosciences*, 27 (2004) 98-103.
- 20 [8] S. Hamodeh, A. Bozkurt, H. Mao, F. Sultan, Uncovering specific changes in network wiring underlying
21 the primate cerebrotype, *Brain structure & function*, 222 (2017) 3255-3266.
- 22 [9] V. Garcia-Marin, T.H. Ahmed, Y.C. Afzal, M.J. Hawken, Distribution of vesicular glutamate transporter
23 2 (VGLUT2) in the primary visual cortex of the macaque and human, *The Journal of comparative
24 neurology*, 521 (2013) 130-151.
- 25 [10] A. Terman, U.T. Brunk, Lipofuscin, *The international journal of biochemistry & cell biology*, 36
26 (2004) 1400-1404.
- 27 [11] J.A. Steinkamp, C.C. Stewart, Dual-laser, differential fluorescence correction method for reducing
28 cellular background autofluorescence, *Cytometry*, 7 (1986) 566-574.
- 29 [12] M. Roederer, R.F. Murphy, Cell-by-cell autofluorescence correction for low signal-to-noise systems:
30 application to epidermal growth factor endocytosis by 3T3 fibroblasts, *Cytometry*, 7 (1986) 558-565.
- 31 [13] N. Billinton, A.W. Knight, Seeing the wood through the trees: a review of techniques for
32 distinguishing green fluorescent protein from endogenous autofluorescence, *Analytical biochemistry*,
33 291 (2001) 175-197.
- 34 [14] T.W. Ridler, S. Calvard, Picture Thresholding Using an Iterative Selection Method, *Ieee Transactions
35 on Systems Man and Cybernetics*, 8 (1978) 630-632.
- 36 [15] C.L. Haass-Koffler, M. Naeemuddin, S.E. Bartlett, An analytical tool that quantifies cellular
37 morphology changes from three-dimensional fluorescence images, *Journal of visualized experiments :*
38 *JoVE*, DOI 10.3791/4233(2012) e4233.
- 39 [16] V. Braitenberg, A. Schüz, *Cortex: Statistics and Geometry of Neuronal Connectivity*, Springer-Verlag,
40 Berlin Heidelberg New York, 1998.
- 41 [17] E. Aarts, M. Verhage, J.V. Veenvliet, C.V. Dolan, S. van der Sluis, A solution to dependency: using
42 multilevel analysis to accommodate nested data, *Nature neuroscience*, 17 (2014) 491-496.
- 43 [18] P.H. Eilers, J.J. Goeman, Enhancing scatterplots with smoothed densities, *Bioinformatics*, 20 (2004)
44 623-628.
- 45 [19] K.R. Brizzee, J.M. Ordy, B. Kaack, Early appearance and regional differences in intraneuronal and
46 extraneuronal lipofuscin accumulation with age in the brain of a nonhuman primate (*Macaca mulatta*),
47 *Journal of gerontology*, 29 (1974) 366-381.

- 1 [20] H. Mao, S. Hamodeh, F. Sultan, Quantitative Comparison Of Vesicular Glutamate Transporters in rat
2 Deep Cerebellar Nuclei, *Neuroscience*, 376 (2018) 152-161.
- 3 [21] S. Hamodeh, J. Baizer, I. Sugihara, F. Sultan, Systematic analysis of neuronal wiring of the rodent
4 deep cerebellar nuclei reveals differences reflecting adaptations at the neuronal circuit and internuclear
5 level, *The Journal of comparative neurology*, DOI 10.1002/cne.23545(2014).
- 6 [22] S. Hamodeh, A. Bozkurt, H. Mao, F. Sultan, Uncovering specific changes in network wiring
7 underlying the primate cerebrotype, *Brain structure & function*, DOI 10.1007/s00429-017-1402-6(2017).
- 8 [23] S. Hamodeh, I. Sugihara, J. Baizer, F. Sultan, Systematic analysis of neuronal wiring of the rodent
9 deep cerebellar nuclei reveals differences reflecting adaptations at the neuronal circuit and internuclear
10 level, *J Comp Neurol*, 522 (2014) 2481-2497.
- 11 [24] E.P. Gilissen, M. Dhenain, J.M. Allman, 27 - Brain Aging in Strepsirhine Primates, in: P.R. Hof, C.V.
12 Mobbs (Eds.) *Functional Neurobiology of Aging*, Academic Press, San Diego, 2001, pp. 421-433.
- 13 [25] T. Miyazaki, M. Fukaya, H. Shimizu, M. Watanabe, Subtype switching of vesicular glutamate
14 transporters at parallel fibre-Purkinje cell synapses in developing mouse cerebellum, *The European*
15 *journal of neuroscience*, 17 (2003) 2563-2572.
- 16 [26] H. Jorntell, Cerebellar physiology: links between microcircuitry properties and sensorimotor
17 functions, *The Journal of physiology*, 595 (2017) 11-27.
- 18 [27] D.C. Van Essen, A tension-based theory of morphogenesis and compact wiring in the central
19 nervous system, *Nature*, 385 (1997) 313-318.
- 20 [28] F. Sultan, S. Hamodeh, J.S. Baizer, The human dentate nucleus: a complex shape untangled,
21 *Neuroscience*, 167 (2010) 965-968.

22 **CONFLICT OF INTEREST STATEMENT**

23 The authors have no conflicts of interest.

24 **ROLE OF AUTHORS**

25 SH sectioned the monkey cerebellum and AS assisted with the LSM multi-channel setup and lambda mode
26 scanning. HM conducted the staining and acquired the data. HM and FS analyzed the data and prepared
27 the manuscript. FS designed the project and was responsible for securing funding.

28 **Figure legends**

29 **Fig. 1** vGluT1+ and vGluT2+ staining patterns in the cerebellum. The staining pattern of vGluT1, vGluT2
30 and MAP2 in the cerebellar molecular layer is shown in (a) and (b). The parallel fibers are detected by
31 vGluT1 antibody (red), while the climbing fiber terminals are detected by vGluT2 antibody (green). The
32 dendrites of Purkinje cells are labelled by MAP2 (Microtubule-associated protein 2, blue) (a, b). The
33 colocalization analysis of vGluT1 and vGluT2 is shown in (c), with Pearson's coefficient (PC) -0.17. The
34 vGluT1, vGluT2 and PCP2 staining pattern in DCN is shown in (d) and (e). The Purkinje cell axons are
35 labelled by PCP2 in blue. The excitatory presynapses are labelled by vGluT1 (red) or vGluT2 (green) or
36 both. The colocalization analysis of the vGluT1 and vGluT2 in DCN is shown in (f) and yields a PC of 0.47.
37 Another example from the DCN is shown in (g) and (h). The vGluT1, vGluT2 and MAP2 staining shows that
38 the majority of excitatory boutons labelled by vGluT1 (red) or vGluT2 (green) contact the DCN dendrites
39 labelled by MAP2 (blue) (g and h). The pearson's coefficient of 0.69 indicates colocalization of vGluT1 and
40 vGluT2 in the DCN (i). Scale bar in (h) is 10um and applies also to images (a, b, d, e, g)

1 **Fig. 2** Examples of vGluT1 and 2 staining in the monkey DCN. Comparison of original microscopic views (a,
2 c, e, g) and surface-rendered views (b, d, f, h) from vGluT1 and vGluT2 stained boutons in different nuclei.
3 The Ridler-Calvard algorithm was used for the red channel, vGluT1, while the thresholding for vGluT2 was
4 user defined at 68/255. Scale bar = 10um in (h) applies to all other images as well.

5 **Fig. 3** Boxplots of the density, volume and co-labelling of vGluT1- and vGluT2-stained boutons in different
6 nuclei. (a-c) shows the results from the rhesus monkey DCN. (a) shows the density of vGluT1 and vGluT2
7 profiles. The vGluT1 density is highest in LN/dentate and PIN and lowest in MN and AIN ($p= 1.87 \cdot 10^{-6}$).
8 The vGluT2 density is comparable between nuclei ($p= 0.049$) except for a lower density in the AIN. (b)
9 Shows the volumes of vGluT1 and 2 profiles. The mean vGluT1 and vGluT2 bouton volumes are $0.7 \mu\text{m}^3$
10 and $0.9 \mu\text{m}^3$, respectively. (c) Co-labelled percentage of vGluT1 and vGluT2 is compared in different nuclei
11 of the monkey, with the average value of 30% for vGluT1 and 31% for vGluT2. (d) The co-labelling of
12 vGluT1 and vGluT2 is significantly lower in the rat (around 15%) than in the monkey.

13 **Fig. 4** Intensity color coded scatter plots. Scatter plots of two shape parameters (ellipticity prolate and
14 diameter) and their relation to the profile diameters for vGluT1 (a–d) and vGluT2 (e–h). Plotted are the
15 values for the different DCN subnuclei. The overall pattern is very similar, with one large cluster
16 encompassing most of the profiles and one smaller cluster (to the lower left of the larger cluster) showing
17 special subpopulations. The colabelled boutons show similar shapes between nuclei (i-l). The color coding
18 indicates the intensity of the scatter plot. Red represents higher and blue represents lower intensities.

19 **Fig. 5** Bouton number per individual DCN neuron. The vGluT1 and vGluT2 labelled boutons are normalized
20 by the neuronal density and compared in the rat and monkey DCN. The vGluT1 bouton number per neuron
21 is similar in the rat and monkey, except in the LN in which the (95% confidence intervals) error bars do
22 not overlap (a). The vGluT2 labelled bouton per neuron is similar in the rat and monkey DCN (b). The sum
23 of vGluT1 and vGluT2 (uncorrected total) bouton number per neuron (c) was adjusted to remove the twice
24 counted double labelled boutons. This was done by subtracting the co-labelled vGluT1 bouton number
25 per neuron from the total vGluT1 bouton number per neuron and then adding the total vGluT2 bouton
26 number per neuron (d, “corrected”). In the monkey, the total bouton number per neuron is highest in the
27 PIN, with a value of 427 boutons per neuron.

28

29 [Supplementary material](#)

30 **Fig. S1** Preabsorption test for vGluT2. In the cerebellar cortex the original vGluT2 channel containing
31 lipofuscin not only detects the beaded-like climbing fiber terminals in the molecular layer (small arrow),
32 the glomeruli structures in the granule layer (small arrow) but also the lipofuscin signals from Purkinje
33 cells layer (big arrow) (a). The autofluorescence in the cerebellar cortex is obtained in a separate channel
34 using excitation at 405nm and emission filters at 650-750nm (b). After channel subtraction, the structures
35 detected by vGluT2 antibody is confined to the molecular and granule layer (c). In contrast, after applying
36 the vGluT2 antibody and the peptide antigen mixture we only detect the autofluorescence in the Purkinje
37 cell layer (d and e). No signal was left after subtracting lipofuscin channel from the vGluT2 channel (f). In
38 the DCN, bouton-like structures and big granules were detected in the vGluT2 channel (g). The

1 autofluorescence was also present in DCN (h). Only puncta structures were left after channel subtraction
2 (i). The preabsorption test also abolished the vGluT2 staining in the DCN (j-l). Scale bar in (f): 20um and
3 applies also to (a-e). Scale bar in (l): 10um and applies to (g-k).

4

5 Results of masking lipofuscin in vGluT1 and vGluT2 channels

6 We scanned unstained macaque cerebellar sections by exciting the tissue at 405nm and by collecting the
7 emission from 650-750nm and detected fluorescent granule-like structures (Fig. S2a). When the
8 specimens were scanned in lambda mode, these granule-like structures showed a broad emission spectral
9 range from 450 to 750nm and peaking at around 530nm. This indicates that these structures are lipofuscin
10 (Fig. S2b). Since the lipofuscin has not only a broad emission spectrum but also broad excitation spectra,
11 granule-like structures were also obtained under the excitation of 633nm laser (Fig. S2c). Again these
12 structures have broad emission spectra under lambda mode (Fig. S2d). However, independent of the
13 granules' location (inside the neuronal soma ROI 3, Fig. S2a or outside the soma ROI 1,2 and 4, Fig. S2a),
14 they share the same fluorescence emission properties, thus further endorsing the compositional
15 homogeneity of these structures. By contrast, the intensity of tissue background fluorescence was lower
16 than the lipofuscin fluorescence and dropped to baseline at longer wavelengths (ROI 5, Fig. S2a and b, ROI
17 2, Fig. S2c and d). The lipofuscin fluorescence can also be well segregated from the tissue background
18 fluorescence from the emission range of 650-750nm (light green rectangle in Fig. S2b and d). We then
19 tested whether the lipofuscin fluorescence can be segregated from our staining. Alexa 405 was used to
20 detect Purkinje cell axons in our quadruple staining with optimal excitation at 405nm. The emission
21 spectrum of the Alexa 405 and lipofuscin differed considerably. The emission range was 405-600nm with
22 the peak around 450nm for Alexa 405. The Alexa 405 emission range was much narrower than that of
23 lipofuscin, and most importantly, there was no emission from 650-750nm, indicating that exciting the
24 lipofuscin at 405nm and obtaining its emission within the range 650-750nm would result in a pure signal
25 (Fig. S2e-f). This configuration ensured no bleed-through of fluorescence emission of the rest of the
26 fluorochromes into the lipofuscin emission signal. In a next step, we needed to remove the lipofuscin
27 staining from the vGluT1 and vGluT2 signal. We used the lipofuscin channel to produce a mask (Fig. S3a),
28 by creating surfaces fitted to the lipofuscin granules (Fig. S3b). The quantification of lipofuscin volume in
29 DCN from two monkeys was also obtained on the basis of the constructed surfaces. The amount of
30 lipofuscin in the DCN of the 18-year-old D98 is about two-fold that of the 13-year-old H01. However, the
31 amount of lipofuscin in the subnuclei does not differ (Fig. S4). The lipofuscin mask was subtracted from
32 the vGluT1 and vGluT2 channels and we obtained the masked vGluT1 and vGluT2 channels, respectively
33 (Fig. S3c, e). Finally, the lipofuscin-removed vGluT1 and vGluT2 channels were surface-rendered for
34 quantification (Fig. S3d, f).

1

2 **Fig. S2** Lipofuscin fluorescence detection and its spectral characteristics. The lipofuscin fluorescence in
3 the unstained DCN was present both in the neuronal cytoplasm (ROI 3) and outside the neuron (ROI 1, 2,
4 and 4) under excitation of 405nm (a). The emission spectrum of each region of interest (ROI) selected is
5 shown in (b). The ROI 5 was tissue background. The spectra of ROI 1-4 were widely spread from 411nm to
6 752nm, albeit with varying intensities. The maximum emission intensity under 405nm excitation was
7 around 530nm (b). The unstained section can also be excited at 633nm (c) and the spectra are shown in
8 (d). The quadruple stained rhesus monkey section was scanned under 405nm excitation in lambda mode
9 (e). The fluorescence spectra from PCP2/Alexa 405 and lipofuscin differ considerably: ROI of 4 and 5 are
10 from PCP2 stained structures and ROI 1-3 and 7-8 are from lipofuscin (e, f). In the emission region of 650-
11 750nm, the PCP2/Alexa 405 was reduced to baseline, while lipofuscin still emits a high-intensity signal (f).
12 The light green columns in (b) and (d) indicate the emission range 650-750nm. The ROI 6 was tissue
13 background. Scale bar in (a), (c) and (e) is 10um.

14

15 **Fig. S3** Workflow to remove lipofuscin autofluorescence (AF) from vGluT1 and vGluT2 channels. The
16 lipofuscin channel signal (a) was surface-rendered in Imaris (b). This mask was then used to subtract from
17 the original vGluT1 and vGluT2 channels (c, e) to obtain the masked vGluT1 and vGluT2 channel (d, f).
18 Scale bar in (f) and in all other images is 10um.

19

20 **Fig. S4** Lipofuscin quantification in DCN. The volume of the lipofuscin surfaces was obtained and compared
21 in different nuclei of two monkeys (D98 (a) and H01 (b)). The lipofuscin volume fraction was higher in the
22 older monkey (D98 i.e., a). Lipofuscin density did not differ significantly between the DCN (ANOVA, $p=0.28$
23 for D98, $p=0.27$ for H01). Examples of microscopic images with lipofuscin (red) is shown in (c) and (d) with
24 vGluT1 channel (green).

25

26 **Fig. S5** Quantile-quantile plots of the power transformed data (a–d). The Shapiro p-values in (a) (c) and (d)
27 are larger than 0.05, indicating that the transformed vGluT1 and 2 density and vGluT2 volume are derived
28 from normally distributed populations. The vGluT1+ bouton volume data was not power transformed (b)

29

30

Figure 1

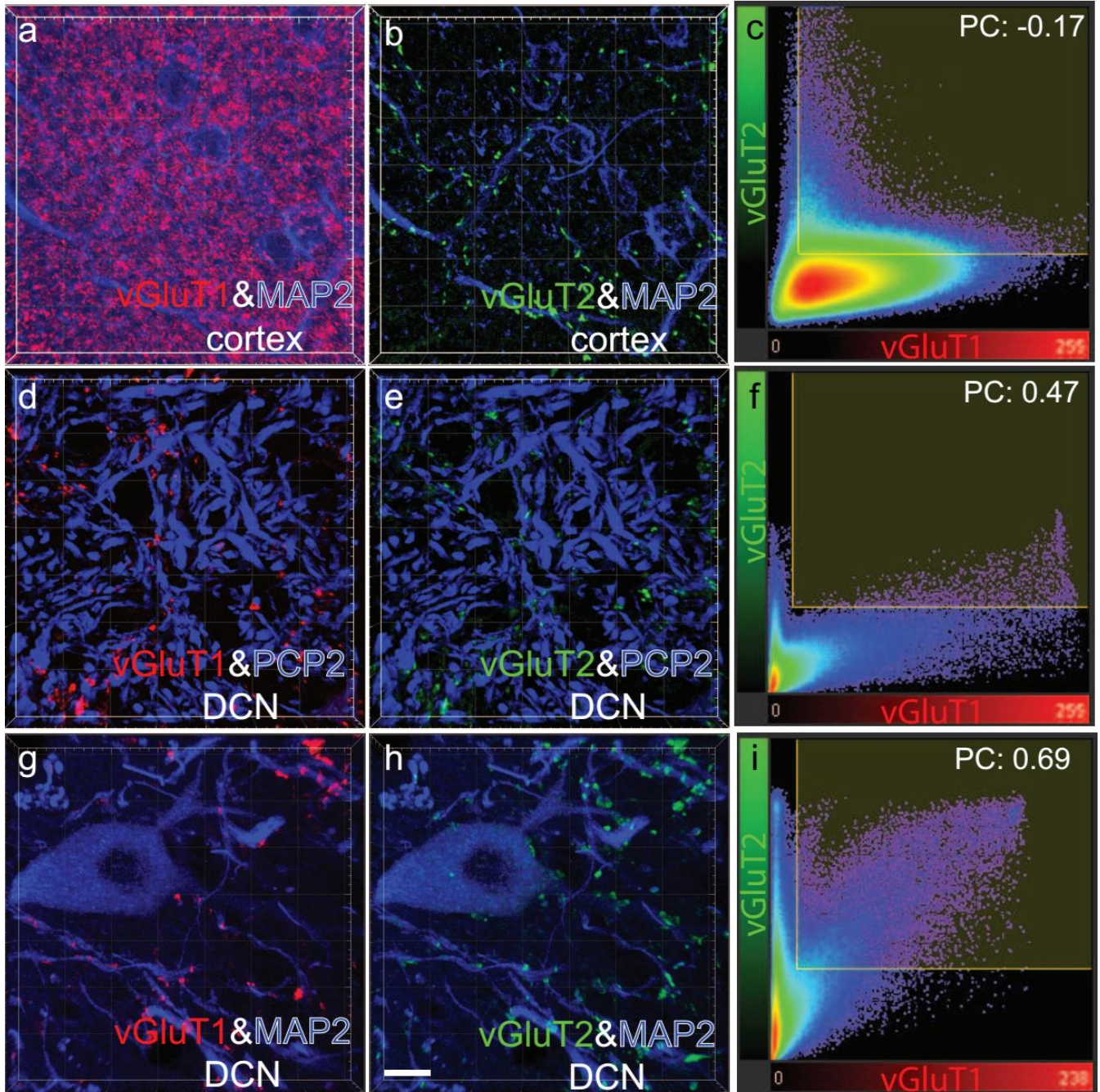


Figure 2

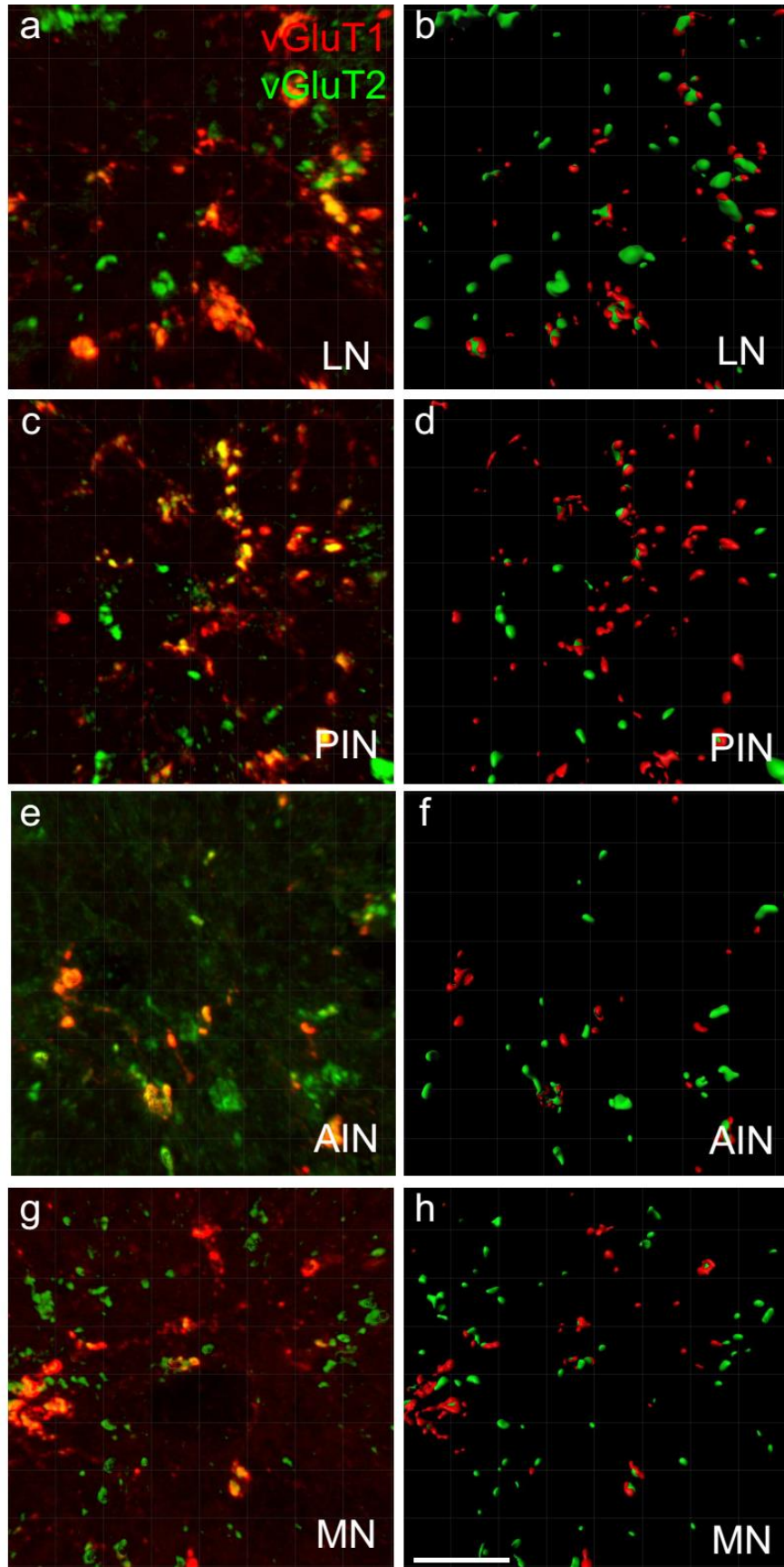


Figure 3

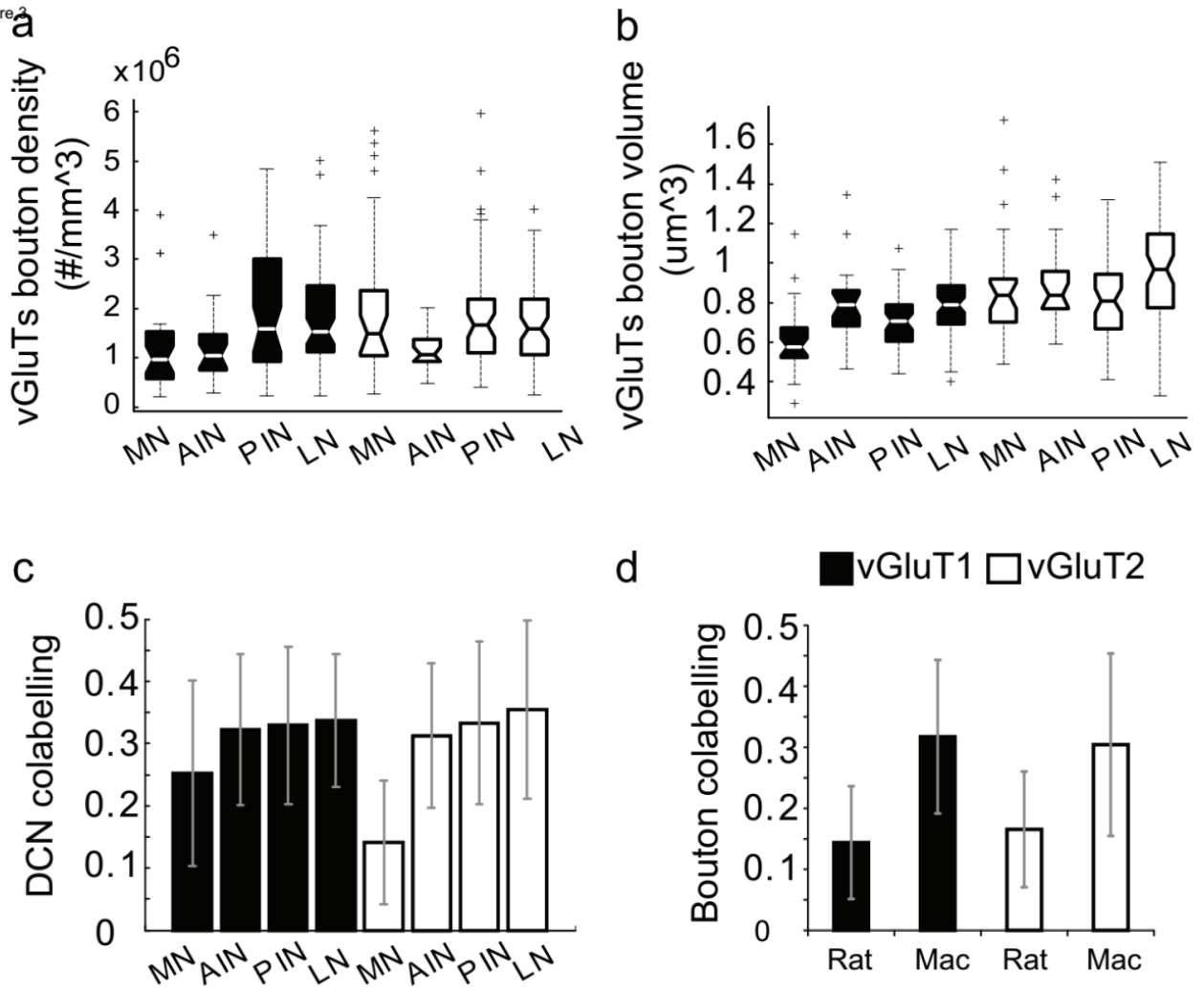
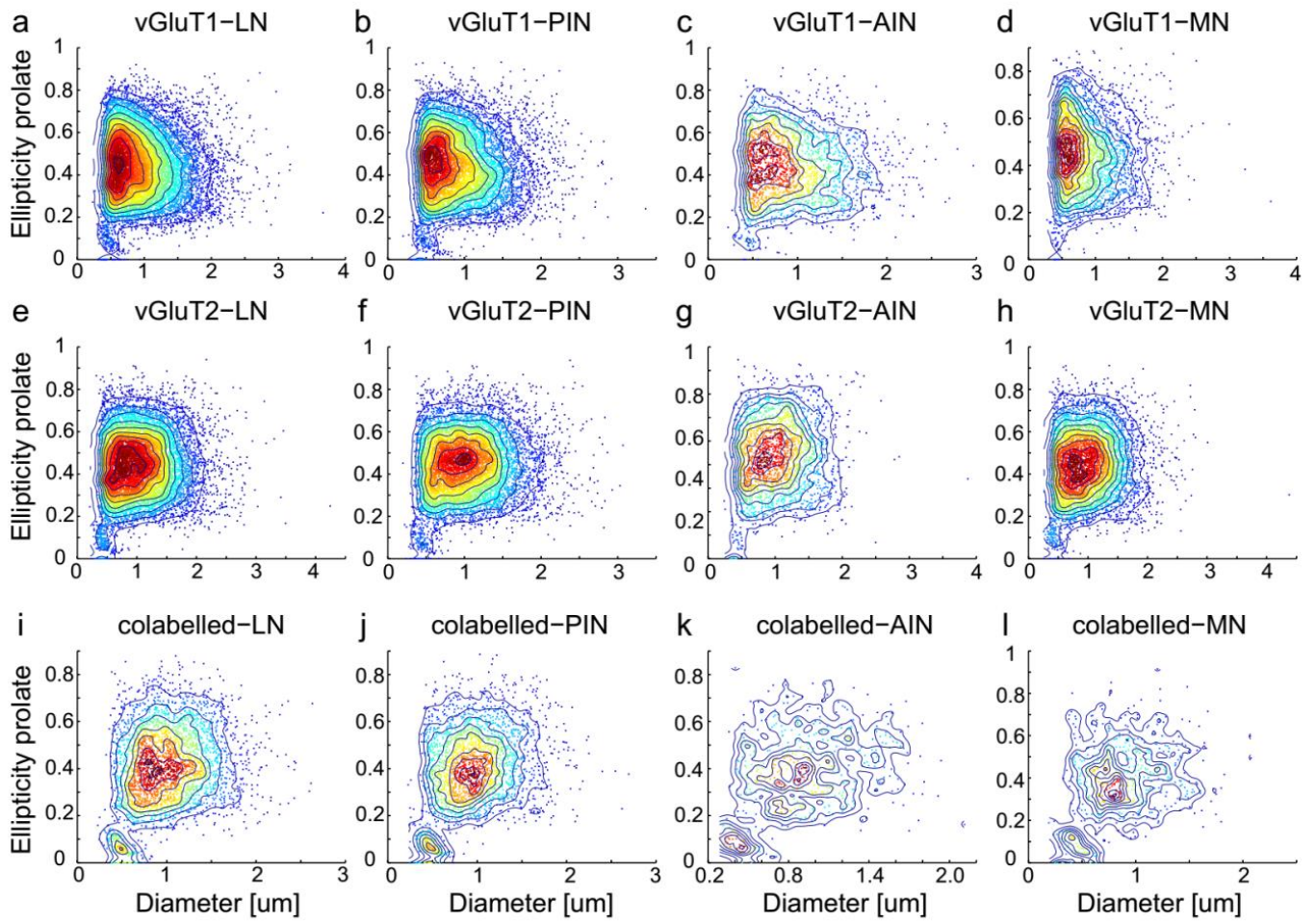


Figure 4



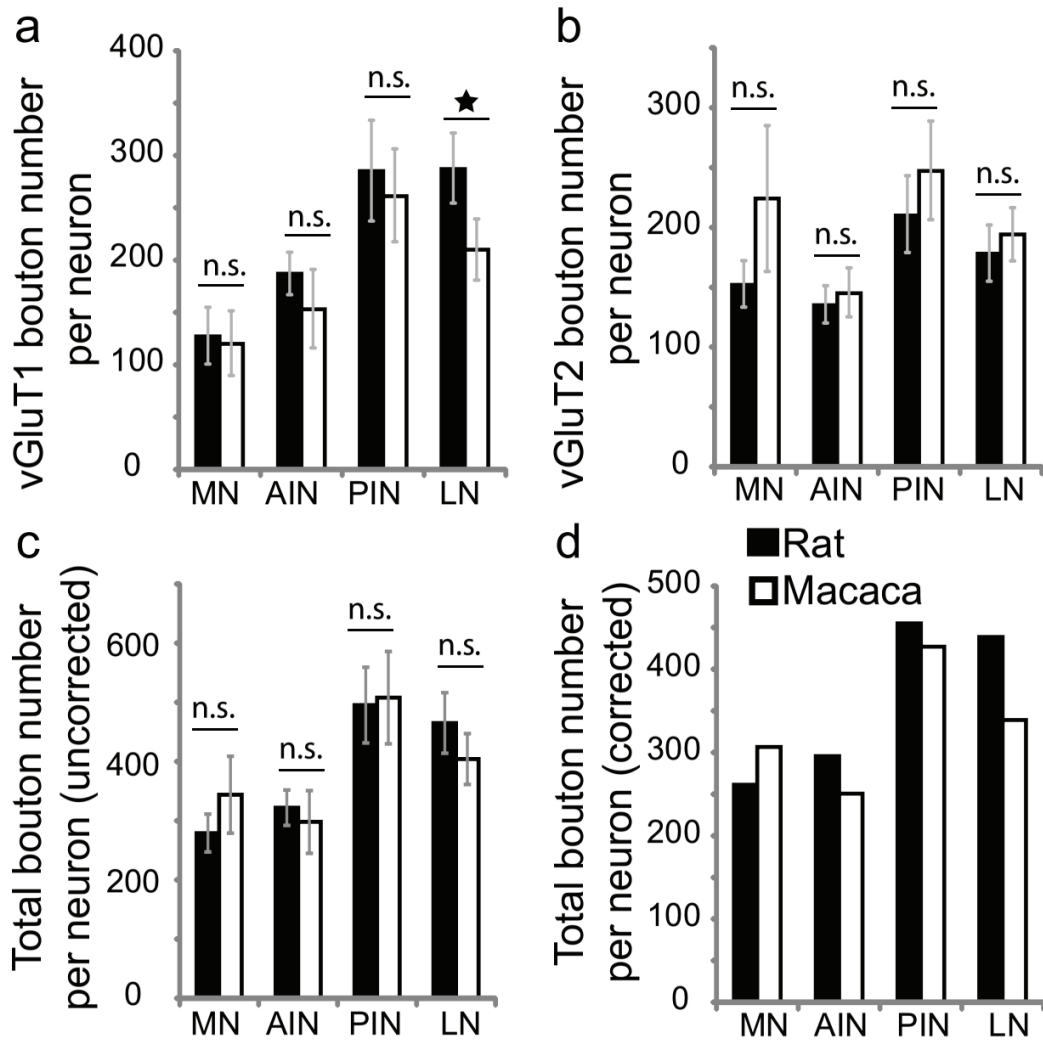
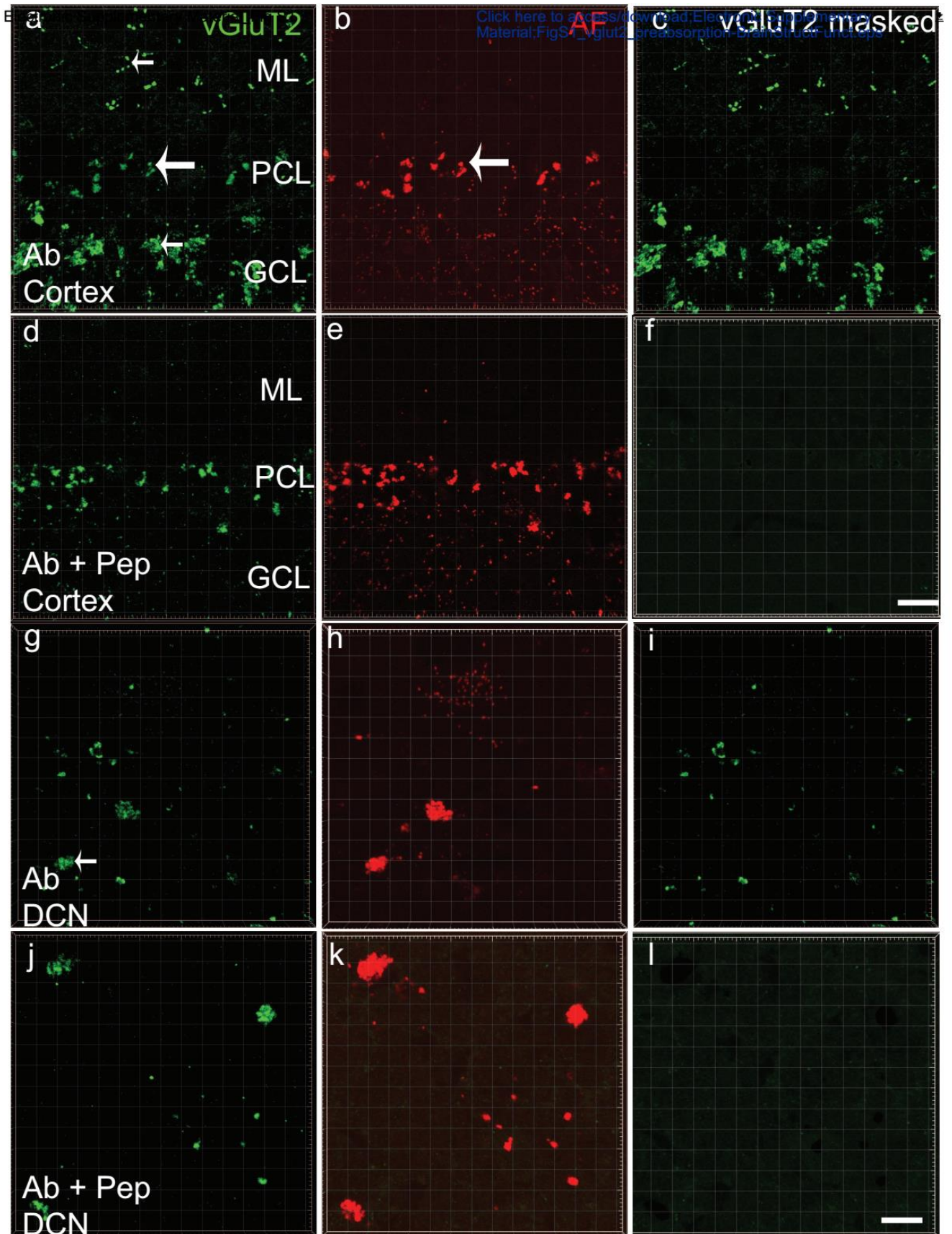


Figure 5



Results of masking lipofuscin in vGluT1 and vGluT2 channels

We scanned unstained macaque cerebellar sections by exciting the tissue at 405nm and by collecting the emission from 650-750nm and detected fluorescent granule-like structures (Fig. S2a). When the specimens were scanned in lambda mode, these granule-like structures showed a broad emission spectral range from 450 to 750nm and peaking at around 530nm. This indicates that these structures are lipofuscin (Fig. S2b). Since the lipofuscin has not only a broad emission spectrum but also broad excitation spectra, granule-like structures were also obtained under the excitation of 633nm laser (Fig. S2c). Again these structures have broad emission spectra under lambda mode (Fig. S2d). However, independent of the granules' location (inside the neuronal soma ROI 3, Fig. S2a or outside the soma ROI 1,2 and 4, Fig. S2a), they share the same fluorescence emission properties, thus further endorsing the compositional homogeneity of these structures. By contrast, the intensity of tissue background fluorescence was lower than the lipofuscin fluorescence and dropped to baseline at longer wavelengths (ROI 5, Fig. S2a and b, ROI 2, Fig. S2c and d). The lipofuscin fluorescence can also be well segregated from the tissue background fluorescence from the emission range of 650-750nm (light green rectangle in Fig. S2b and d). We then tested whether the lipofuscin fluorescence can be segregated from our staining. Alexa 405 was used to detect Purkinje cell axons in our quadruple staining with optimal excitation at 405nm. The emission spectrum of the Alexa 405 and lipofuscin differed considerably. The emission range was 405-600nm with the peak around 450nm for Alexa 405. The Alexa 405 emission range was much narrower than that of lipofuscin, and most importantly, there was no emission from 650-750nm, indicating that exciting the lipofuscin at 405nm and obtaining its emission within the range 650-750nm would result in a pure signal (Fig. S2e-f). This configuration ensured no bleed-through of fluorescence emission of the rest of the fluorochromes into the lipofuscin emission signal. In a next step, we needed to remove the lipofuscin staining from the vGluT1 and vGluT2 signal. We used the lipofuscin channel to produce a mask (Fig. S3a), by creating surfaces fitted to the lipofuscin granules (Fig. S3b). The quantification of lipofuscin volume in DCN from two monkeys was also obtained on the basis of the constructed surfaces. The amount of lipofuscin in the DCN of the 18-year-old D98 is about two-fold that of the 13-year-old H01. However, the amount of lipofuscin in the subnuclei does not differ (Fig. S4). The lipofuscin mask was subtracted from the vGluT1 and vGluT2 channels and we obtained the masked vGluT1 and vGluT2 channels, respectively (Fig. S3c, e). Finally, the lipofuscin-removed vGluT1 and vGluT2 channels were surface-rendered for quantification (Fig. S3d, f).

